ROBUST ACTIVE AND REACTIVE POWER CONTROL SCHEMES FOR A DOUBLY FED INDUCTION GENERATOR BASED WIND ENERGY CONVERSION SYSTEM

PEDDA SURESH OGETI

DEPARTMENT OF ELECTRICAL ENGINEERING
NATIONAL INSTITUTE OF TECHNOLOGY ROURKELA

Robust Active and Reactive Power Control schemes for a Doubly Fed Induction Generator based Wind Energy Conversion System

Dissertation submitted to the
National Institute of Technology Rourkela
in partial fulfillment of the requirements of the degree of
Doctor of Philosophy

in

Electrical Engineering

by

Pedda Suresh Ogeti

Roll No:510EE809

Under the supervision of

Prof. Bidyadhar Subudhi

and

Prof. Ajit Kumar Panda

Department of Electrical Engineering

National Institute of Technology Rourkela

November 2016

Department of Electrical Engineering

National Institute of Technology Rourkela

November 11, 2016

Certificate of Examination

Roll Number: **510EE809**

Name: **Pedda Suresh Ogeti**

Title of Dissertation: **Robust Active and Reactive Power Control schemes for a Doubly Fed Induction Generator based Wind Energy Conversion System**

We the below signed, after checking the dissertation mentioned above and the official record book (s) of the student, hereby state our approval of the dissertation submitted in partial fulfillment of the requirements of the degree of Doctor of Philosophy in Electrical Engineering at National Institute of Technology Rourkela. We are satisfied with the volume, quality, correctness, and originality of the work.

Ajit Kumar Panda	Bidyadhar Subudhi
Co-Supervisor	Principal Supervisor
S.K.Patra	S.K.Jena
Member(DSC)	Member(DSC)

Examiner

A.K.Panda

Chairman(DSC)

Department of Electrical Engineering

National Institute of Technology Rourkela

Prof. Bidyadhar Subudhi

Prof. Ajit Kumar Panda

November 11,2016

Supervisor's Certificate

This is to certify that the work presented in this dissertation entitled "Robust Active and Reactive Power Control schemes for a Doubly Fed Induction Generator based Wind Energy Conversion System" by "Pedda Suresh Ogeti", Roll Number 510EE809, is a record of original research carried out by him under my supervision and guidance in partial fulfillment of the requirements of the degree of Doctor of Philosophy in Electrical Engineering. Neither this dissertation nor any part of it has been submitted for any degree or diploma to any institute or university in India or abroad.

Ajit Kumar Panda	Bidyadhar Subudhi
Co-Supervisor	Principal Supervisor

Declaration of Originality

I, Pedda Suresh Ogeti, Roll Number 510EE809 hereby declare that this dissertation entitled "Robust Active and Reactive Power Control schemes for a Doubly Fed Induction Generator based Wind Energy Conversion System" represents my original work carried out as a doctoral student of NIT Rourkela and, to the best of my knowledge, it contains no material previously published or written by another person, nor any material presented for the award of any other degree or diploma of NIT Rourkela or any other institution. Any contribution made to this research by others, with whom I have worked at NIT Rourkela or elsewhere, is explicitly acknowledged in the dissertation. Works of other authors cited in this dissertation have been duly acknowledged under the section "Bibliography". I have also submitted my original research records to the scrutiny committee for evaluation of my dissertation. I am fully aware that in case of any non-compliance detected in future, the Senate of NIT Rourkela may withdraw the degree awarded to me on the basis of the present dissertation.

November 11, 2016
NIT Rourkela

Pedda Suresh Ogeti

ACKNOWLEDGEMENT

First and foremost, I am truly indebted to my supervisor Prof. Bidyadhar Subudhi for his inspiration, excellent guidance and unwavering confidence through my study, without which this thesis would not be in its present form. I also thank him for his gracious encouragement throughout the work.

I express my gratitude for my co-supervisor Prof. Ajit Kumar Panda for encouraging and supporting with his valuable suggestions and guidance.

I also express my gratitude to director of NIST, Prof. Sangram Mudali for sponsoring and giving financial support throughout my PhD work.

I express my gratitude to the members of Doctorate Scrutiny Committee, Prof. S.K.Patra, Prof. S.K.Jena and Prof. A.K. Panda for their advise and care. I am also very much obliged to Prof.J.K.Satpathy, Head of the Department of Electrical Engineering, NIT Rourkela for providing all the possible facilities towards this work.

My wholehearted gratitude to my parents, Venkata Subbaiah and Lakshmi Devi, my sister Sumati and brother Venkata Suresh keeping faith on me and always shower me with their unconditional love.

I thank Raja and Murali for their enjoyable and helpful company.

Last but not the least, I like to record my special thank to my wife Vijaya Lakshmi for giving constant source of inspiration and support during this entire process.

November 11, 2016

NIT Rourkela

Pedda Suresh Ogeti

Roll No:510EE809

Abstract

In view of resolving rising environmental concern arising out of fossil fuel based power generation, more electricity has to be generated from renewable energy sources. Out of the several renewable energy options available today, wind energy is considered to be the most promising one due to its high energy conversion efficiency compared to one of its competitors, i.e. the solar photovoltaic system. Now-a-days, large wind farms are generating thousands of mega watts of power feeding to the grid.

In literature, number of controllers such as conventional proportional integral (PI) control, linear parameter varying (LPV) control, gain scheduling control, robust control, model predictive control have been proposed for both torque and pitch control. In these controllers, some of the important issues such as robustness for nonlinear dynamics of wind turbine and stability are not considered simultaneously. Hence, it is necessary to design appropriate controllers for extracting maximum power from the wind turbine whilst the robustness and stability of the Wind Energy Conversion System (WECS) are ensured. Hence, in this thesis, firstly the focus is made to design control system for the wind turbine coupled with the DFIG (torque and pitch control) using one of the very promising robust control paradigm called sliding mode controller for achieving robustness, reducing chattering phenomenon and stability of the WECS.

Since the number of terms in control inputs (i.e. torque and pitch angle) and outputs (i.e. DFIG output power and speed) are more in wind control dynamics, selection of significant terms is important for reducing the complexity of controlling. Therefore, a Nonlinear Autoregressive Moving Average with exogenous input (NARMAX) model of the WECS has been

developed. The parameters of this NARMAX model are estimated by suitably designing an on-line adaptive Recursive Least squares (RLS) algorithm. Subsequently for controlling speed and achieving efficient power regulation of the WECS a nonlinear model predictive controller (NAMPC) has been developed in which the control variables (torque and pitch) are optimised by formulating a cost function.

Subsequently for the WECS, the power converters connecting the DFIG to the grid have been designed. For controlling stator active and reactive power of DFIG connected to the grid, a state feedback controller for the DFIG has been developed using a linear quadratic optimal theory with preview concept. This Linear Quadratic Regulator Optimal Preview Control (LQROPC) scheme is employed with a stator voltage oriented control (SVOC) technique. This Optimal preview control is used to solve the tracking and rejection problems with an assumption that the signals to be tracked or rejected are available a priori by a certain amount of time.

Even though the OPC provides very good tracking and disturbance suppression performance, but it is sensitive to the DFIG circuit parameters which makes the WECS system unstable. Hence, to address the parameter uncertainty of the DFIG, a sliding mode controller has been proposed and the robustness of the WECS have been verified by using the Lyapunov criterion.

Then, a 2 kW DFIG based WECS experimental setup has been developed in the laboratory to study the effectiveness of the controllers developed.

Keywords:WECS, DFIG, NARMAX, LQROPC, PWM, RSC,GSC.

List of Acronyms

List of Acronyms

DFIG	:	Doubly Fed Induction Generator
WECS	:	Wind Energy Conversion System
FOC	:	Field Oriented Control
DTC	:	Direct Torque Control
DPC	:	Direct Power Control
SVOC	:	Stator Voltage Oriented Control
RSC	:	Rotor Side Control
GSC	:	Grid Side Control
SMC	:	Sliding Mode Control
MPC	:	Model Predictive Control
VSC	:	Voltage Source Converter
PI	:	Proportional Integral
PLL	:	Phase Locked Loop
FAST	:	Fatigue Aerodynamic Structure Turbulence).
LPV	:	Linear Parameter Varying
LVRT	:	Low Voltage Ride Through
NARMAX	:	Non-linear Autoregressive Moving Average with Exogenous Input
OPC	:	Optimal Preview Control
PWM	:	Pulse Width Modulation
JTAG	:	Joint Test action Group
FPGA	:	Field Programmable Gate Array
MPPT	:	Maximum Power Point Tracking

NAMPC	:	Non-linear Adaptive Model Predictive controller
RLS	:	Recursive Least Square
ERR	:	Error Reduction Ratio
MIMO	:	Multi Input Multi Output
ZOH	:	Zero Order Hold
PID	:	Proportional-Integral-Derivative
LMI	:	Linear matrix inequality
LQR	:	Linear-Quadratic Regulator

List of Figures

1.1 GWEC worldwide wind energy capacity by 2014[1] 4
1.2 Scenerio for future wind energy proposed by IEA and IPCC for India 4
1.3 Scenerio for future wind energy proposed by IEA and IPCC for world 5
1.4 (a) Horizontal-axis wind turbine and (b) Vertical-axis wind turbine 6
1.5 MPPT power control with wind turbine power profile 9
1.6 MPPT control with wind turbine optimal tip speed ratio control 10
1.7 MPPT control with wind turbine optimal torque control 10
1.8 Fixed speed WECS without power converters interface 11
1.9 Variable speed WECS with variable rotor resistance 12
1.10 Variable speed WECS with reduced power capacity converters 12
1.11 Variable speed WECS with full capacity converters 13
1.12 Schematic diagram of Flux Oriented Control 14
1.13 Schematic diagram of Direct Power Control 16
1.14 Schematic diagram of Rotor Current Controller 17
1.15 Schematic diagram of Model Predictive Controller 18

2.1 Schematic diagram of WECS 24
2.2 Grid side converter control system 25
2.3 Rotor side converter control system 26
2.4 Stator flux estimator 26
2.5 Torque control on rotor side converter 27
2.6 Pitch control of WECS 27

2.7 Gain scheduling for pitch control 28
2.8 Design Flow in FPGA implementation 29
2.9 JTAG Co-Simulation 30
2.10 Structure of Pitch control system of a WECS 34
2.11 Wind turbine model 35
2.12 Pitch angle characteristics of wind turbine 35
2.13 Pitch angle control system using SMC 37
2.14 Variation of wind speed(m/sec) Versus time(sec) 41
2.15 Electromagnetic torque(N-m) Versus time(sec) 41
2.16 Generated power of DFIG(pu) versus time 42
2.17 Three phase voltage at stator terminals u_{abc} 42
2.18 Three phase current at stator terminals i_{abc} 43
2.19 Rotor speed of DFIG(rad/sec) versus time 43
2.20 Frequency at the stator terminals versus time 44
2.21 Pitch angle(deg) versus time 44
2.22 Wind profile versus time 45
2.23 Pitch angle β versus time 46
2.24 Generated Power P(kW) versus time 46
2.25 Reactive Power Q versus time 47
2.26 generator rotor Speed ω_r versus time 47

3.1 Ideal power curve P_m Versus v_w) for DFIG WECS 51
3.2 Schematic diagram of a WECS 53
3.3 Structure of the Multivariable Self Tuning Regulator for DFIG WECS 57
3.4 Parameter extraction using on-line Recursive structure identification 62
3.5 NAMPC structure with RLS NARMAX identification technique 64
3.6 Wind speed profile in partial load region for Gaussian noise disturbance . . . 67
3.7 Response of Generator speed ω_G for different values of weight z_1 67
3.8 Response of Output Power P_G for different values of weight z_1 68
3.9 Response of control input Γ_G for different values of control weight z_1 68

3.10 Response of control input β for different values of control weight z_1 69
3.11 Performance comparison for ω_G 70
3.12 Performance comparison for P_G 70
3.13 Performance comparison for Γ_G 71
3.14 Performance comparison for β 71

4.1 Schematic diagram of DFIG based WECS 76
4.2 Space Vector representation of DFIG 77
4.3 Equivalent circuit of DFIG 77
4.4 Structure of Proposed optimal preview control of DFIG 82
4.5 Structure of the Proposed Optimal Preview Controller 84
4.6 Controller design for VSC using current regulator 87
4.7 Implementation of LQR OPC in DFIG WECS using SIMULINK 88
4.8 Simulation of DFIG WECS using RT LAB 90
4.9 Design of Master Subsystem using RT LAB 91
4.10 Design of Slave Subsystem of LQR OPC 91
4.11 Design of Console Subsystem of DFIG WECS using RT LAB 92
4.12 Interfacing host computer and RT lab 92
4.13 Performance plots for LQR OPC controller 93
4.14 Performance plots for LQR OPC controller 93
4.15 Performance plots for LQR OPC controller 94
4.16 Performance plots for LQR OPC controller 95
4.17 Comparison of LQROPC,SMC-DTC and SMC-FOC controllers 96
4.18 Experimental setup for DFIG WECS using RT-LAB simulator 97
4.19 V model for RT lab Simulator 98
4.20 Block diagram for RT Lab set up of DFIG WECS 98
4.21 Sub synchronous numeric data for N=1300rpm and P=300w of DFIG WECS 103
4.22 Sub synchronous waveform analysis for N=1300rpm and P=300w 104
4.23 Sub synchronous numeric data for N=1300rpm and P=450w of DFIG WECS 106
4.24 Sub synchronous waveform analysis for N=1300rpm and P=450w 107

4.25 Super synchronous numeric data for N=1700rpm and P=300w of DFIG WECS109
4.26 Super synchronous waveform analysis for N=1700rpm and P=300w 110
4.27 Super synchronous numeric data for N=1700rpm and P=450w of DFIG WECS112
4.28 Super synchronous waveform analysis for N=1700rpm and P=450w 113

5.1 Sliding mode controller design for DFIG WECS 121
5.2 Stator voltage versus time 124
5.3 Stator current versus time 124
5.4 Active Power versus time 125
5.5 Reactive Power versus time 125
5.6 ω_r versus time 126
5.7 DC voltage versus time 126
5.8 Numeric data for N=1700 rpm and P=300 w of DFIG WECS 128
5.9 Waveform data for N=1700 rpm and P=300 w of DFIG WECS 128
5.10 FOC control of Stator and rotor parameters for Subsynchronous mode 130
5.11 DPC control of Stator and rotor parameters for Subsynchronous mode 130
5.12 LQROPC control of Stator and rotor parameters for Subsynchronous mode . 131
5.13 FOC control of Stator and rotor parameters for Super synchronous mode . . 132
5.14 DPC control of Stator and rotor parameters for Super synchronous mode . . 132
5.15 LQROPC control of Stator and rotor parameters for Super synchronous mode 133

List of Tables

3.1 Simulation Parameters for DFIG WECS 66
3.2 Comparison of computational burden 72

4.1 DC Machine Parameters 88
4.2 DFIG Parameters 89
4.3 Descriptions of the parameters for result analysis 102

5.1 Descriptions of the parameters 127
5.2 Descriptions of the parameters for rotor and stator side 129

Contents

Abstract **i**

List of Acronyms **iv**

1 INTRODUCTION **3**

1.1 Background of WECS 3

1.2 Classification of Wind turbines 6

1.2.1 Stand-Alone and Grid connected WECS 6

1.2.2 On-land and Offshore wind farms 6

1.2.3 Horizontal Axis and Vertical Axis Wind Turbines 6

1.2.4 Fixed and variable speed wind turbines 7

1.3 Control methods for wind turbine for maximizing power conversion efficiency 7

1.3.1 Stall Control 8

1.3.2 Pitch Control 9

1.4 Maximum Power Point Tracking (MPPT) for WECS 9

1.5 Configurations of WECS 10

1.5.1 Fixed speed WECS without power converters 11

1.5.2 Variable speed WECS 11

1.6 Review of control techniques for WECS 13

1.6.1 MPPT Algorithms 13

1.6.2 Flux oriented control (FOC) 13

1.6.3 Stator Voltage Oriented Control (SVOC) 14

1.6.4 Direct Torque Control (DTC) . . . 15
1.6.5 Direct Power Control (DPC) . . . 15
1.6.6 Current Mode Control (CMC) . . . 16
1.6.7 Model Predictive Control (MPC) . . . 17
1.6.8 Linear Parameter Varying (LPV) H_∞ control . . . 18
1.7 Motivation . . . 19
1.8 Objectives of the thesis . . . 19
1.9 Outline of the Thesis . . . 20

2 Sliding Mode Torque and Pitch Controller Design for a WECS 21
2.1 Introduction . . . 21
2.1.1 Objectives . . . 23
2.2 Modelling of WECS . . . 23
2.2.1 Wind Turbine Modeling . . . 23
2.2.2 Drive Train Subsystem . . . 24
2.2.3 V-I relationships in d-q reference frame using generator convention . . . 25
2.2.4 FPGA Design . . . 29
2.2.5 JTAG(Joint Test Action Group) Co-Simulation . . . 29
2.3 SMC design for pitch and torque control . . . 30
2.3.1 Torque controller design . . . 31
2.3.2 Derivation of sliding mode control law for torque control . . . 31
2.3.3 Pitch controller design . . . 34
2.3.4 Derivation of SMC law for pitch angle control . . . 36
2.4 Results and Discussion . . . 40
2.5 Chapter Summary . . . 48

3 NARMAX model based Torque and Pitch Control schemes for WECS 49
3.1 Introduction . . . 49
3.2 Problem statement . . . 51
3.2.1 Chapter Objectives . . . 52
3.3 Physical model of DFIG based WECS . . . 52

3.4 State space model of DFIG WECS 53
3.5 NARMAX model Structure Representation of DFIG WECS 56
3.5.1 Structure representation 56
3.5.2 Extended Polynomial NARMAX Model of DFIG WECS 57
3.5.3 Orthogonal Least squares QR decomposition of the regression matrix 59
3.5.4 Normalizing the columns of Q 60
3.5.5 Structure determination (sub set selection) 61
3.5.6 Parameter estimation 62
3.6 Optimization of torque and pitch angle using NAMPC technique 63
3.7 Results and Discussion 65
3.8 Chapter Summary 72

4 Active and Reactive Power Control of DFIG WECS with OPC SVOC 73
4.1 Introduction 73
4.1.1 Chapter Objectives 75
4.2 Proposed structure of WECS 75
4.2.1 Stator active and reactive power control (slow control loop) 78
4.2.2 Inner rotor current control loop (Fast control loop) 79
4.3 State space model of DFIG 80
4.4 Augmented Error System for DFIG 82
4.5 Optimal Preview Control Law 84
4.6 Design of controller for VSC with optimised rotor current dynamics 87
4.7 Results and Discussion 88
4.8 Experimental set up 95
4.9 Sub synchronous mode 99
4.9.1 Sub synchronous mode for N=1300 rpm and P=300 w of DFIG WECS 100
4.9.2 Sub synchronous mode for N=1300 rpm and P=450 w of DFIG WECS 105
4.10 Super synchronous mode 108
4.10.1 Super synchronous mode for N=1700 rpm and P=300 w of DFIG WECS108
4.10.2 Super synchronous mode for N=1700 rpm and P=450 w of DFIG WECS111

4.11 Chapter Summary 114

5 Active and Reactive Power Control of DFIG WECS with SMC 115

5.1 Introduction 115

5.1.1 Chapter Objectives 117

5.2 Modelling of stator active and reactive power of DFIG 117

5.3 Design of SMC for active and reactive power control 119

5.4 Robustness verification using Lyapunov theory 122

5.5 Results and Discussion 123

5.5.1 Experiment Results 127

5.6 Comparative analysis of SMCFOC, SMCDPC and LQROPC 129

5.6.1 Sub synchronous mode 129

5.6.2 Super synchronous mode 131

5.7 Chapter Summary 133

6 Conclusions and Future Directions 135

6.1 Conclusions of the thesis 135

6.2 Contributions of the thesis 136

6.3 Suggestions for Future Work 137

6.4 Thesis Dissemination 138

References 139

Chapter 1

INTRODUCTION

1.1 Background of WECS

Alternate to fossil fuels and non renewable sources, wind power emerged as a powerful renewable energy resource for generation of electric power. Wind power plays a vital role for electrical power transmission network compared to other renewable sources. Wind turbines extract wind power from air flow to produce mechanical power. Induction Generators connected to wind turbines convert mechanical power into electrical power. Wind power is clean, renewable, produces no green house emissions, available plentiful, widely distributed and uses little land with almost zero environmental problems. Wind farms are broadly classified as on-shore and off-shore wind turbines. Small onshore wind farms provide electricity to isolated off-grid locations and some energy into the grid. Wind power significantly varies and inconsistent from year to year, therefore wind power is used in conjunction with the other electric power sources to meet the requirements of grid and for reliable supply of electric power. The first wind turbine has been built by James Blyth of Andersons College, Glasgow (now Strathclyde University) in 1887. Later Danish scientist Poul la Cour in the 1890s, has worked to built 2500 turbines in Denmark to generate 30 MW peak power capacity. By 1931, 100kW horizontal-axis wind generators on a 30-meter-high tower was put into service at Yalta, in Russia with a load factor of 32%. In 1941, the worlds first grid-connected 1.25 MW turbine was on Grandpas Knob in Castleton. In mid-1950s, Denmark built the first

wind turbine. In 1956, Danish Wind Industry Association (DWIA), has built the 200kW Gedser wind turbine in southern Denmark with 3 blade concept. In 1973 the first oil crisis occurred in UK, Germany, Denmark, Sweden, U.S., and some other countries, scrambled to design larger wind turbines.

In India wind power development began in 1990s, and has increased significantly since last

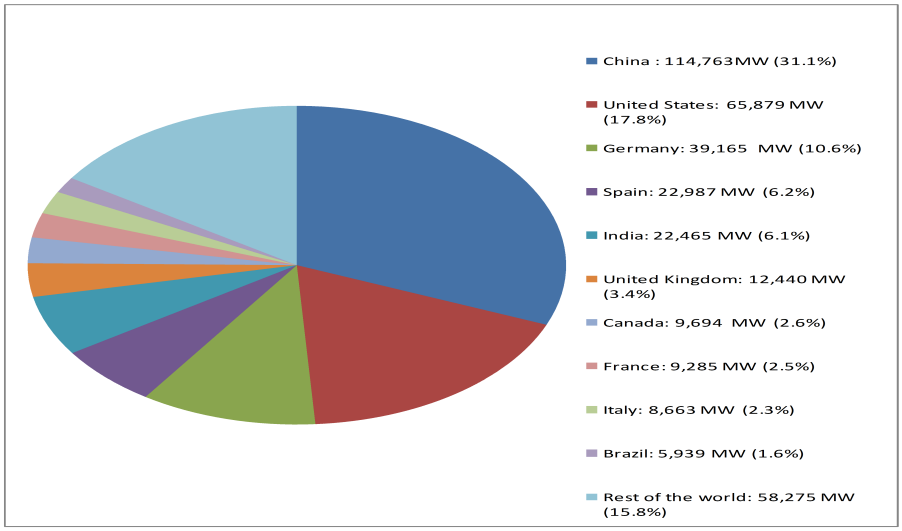

Figure 1.1: GWEC worldwide wind energy capacity by 2014[1]

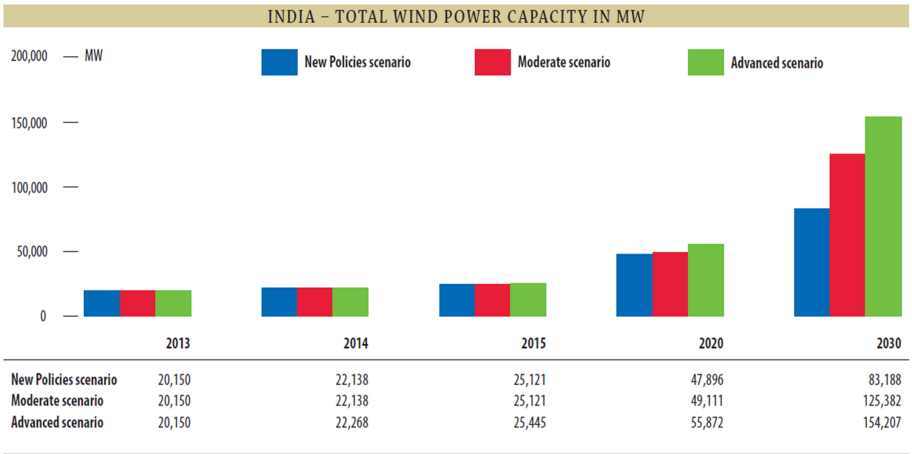

Figure 1.2: scenerios for future wind energy proposed by International Energy Agency (IEA) and Intergovernmental Panel on Climate Change (IPCC)for India[1]

few years. India occupies the fifth position in wind power installations in the world. India's growth ratein wind power was highest in 2009-2010 compared to top four countries. By the

end of 30 June 2015, India has wind power installed capacity of 23,763 MW. By the year 2022, the MNRE sets the target of 60,000 MW wind power generation capacity. By 2012, installed capacity of wind power reached to 283 GW worldwide[1].

As of 2014, about 4% of world wide electricity has been generated by wind power. By December 2014, wind power capacity has been expanded to 3,69,553 MW.

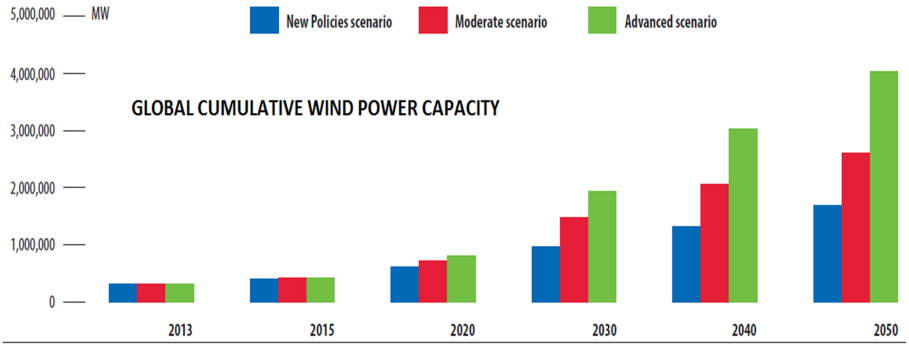

	2013	2015	2020	2030	2040	2050
New Policies scenario						
MW	318,128	396,311	610,979	964,465	1,324,814	1,684,074
TWh/a	620	972	1,499	2,535	3,482	4,426
Moderate scenario						
MW	318,128	413,039	712,081	1,479,767	2,089,261	2,672,231
TWh/a	620	1,013	1,747	3,889	5,491	7,023
Advanced scenario						
MW	318,128	420,363	800,615	1,933,989	3,024,473	4,042,475
TWh/a	620	1,031	1,964	5,083	7,948	10,624

Figure 1.3: scenerios for future wind energy proposed by International Energy Agency (IEA) and Intergovernmental Panel on Climate Change (IPCC)for world[1]

Fig.1.1 shows the GWEC worldwide wind energy capacity by 2014 where China is in the top position for generating wind power. Fig.1.2 show the scenerio of the future wind energy generation proposed by the International Energy Agency (IEA) and Intergovernmental Panel on Climate Change (IPCC) for India upto 2030. From Fig.1.2, it is observered that wind power generation will drastically increase to 1.5 lakh MW by 2030. Fig.1.3 shows the scenerio of the future wind energy generation proposed by International Energy Agency (IEA) and Intergovernmental Panel on Climate Change (IPCC)for world. From Fig.1.3, it is seen that 40 lakh MW wind power generation is being done all over the world.

1.2 Classification of Wind turbines

1.2.1 Stand-Alone and Grid connected WECS

Small capacity wind turbines are operated as stand-Alone units in farms, islands and villages where grid is not accessible or costly. Now-a-days majority of wind farms are connected to the grid, so wind turbines with large capacity are directly connected to the grid. Since the wind turbine generators are capable of withstanding low voltage(typically 690V), transformers are utilised for stepping up the voltage to 35kV, further this voltage is stepped up with the substation transformer.

1.2.2 On-land and Offshore wind farms

On-land wind farms are installed where wind speed is adequate. On-land wind farms have advantages such as access is convenient, erosion is less, capital cost and maintenance cost is less, and energy production is good. Offshore wind farms are installed where wind speed is higher and steadier and there is no limit for land/area. But in these firms capital cost and maintenance are very high.

1.2.3 Horizontal Axis and Vertical Axis Wind Turbines

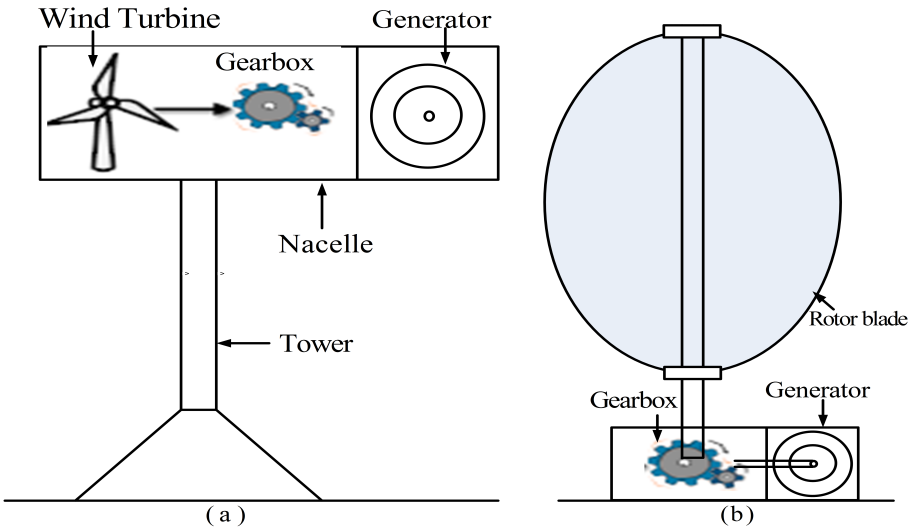

Figure 1.4: (a) Horizontal-axis wind turbine and (b) Vertical-axis wind turbine

Wind turbines are classified as horizontal or vertical axis turbines as shown in Fig. 1.4. If the orientation of spin axis of the blades are parallel to the ground, then it is a horizontal axis wind turbine. If the orientation of spin axis is perpendicular to the ground, then it is called vertical axis wind turbine.

1.2.4 Fixed and variable speed wind turbines

Fixed speed wind turbines operate only for a constant speed. For all other speeds, the system efficiency degrades. It depends on gear ratio, number of poles of generator and grid frequency.

Variable speed wind turbines are operated for a wide range of wind speeds. According to wind speed, the turbine adjusts its rotational speed. For obtaining maximum power conversion efficiency, the tip speed ratio is kept at its optimum value for different values of wind speed.

1.3 Control methods for wind turbine for maximizing power conversion efficiency

Nominal speed of wind turbine is 3 to 15 m/sec. In order to capture maximum power, wind turbine blades are operated in this range. For below rated speed i.e. less than 3 m/sec, the turbine will not rotate due to large inertia. Hence torque control is employed for below rated speed. For above rated speeds, in the range from 15 to 25m/sec, aerodynamic power control of turbine is desired.

Aerodynamic power captured by the blade is given by

$$P_w = 0.5\rho\Lambda {v_w}^3 \tag{1.1}$$

Aerodynamic power converted to mechanical power is given by

$$P_m = 0.5\rho\Lambda C_P(\lambda,\beta) {v_w}^3 \tag{1.2}$$

Tip speed ratio λ and pitch angle β are given by

$$\lambda = \frac{\omega_m r_t}{v_w} \; ; \; \beta = \frac{\omega_m^3}{P_m} \tag{1.3}$$

where β denotes turbine blade pitch angle, C_P is power coefficient, ω_m is of the turbine rotational speed, ρ is air density in g/m^3 , Λ is sweep area in m^2 , v_w is the wind velocity, r_t is the radius of turbine shaft.

From eq(1.1), it is observed that the power captured by the wind turbine can be increased in three different ways. i.e. by varying wind speed v_w, power coefficient C_P and swept area Λ. As wind speed cannot be increased, wind turbines need to be installed in regions of higher average wind speeds. In the second method, the area of turbine is to be increased. As the area is proportional to twice the blade length $\left(\Lambda = \pi l^2\right)$, the power captured will be maximum. In the third method, the power coefficient C_P is varied. For extracting maximum power, aerodynamic forces on the turbine blades are controlled by using stall and pitch control methods.

1.3.1 Stall Control

When the wind speed exceeds the rated value, heavy wind causes the turbulence on the blade surface not facing the wind direction, which results in reducing the lifting force of the blade and finally slowing down the rotational speed of the turbine which is called stall. There are two types of stall, such as passive and active stall.

When the wind speed is less than the rated value, angle of attack is kept at the optimal value which captures the maximum power. When the wind speed exceeds 15m/sec, passive stall is employed. Air turbulence acts on the surface of the blade in the opposite direction of wind, which reduces the lift force on the turbine blades. This causes the reduced power capture. Passive stall is employed in small turbines. No sensors or actuators are used and therefore passive stall is cost effective and robust.

In active stall, stall phenomenon is implemented by using high wind speeds and increasing the angle of attack of the blades. For above rated speed, in active stall, the adjustable blades are made to turn into the wind direction, which results in reduced power capture. The power

capture can be increased and maintained at rated value by adjusting the angle of attack.

1.3.2 Pitch Control

Pitch control is similar to active stall, but the wind makes the blades to turn out of its direction, causing turbulence which reduces the lift force causing the turbine to come to halt position. Pitch controller reduces the angle of attack gradually turning the blades out of wind speed.

1.4 Maximum Power Point Tracking (MPPT) for WECS

In [2], for variable speed wind turbines, three MPPT techniques have been proposed, based on generation of reference mechanical power P_m^*, reference generator speed ω_m^* and desired reference torque T_m^*.

Fig. 1.5 depicts maximum power versus wind speed curve. The reference power P_m^* is

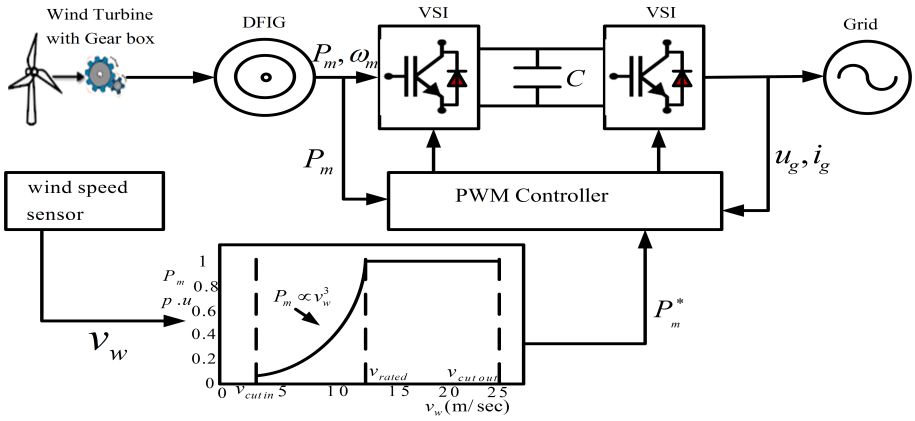

Figure 1.5: MPPT power control with wind turbine power profile

compared with actual measured power P_m for generating the control pulses for the power converters. Maximum power point tracking (MPPT) is achieved by controlling the power converters and making generator reference mechanical power equal to the measured mechanical power at the steady state. u_g and i_g are the grid voltage and grid current respectively.

In Fig. 1.6, the measured wind speed and maintaining optimal tip speed ratio generates the reference generator speed ω_m^* and this is compared with the measured generator speed ω_m for generating the control pulses for power converters. MPPT is achieved when generator

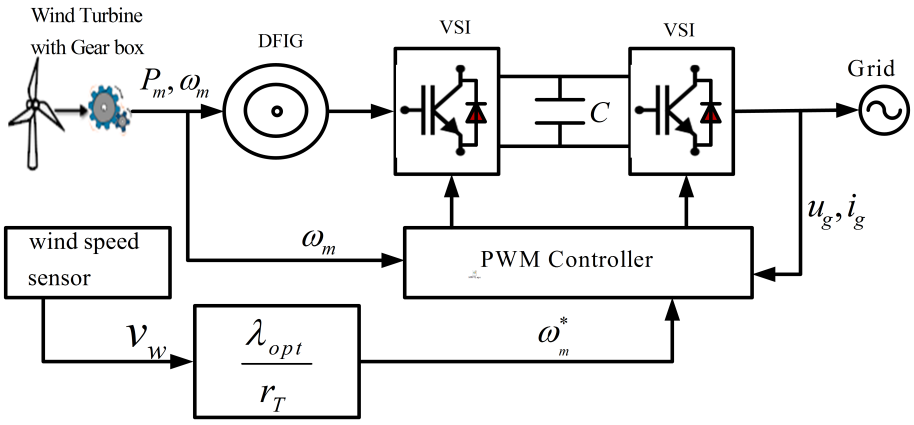

Figure 1.6: MPPT control with wind turbine optimal tip speed ratio control

reference is equal to measured generator speed at the steady state.

In Fig. 1.7, based on $T_m \propto \omega_m^2$, an optimal torque T_m^* is generated from measured generator

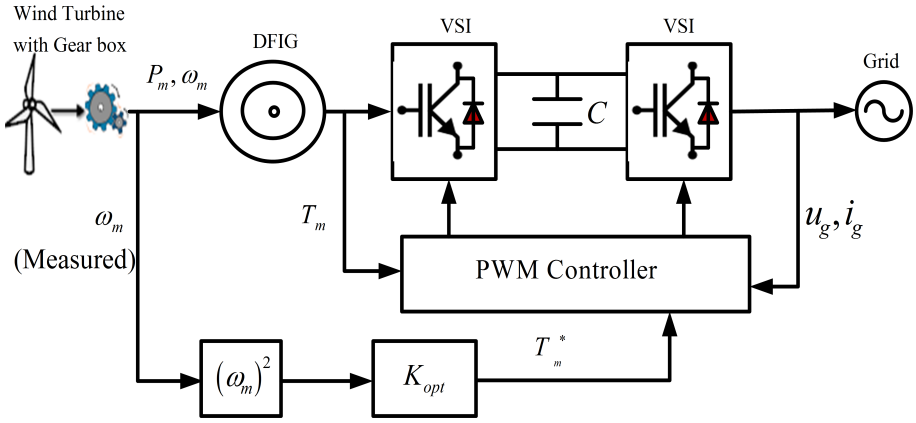

Figure 1.7: MPPT control with wind turbine optimal torque control

speed ω_m and comparing with actual generator torque and finally MPPT is achieved when $T_m^* = T_m$ at steady state.

1.5 Configurations of WECS

Generators and power converters are the main electrical components of a WECS. According to these two different types of converters, three different configurations are proposed for both fixed and variable speed WECS.

1.5.1 Fixed speed WECS without power converters

In Fig. 1.8, the structure of a fixed speed WECS without power electronic interface converter is shown in which the gear box is used to match the speed of wind turbine and generator for delivering the rated power at rated speed. During the system start-up, heavy in-rush current is limited using a soft starter and later it is bypassed by a switch. For compensating the reactive power drawn by the induction generator, a three phase capacitor bank is installed.

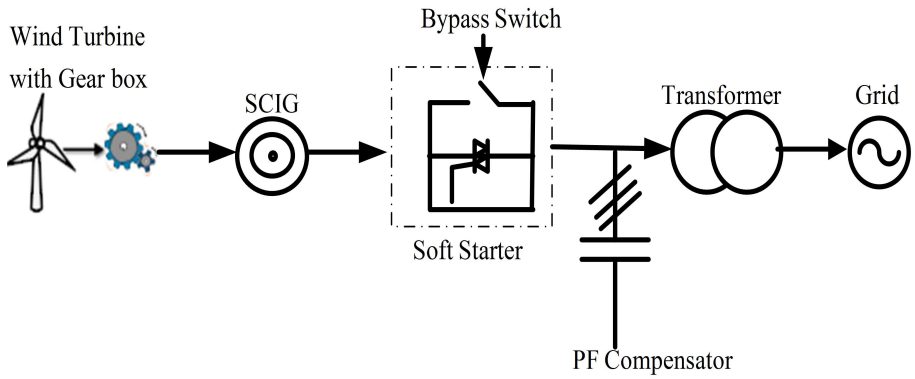

Figure 1.8: Fixed speed WECS without power converters interface

1.5.2 Variable speed WECS

Variable speed WECS systems are classified into two types based on the power rating of the power electronics converter, such as reduced capacity converters and full capacity converters. Due to the use of these power converters, decoupling between the generator and grid can be made automatically.

Fig. 1.9 and Fig. 1.10 shows the reduced capacity converters of WECS where as Fig. 1.11 depicts the structure of the full capacity converter WECS. Variable speed reduced capacity converters are designed only with wound rotor induction generators, since rotor currents can be controlled on rotor side for variable speed operation without the need for total power in power system. Reduced capacity converters are again classified into two types such as wound rotor induction generator with variable rotor resistance shown in Fig. 1.9 and doubly fed induction generator(DFIG) with rotor converter shown in Fig. 1.10.

Wound rotor induction generators is shown in Fig. 1.9, with a variable resistance in the rotor

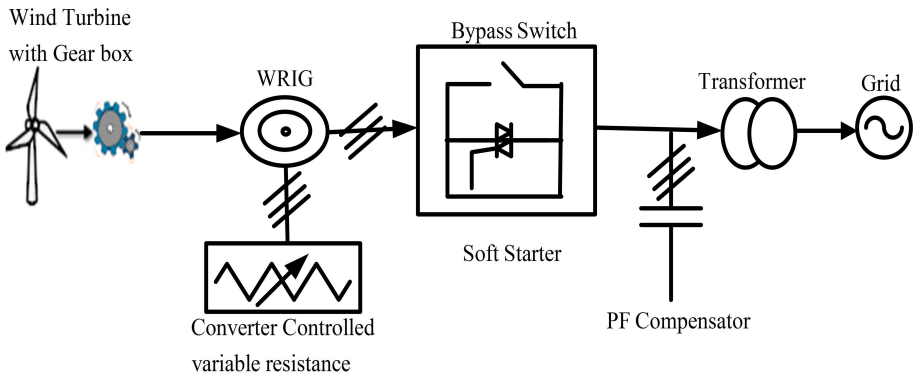

Figure 1.9: Variable speed WECS with variable rotor resistance

circuit. Variable speed operation of the turbine is achieved by varying the rotor resistance which affects the torque/speed characteristics of generator. The rotor resistance is varied with the help of power converter. The speed of WRIG can be increased only 10 % above the rated synchronous speed of the generator. In variable speed configuration more power is captured from the wind, but due to rotor resistance, energy losses are more and this configuration necessitates a soft starter and reactive power compensation equipment.

In Fig. 1.10, DFIG WECS is shown, where variable resistance in the rotor circuit is replaced

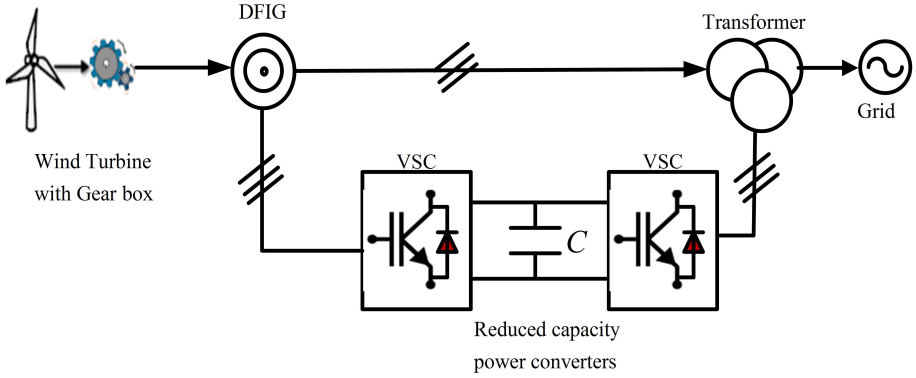

Figure 1.10: Variable speed WECS with reduced power capacity converters

by power converters and there are no power compensation and soft starter. The power in the rotor circuit processes only slip power, that is only 30 percent of the rated power of the generator. Due to reduction in the power capacity, the cost of converter equipment is less compared to the full capacity converters.

Full capacity converters are shown in Fig. 1.11, where generator is directly connected to

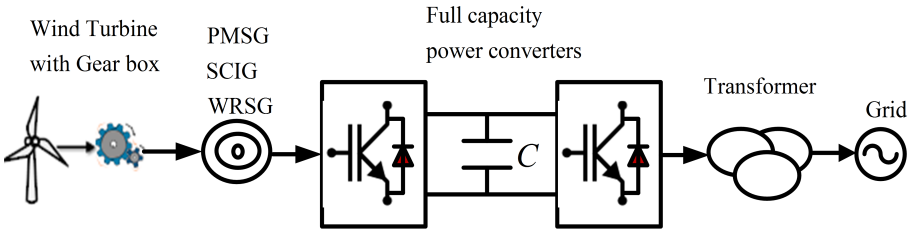

Figure 1.11: Variable speed WECS with full capacity converters

the grid via power electronics converters. In this configuration, a wind generator i.e SCIG, WRIG and PMSG generators can be used. Converters power rating is equal to the generator power rating. Due to presence of power converters, generator can be decoupled from the grid and it can operate in full speed range.

1.6 Review of control techniques for WECS

A number of controllers are proposed in the literature for DFIG WECS to extract maximum power from WECS.

1.6.1 MPPT Algorithms

Conventional hill climb searching (HCS) has been proposed in [3] for maximum power point tracking (MPPT) for WECS. But these MPPT algorithms are not effective for tracking the maximum power reference.

1.6.2 Flux oriented control (FOC)

The field orientated control can be classified as stator flux, air gap flux and rotor flux orientations [4, 5, 6, 7, 8, 9, 10, 11, 12, 13, 14, 15, 16, 17, 18, 19]. FOC is further classified as direct field oriented control (DFOC) and indirect field oriented control (IFOC). FOC is implemented based on measurement of stator voltages and stator currents but IFOC is based on measured stator speed and calculated slip frequency. Orienting the stator flux rather than rotor flux offers the additional advantages of more robust estimation of the flux and more

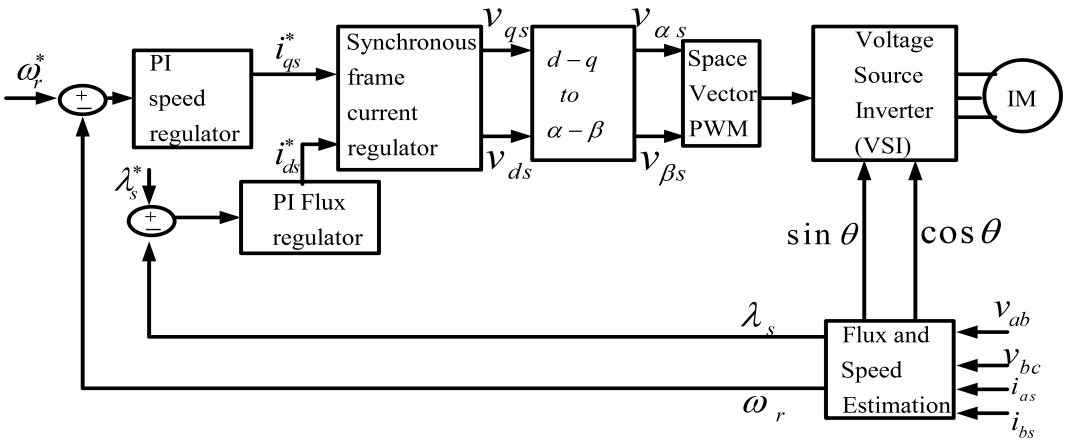

Figure 1.12: Schematic diagram of Flux Oriented Control

direct control of the stator voltage in the field weakening region. Stator flux is estimated from terminal voltages and phase currents by using $\alpha-\beta$ or $d-q$ reference frame as shown in Fig. 1.12. The essence of field oriented control is that the decoupled control of λ_r (flux) and electromagnetic torque (τ_e) of the generator are used to achieve high dynamic performance. With a properly designed flux regulator and decoupling compensator, the performance of direct stator flux orientation control is comparable with the well-tuned rotor flux oriented system. In IFOC, a shaft sensor is needed for measuring the rotor speed (or shaft encoder). One way to avoid shaft sensor is to estimate flux, which can be either rotor flux or stator flux or air gap flux directly direct field orientation (DFO) from the rotor voltage and current measurements.

1.6.3 Stator Voltage Oriented Control (SVOC)

SVOC is preferred over FOC since decoupling can be accomplished among torque and flux in the vector control method and as compared to the flux control. In stator field oriented control(FOC), there is a limit on the reactive power production, when the machine goes to the unstable position. Hence SVOC is designed, where inner rotor control loop tracks its reference values perfectly by tuning the PI controllers where stability is ensured. Current dynamics of DFIG are faster than mechanical dynamics of wind turbine.

In SVOC scheme [20, 21, 22, 8, 23], the d-axis is aligned to the reference frame of the

stator voltage, $v_s = \sqrt{v^2{}_{ds} + v^2{}_{qs}} = v_{ds}$. To realize SVOC, grid voltage angle is measured and its angle is detected for the voltage orientation, $\theta_g = tan^{-1}\left(\frac{v_\beta}{v_\alpha}\right)$.
However, the performance of the PI controller is highly dependent on tuning of their gain parameters and accurate tracking of angular information of stator flux/voltage. Moreover, the vector or field oriented control schemes necessitate accurate values of machine parameters and rotor speed. This vector control requires complex transformations among rotor, stator and synchronous reference frames. Hence this controller design is complex.

1.6.4 Direct Torque Control (DTC)

To overcome the tuning difficulties of the controllers in vector control (VC) scheme and to reduce the control complexity, a direct torque control (DTC)[24, 25, 26, 27, 28, 29, 30, 8, 31, 32, 33] has been proposed . DTC is used to control the electromagnetic torque of the generator by adjusting its torque angle θ_T and maintaining the stator flux constant at rated value. In DTC, machine torque is directly controlled by selecting appropriate stator flux and torque information which are given to the hysteresis comparators. These are evaluated in a switching logic unit for generating the switching states of the rectifier connected to rotor of DFIG.
One of the problems associated with the DTC scheme is that its performance deteriorates during starting and very-low-speed operations. This is mainly due to repeated selection of zero voltage vectors at low speed resulting in flux level reduction owing to the stator resistance drop.

1.6.5 Direct Power Control (DPC)

When using DTC at low rotational speed, zero voltage vectors are most frequently applied to the machine terminals causing a flux reduction because of the stator resistance. In DTC, performance deteorites during starting and low speed operations. To avoid this disadvantage, DPC has been proposed. A DPC strategy [34, 35, 8, 36, 37, 38, 39, 40, 41, 42, 43, 44, 45] minimises the use of zero voltage vectors. Based on the principles of DTC, DPC has been proposed for a three phase rectifier. This method is based on the stator flux and only machine parameter required is stator resistance. Rotor speed ω_r is measured and is used to transform

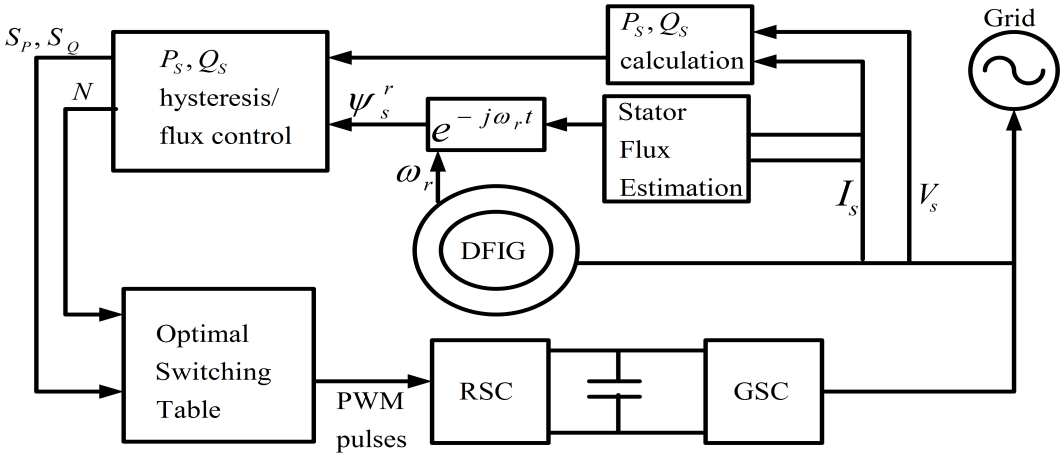

Figure 1.13: Schematic diagram of Direct Power Control

the stator flux for appropriate PWM pulse generation as shown in Fig. 1.13. However, it has some drawbacks such as high amount of ripple in active power, reactive power and currents. As shown in Fig. 1.13, the three-phase ac voltages and currents of the stator V_s and I_s are measured and transformed into the stationary $\alpha-\beta$ reference frame. The active and reactive power P_s and Q_s are calculated and the stator flux is then estimated. N is the number of switching vector in optimal switching table. The rotor speed/position is measured and is used to transform the stator flux from the $\alpha-\beta$ frame to the rotor $\alpha_r-\beta_r$ frame. The calculated active and reactive power are compared to their reference values and S_P and S_Q are generated. The two active and reactive power states are then fed to the optimal switching table together with the calculated stator flux position to obtain the appropriate switching states. Finally, the optimal switching states are fed to the converter to provide the control required to reduce the power errors.

1.6.6 Current Mode Control (CMC)

To minimize variable switching frequencies and current distortions, a current mode control (CMC) has been proposed in [46, 47, 48, 49, 50, 51]. In CMC, control on rotor side converter is achieved by controlling the rotor currents on rotor side of DFIG as shown in Fig. 1.14. CMC requires a capacitor in both rectifier and inverter sides to assist in commutation of their switching devices. Two parallel controllers, which are developed using the positive

and negative-synchronous reference frames. The positive-sequence controller regulates the rotor side converter as in the case of normal operating conditions, while the pulsations at twice the line frequency are significantly reduced with the negative-sequence controller. The unbalanced currents will create unequal heating of the stator and rotor windings as well as torque and power pulsations in the generator at twice the line frequency. Fig. 1.14 shows the

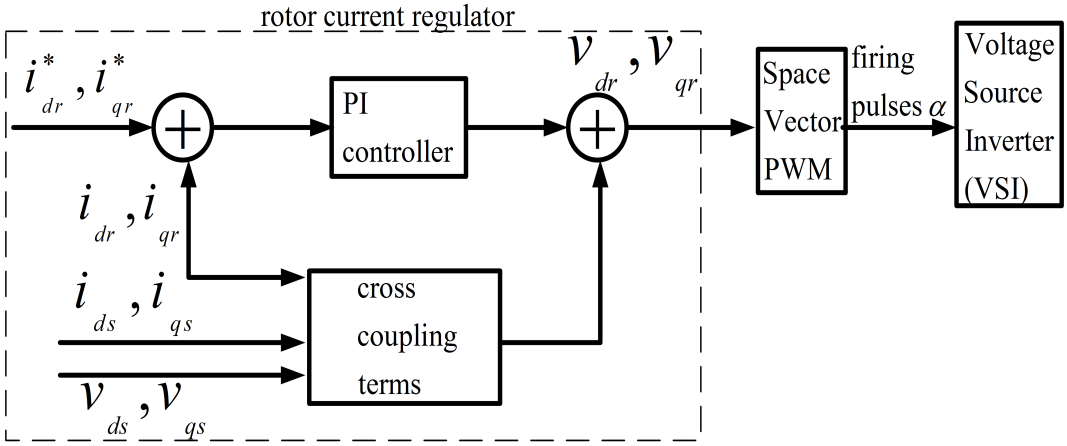

Figure 1.14: Schematic diagram of Rotor Current Controller

diagram of a current regulator intended for unbalanced grid faults. The regulator combines a proportional-integral (PI) controller with cross-coupling terms. The cross-coupling terms are used to decouple the dynamics of dq subsystems. i_{dr}, i_{qr} are the dq rotor currents, i^*_{dr}, i^*_{qr} are the rotor reference currents, i_{ds}, i_{qs} are the stator currents, v_{dr}, v_{qr} are the dq rotor voltages and v_{ds}, v_{qs} are the dq stator voltages. The rotor voltages obtained are used for generating PWM pulses for Voltage source inverter.

1.6.7 Model Predictive Control (MPC)

For limiting the rotor over current during a grid side fault, model predictive control (MPC) has been proposed in [52, 8, 53, 54, 55, 56, 57, 58, 59, 60, 61]. MPC performs an optimization procedure to calculate optimal control actions at each sampling interval. MPC is an advanced control strategy that can handle multiple constraints, i.e., it can manipulate and control system variables in predefined ranges. This feature is perfect for coping up with the abrupt change in the rotor currents. Further, the ability to incorporate optimal

control requirements through minimisation of cost function makes it even more attractive for DFIG control. The control law is derived by optimization of an objective function that

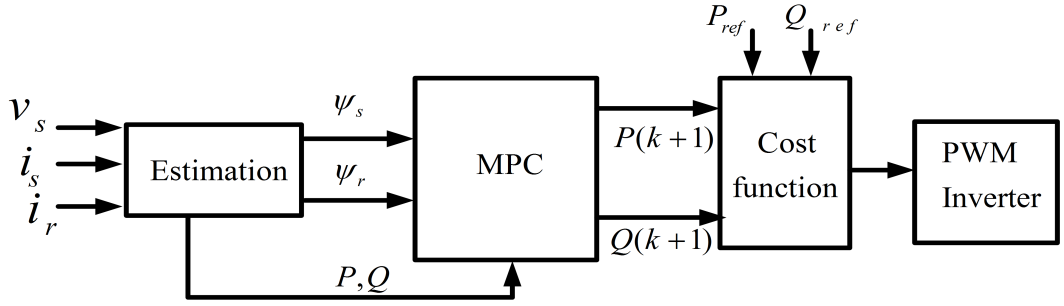

Figure 1.15: Schematic diagram of Model Predictive Controller

considers the control effort and the difference between the predicted outputs (active and reactive power) and the references as shown in Fig. 1.15. The prediction is calculated using a linearized state-space model of DFIG. In [52], MPC performance index is considered by using an augmented error system. Pitch angle and generator torque are controlled simultaneously to maximize energy capture and generator speed both in partial and full load regions.

In Fig. 1.15, the stator active and reactive powers, stator and rotor fluxes are first measured by using stator voltage v_s, stator current i_s and rotor current i_r. They are then fed into the system model together with all the possible voltage vectors in order to predict $P(k+1)$ and $Q(k+1)$. After this, $P(k+1)$ and $Q(k+1)$ together with the references P_{ref} and Q_{ref} are evaluated using the cost function. The voltage vector that minimises the cost function is applied during the next sampling period and appropriate PWM pulses are generated for inverter.

1.6.8 Linear Parameter Varying (LPV) H_∞ control

All the parameters for wind turbine has linear time invariant (LTI) characteristics in LPV H_∞ control [62, 63, 13] and the LPV controller matrices are computed as a weighted linear combination of these LTIs. Controller design requires that the nonlinear turbine dynamics are linearized about a specified operating point (OP). The LPV gain-scheduled controller for torque and pitch control of WECS is obtained by solving a convex optimization problem

with linear matrix inequalities (LMI) constraints that satisfy a defined H_∞ criterion.

1.7 Motivation

- From the literature review, it is observed that in most of the popular control schemes such as vector control, DPC and DTC, issues such as parametric uncertainities and power qualities are not addressed for a WECS. Therefore there is a need of designing robust controllers to handle the parametric uncertainties in a WECS.
- Wind speed is being intermittent in nature, it is necessary to devise a nonlinear system identification to obtain a nonlinear dynamic model of a WECS which can be subsequently used for developing an adaptive controllers.

1.8 Objectives of the thesis

- To develop a control algorithm for DFIG to achieve robustness for parameteric variations for controlling active and reactive power connected to grid.
- To develop an effective system identification for wind turbine model connected to DFIG based WECS.
- To design torque and pitch control schemes for the wind turbine using the identified wind turbine model.
- To generate appropriate PWM pulses for controlling both rotor side and grid side voltage source converters. With proper PWM switching, DC link voltage, reactive power and power factor are regulated on grid side and electromagnetic torque pulsations are eliminated on rotor side.
- To develop a 2kW laboratory DFIG WECS prototype for validating the proposed control strategy experimentally.
- The proposed control strategies are to be simulated in MATLAB/SIMULINK and implemented in real time (RT) Lab set up.

1.9 Outline of the Thesis

The thesis is organised as follows.

Chapter 2 presents torque and pitch control of wind turbine using sliding mode control. The performances of the SMC are compared with conventional proportional integral (PI) and linear parameter varying (LPV) controllers.

In *Chapter 3*, NARMAX model has been proposed along with on-line adaptive Recursive Least squares (RLS) algorithm. For optimisation of DFIG output power and speed regulation, Nonlinear Adaptive Model Predictive Controller (NAMPC) technique has been devloped for torque and pitch control of wind turbine.

In *Chapter 4*, A state space model for DFIG is derived. Using this state space model, state feedback controller has been developed with linear quadratic regulator optimal preview controller (LQROPC) with stator voltage oriented control (SVOC) technique. This controller has been implemented by considering the rotor current control dynamics. A 2 kW DFIG based WECS has been developed for real-time control of active and reactive power.

In *Chapter 5*, stator active and reactive power are controlled by considering the control variables such as rotor voltages(quadrature and direct axes) respectively. A new sliding mode controller has been proposed. The robustness of the WECS has been verified with Lyapunov theory. Results have been analysed by comparing the performances of the three different controllers such as field oriented control, direct torque control and proposed LQROPC technique.

Chapter 6 provides the overall conclusions of the thesis together with the contributions made. Further suggestions for future work are also provided therein.

Chapter 2

Sliding Mode Torque and Pitch Controller Design for a Wind Energy Conversion System

2.1 Introduction

WECS consists of a variable speed wind turbine model coupled to a wind generator. Wind generator connected to wind turbine shaft gives variable voltage which is further rectified and placed at the input terminal of voltage source converter. Since wind velocity always fluctuates from time to time, there is a concern for controlling the speed of wind turbine for regulating the output power. If the wind speed increases beyond the rated speed, turbine blades are damaged due to heavy wind gust and the output power decreases. So, pitch control is a better alternative for controlling wind turbines beyond the rated speed. A number of controllers such as Linear parameter varying(LPV), H_∞ control, Model Predictive Control (MPC) and gain scheduling control have been proposed in literature for torque and pitch control of wind turbines.

A gain scheduling controller for torque and pitch controller is proposed in [64, 65, 66], which changes the controller gains with variation of wind speed or other parameters. This means that accurate wind speed should be available to the controller. But the wind speed is usually

measured on the tower and does not represent the wind speed at the turbine plant, which makes the practical implementation of gain scheduling very difficult [67]. A pitch control has been designed that provides enhanced DFIG wind turbine performance through disturbance attenuation. However the drawback of this method is that, external disturbance is considered that represents the driving signals generating the disturbances, instead of considering the actual disturbances in WECSs. The variable pitch control can be achieved by exact linearization of the first order wind power system based on differential geometry method [68]. This is a nonlinear control, but its model is too simple, meanwhile it yields poor performance and bad robustness. In [55], pitch angle and generator torque are controlled simultaneously to provide optimal regulation of the generated power and the generator speed while minimising torsional torque fluctuations in the drive train and pitch actuator activity. In order to cope up with the non-linearity in the WECS and the continuous variation in the operating point, a multiple model predictive controller is proposed to provide near optimal performance within the entire operating region. In [62], the rotational speed is controlled by means of the generator torque under partial-load conditions and by means of the pitch angle under full-load operation. For wind speeds below rated speed, Look Up Table(LUT) builds the static torque speed reference curve for maximum energy capture. In high wind speeds, the PI controller used for pitch control regulates the rotational speed at its rated value and regulates the power to rated value. In [63, 13], design of WECS has been proposed in two parts. The first part describes the modeling of the subsystems of WECS and introduces the multiobjective H_∞ control concept. The second part deals with the implementation of the control algorithm. The mechanical dynamics are regulated by a proportional integral (PI)-based pitch angle controller, while the generator torque characteristic governs the power electronic converters via H_∞ control. Controller design requires that the nonlinear turbine dynamics be linearized about a specified operating point. Each fixed value of the parameter vector p has linear time invariant (LTI) systems, and the LPV controller matrices are computed as a weighted linear combination of these LTIs. The LPV gain-scheduled controller for $\Gamma_{G\,\mathrm{Re}\,f}$ is obtained by solving a convex optimization problem with LMI constraints that satisfy a defined H_∞ criterion. In [56], the proposed control strategy is described for the whole operating region of the wind turbine, i.e., both partial and full load regimes. Pitch

angle and generator torque are controlled simultaneously to maximize energy capture and generator speed. In [57], the control system has multiple objectives for both partial and the full load region. In the partial load region, the controller is implemented for the maximum power point tracking (MPPT). The generator speed ω_G and the pitch angle β should be controlled in a way such that the power coefficient $C_p(\lambda, \beta)$ is maximized. In the full load region, the controller is required to maintain both the generator power and the generator speed at their rated values P_{Grat} and ω_{Grat}. These objectives can be achieved by regulating the desired pitch angle β and/or the generator torque set point T_G.

2.1.1 Objectives

- To design a sliding mode (SM) controller for speed and power regulation of DFIG connected to wind turbine by using torque and pitch control of wind turbine.
- The proposed SM control algorithm is implemented using MATLAB/SIMULINK.
- To implement the proposed control algorithm in FPGA.

2.2 Modelling of WECS

Fig. 2.1 shows block diagram of a WECS. The power generated from the DFIG can be controlled by a power electronics interface. In Fig. 2.1, mechanical power obtained from wind turbine is fed to DFIG which generates electrical power fed to grid. DFIG feeds power to grid from both rotor side converter (RSC) and grid side converter (GSC). PWM pulses to RSC abd GSC are obtained through torque and pitch control of WECS. Finally these two controllers were implemented in FPGA and the results were compared with that of LPV and PI controllers.

2.2.1 Wind Turbine Modeling

Wind turbine plays a vital role for converting wind kinetic energy to mechanical energy by using rotor blades. Since energy source for a WECS is wind kinetic energy, wind speed plays a key role in relation to the maximum power point. However, the power output of the wind

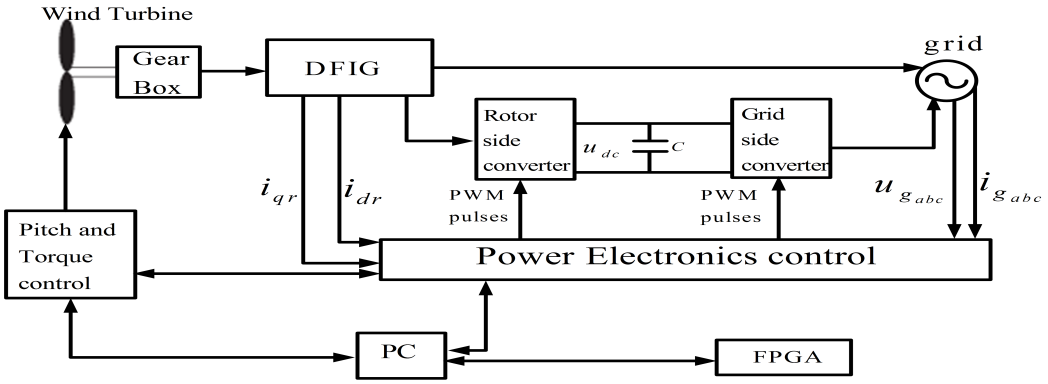

Figure 2.1: Schematic diagram of WECS

turbine can be regulated by adjusting the blade pitch angle or by controlling the generators torque or speed. Aerodynamic power of a wind turbine is given by [69]

$$P_w = \frac{C_P(\lambda,\beta)\rho\Lambda {v_w}^3}{2} \tag{2.1}$$

where $\Lambda = \pi R^2$

$$\begin{aligned} C_P(\lambda,\beta) &= a_1(\beta)\lambda^2 + a_2(\beta)\lambda^3 + a_3(\beta)\lambda^4 \\ a_1(\beta) &= a_{10} + a_{11}\beta + a_{12}\beta^2 + a_{13}\beta^3 + a_{14}\beta^4 \\ a_2(\beta) &= a_{20} + a_{21}\beta + a_{22}\beta^2 + a_{23}\beta^3 + a_{24}\beta^4 \\ a_3(\beta) &= a_{30} + a_{31}\beta + a_{32}\beta^2 + a_{33}\beta^3 + a_{34}\beta^4 \end{aligned} \tag{2.2}$$

where $a_{10} - a_{34}$ are performance constants of a wind turbine, tip speed ratio $\lambda = \frac{\omega_m R}{v_w}$, β is the pitch angle, C_P is the power coefficient, ω_m is turbine rotational speed, ρ is the air density in gm/m^3 , Λ is the cross sectional area of the turbine,V_w is the wind velocity and R is the radius of turbine shaft.

2.2.2 Drive Train Subsystem

The drive train model for WECS is derived in [70, 71] and is represented as

$$\tau_e - T_w = J\frac{d\omega_m}{dt} + B\omega_m \tag{2.3}$$

where J denotes the total inertia, τ_e is the electromagnetic torque of the generator, T_w is the input mechanical torque extracted from aerodynamic power, B is the effective friction coefficient, ω_m is rotor angular speed.

$$\tau_e = \frac{P_{em}}{\omega_m} \tag{2.4}$$

$$\dot{\omega}_e = \frac{P_m}{J}\left(\frac{T_w}{N} + \tau_e\right) \tag{2.5}$$

$$\omega_e = P_m\omega_r = P_m N\omega_m \tag{2.6}$$

where P_{em} is the electromagnetic power of the generator, ω_r is generator rotor speed, ω_e is the electrical rotor speed. P is the number of pole pairs and N denotes the gear ratio.

2.2.3 Voltage-Current relationships applied in dq reference frame using generator convention

From [22], stator and rotor voltages in d and q axes are given as

$$\begin{bmatrix} u_{ds} = R_s i_{ds} + \omega_s((L_s + L_m)i_{qs} + L_m i_{qr}) \\ u_{qs} = R_s i_{qs} - \omega_s((L_s + L_m)i_{ds} + L_m i_{dr}) \\ u_{dr} = R_r i_{dr} + s\omega_s((L_r + L_m)i_{qr} + L_m i_{qs}) \\ u_{qr} = R_r i_{qr} - s\omega_s((L_r + L_m)i_{dr} + L_m i_{ds}) \end{bmatrix} \tag{2.7}$$

where s=slip, suffixes s and r represent stator and rotor respectively. Generation of the

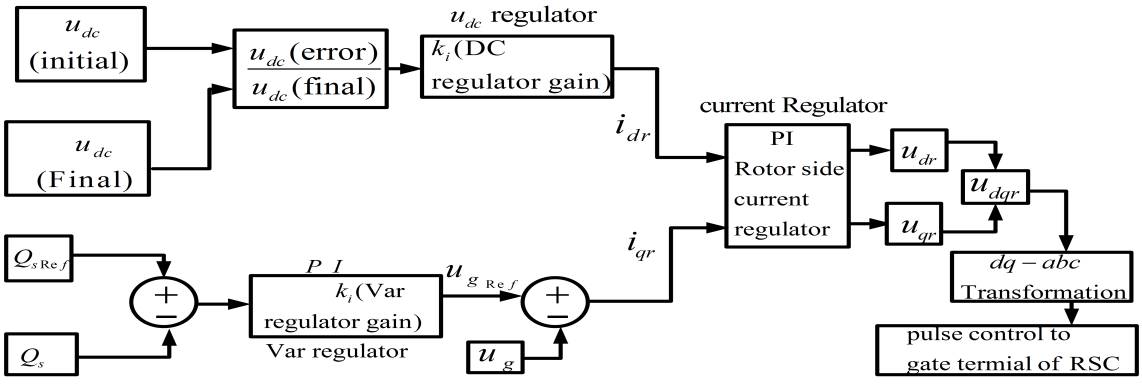

Figure 2.2: Grid side converter control system

firing pulses for the grid side converter is described in Fig. 2.2. The firing pulses can be derived from the regulated DC voltage and the reactive power from the grid. The three phase quantities are converted into dq reference values for Proportional Integral (PI) control and later converted again from $dq - abc$ for generating firing pulses to the converter on grid side. The firing pulses for the rotor side converter is explained in Fig. 2.3. The firing pulses

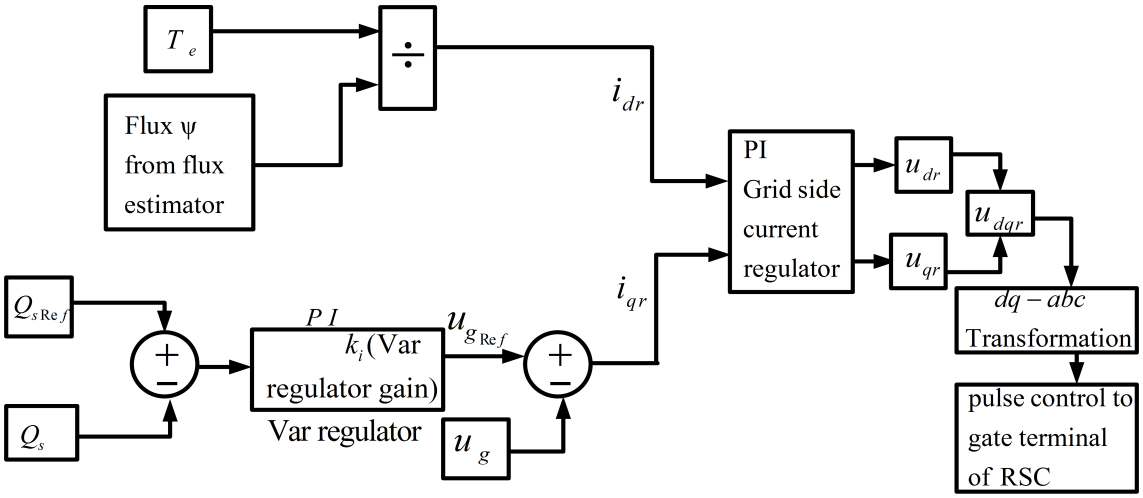

Figure 2.3: Rotor side converter control system

are derived from the electromagnetic torque, stator flux estimation and the reactive power from the grid. Fig. 2.4 depicts the estimation of the stator flux from stator u_{dqs} and i_{dqs} as

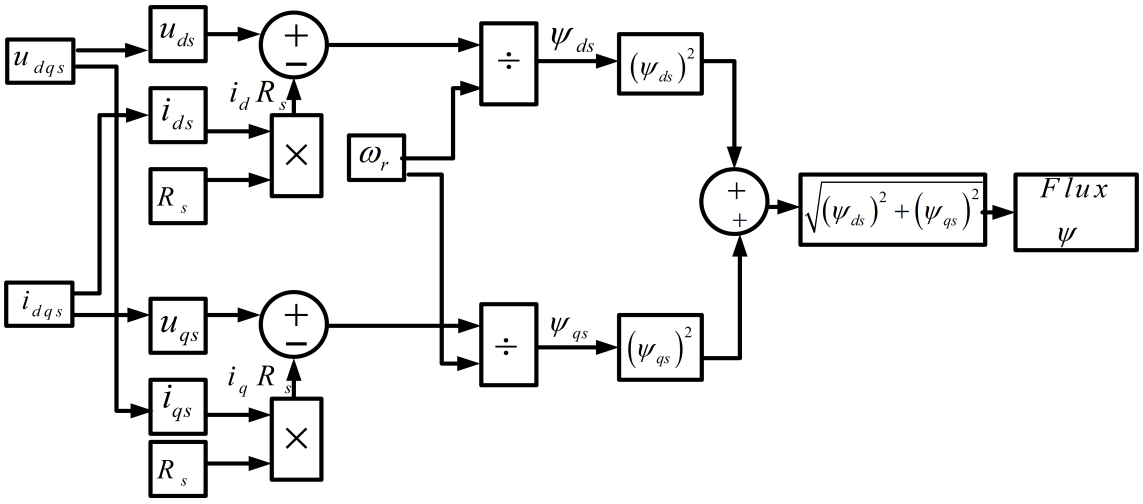

Figure 2.4: Stator flux estimator

given in equations (2.8),(2.9),(2.10),(2.11)

The electromagnetic torque τ_e is obtained from the rotor speed of generator and the measured value of power. If the speed is less than the nominal speed, then reference torque is calculated by dividing power with mechanical angular speed and the torque control comes into picture as shown in Fig. 2.5. If the speed is above the nominal speed then the pitch control is activated as shown in Fig. 2.6.

Eq(2.7) can be splitted and represented in matrix form as given in eq(2.8).

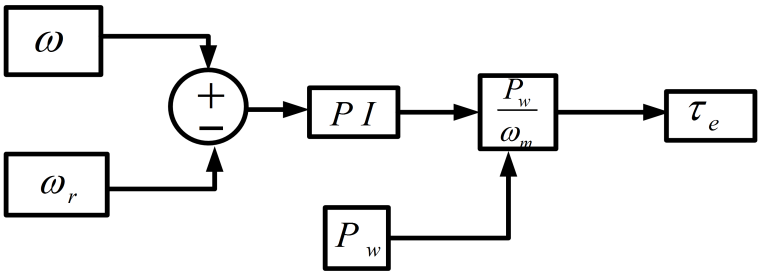

Figure 2.5: Torque control on rotor side converter

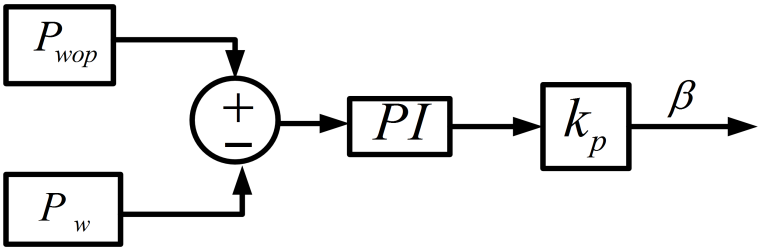

Figure 2.6: Pitch control of WECS

$$\begin{bmatrix} u_{ds} \\ u_{qs} \\ u_{dr} \\ u_{qr} \end{bmatrix} = [R^*] \begin{bmatrix} i_{ds} \\ i_{qs} \\ i_{dr} \\ i_{qr} \end{bmatrix} + \frac{d}{dt} \begin{bmatrix} \psi_{ds} \\ \psi_{qs} \\ \psi_{dr} \\ \psi_{qr} \end{bmatrix} + [\Omega^*] \frac{d}{dt} \begin{bmatrix} \psi_{ds} \\ \psi_{qs} \\ \psi_{dr} \\ \psi_{qr} \end{bmatrix} \tag{2.8}$$

$$R^* = \begin{bmatrix} R_s & 0 & 0 & 0 \\ 0 & R_s & 0 & 0 \\ 0 & 0 & R_r & 0 \\ 0 & 0 & 0 & R_r \end{bmatrix} \tag{2.9}$$

$$\Omega^* = \begin{bmatrix} 0 & -\omega & 0 & 0 \\ \omega & 0 & 0 & 0 \\ 0 & 0 & 0 & -(\omega - \omega_r) \\ 0 & 0 & (\omega - \omega_r) & 0 \end{bmatrix} \tag{2.10}$$

where ω is the rotating speed of arbitrary reference frame, ω_r is the rotor electrical angular speed(rad/sec)

$$\begin{bmatrix} \psi_{ds} \\ \psi_{qs} \\ \psi_{dr} \\ \psi_{qr} \end{bmatrix} = \begin{bmatrix} L_s & 0 & L_m & 0 \\ 0 & L_s & 0 & L_m \\ L_m & 0 & L_r & 0 \\ 0 & L_m & 0 & L_r \end{bmatrix} \begin{bmatrix} i_{ds} \\ i_{qs} \\ i_{dr} \\ i_{qr} \end{bmatrix} \tag{2.11}$$

The scheduling constant k_p is given as follows which has been used in Fig. 2.7.

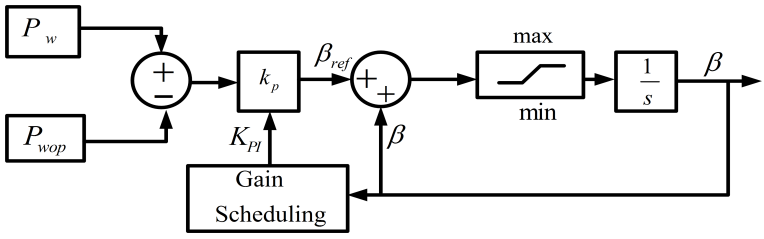

Figure 2.7: Gain scheduling for pitch control

$$K_{PI} = \begin{Bmatrix} 1 & for\ \text{-}3^\circ < \beta \leq 0^\circ \\ \frac{\beta}{15} + 1 & for\ 0^\circ < \beta \leq 30^\circ \\ 3 & \beta > 30^\circ \end{Bmatrix} \tag{2.12}$$

Selection of k_p is made by trial and error, based on minimising the deviations from the set point, without any excessive control action and without causing instability.

2.2.4 FPGA Design

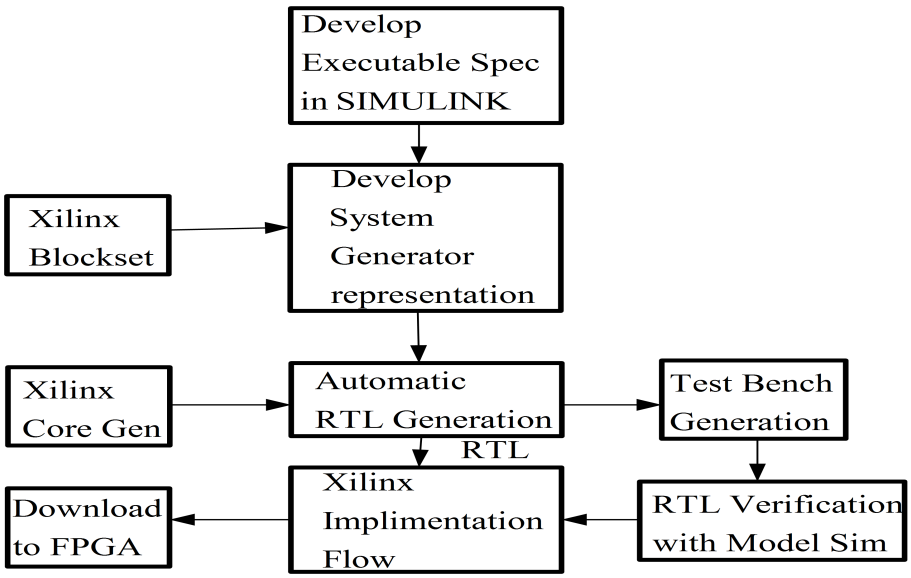

Figure 2.8: Design Flow in FPGA implementation

System Generator tool in Xilinx toolbox works within the Simulink model-based design methodology. An executable spec is created using the standard Simulink block sets as shown in Fig. 2.8. Once the functionality and basic dataflow issues have been defined, System Generator can be used to specify the hardware implementation details for the Xilinx devices. System Generator uses the Xilinx block set for Simulink and will automatically invoke Xilinx Core Generator to generate highly optimized netlists for building blocks. System Generator can execute all the downstream implementation tools to product a bit stream for programming the FPGA. An optional test bench can be created using test vectors extracted from the Simulink environment for use with ModelSim or the Xilinx ISE Simulator.

2.2.5 JTAG(Joint Test Action Group) Co-Simulation

The symbol for JTAG Co-Simulation in simulink is given in Fig. 2.9 JTAG boundary scan started as a method of testing ICs and their interconnections using a shift register built into the chip so that inputs could be shifted-in and the resulting outputs could be shifted-out using only four I/O pins (clock, input data, output data, and state machine mode control). This eliminated the need for complex, expensive cards for low-speed probing of IC

Figure 2.9: JTAG Co-Simulation

I/O pins.JTAG is used for debugging software, hardware co-simulation. When a model is implemented for JTAG hardware co-simulation, a new library is created that contains a custom JTAG co-simulation block with ports that match the gateway names from the original model. The co-simulation block interacts with the FPGA hardware platform during a Simulink simulation. Simulation data that is written to the input ports of the block are passed to the hardware by the block.
System Generator provides "Hardware Co-Simulation", making it possible to incorporate a design running in an FPGA directly into a Simulink simulation. Hardware Co-Simulation compilation targets automatically create a bit stream and associate it to a block. When the design is simulated in Simulink, results for the compiled portion are calculated in hardware. This allows the compiled portion to be tested in actual hardware and can speed up simulation dramatically. A controller area network (CAN bus) is a vehicle bus standard designed to allow devices to communicate with each other in applications without a host computer. USB(Universal Serial Bus), is an industry standard developed in a bus for connection, communication, and power supply between computers and electronic devices.

2.3 SMC design for pitch and torque control

In this section, sliding mode approach to design torque and pitch controllers is presented. The wind power system is represented by state space equations. The wind power system is operated within the specific range of wind speed. If the wind speed is out of the range i.e above 25m/sec, then the wind turbine will be off and does not generate the power. Similarly the pitch angle should be within the prescribed limits as explained above in gain scheduling pitch control mechanism, beyond which the wind power system will be off and does not generate the power.

2.3.1 Torque controller design

By substituting equations (2.8)-(2.11) into rotor voltage equations of (2.7), the following dynamic equations for rotor current can be obtained.

$$\frac{di_{dr}}{dt} = -\frac{R_r}{\sigma} i_{dr} - \frac{L_m}{\sigma L_s} \underbrace{(u_{ds} - R_s i_{ds})}_{\frac{d\psi_{ds}}{dt}} - \underbrace{\omega_r \left(i_{qr} + \frac{L_m}{\sigma L_s} \psi_{qs} \right)}_{cross\ coupling\ term} + \frac{1}{\sigma} u_{dr} \tag{2.13}$$

$$\frac{di_{qr}}{dt} = -\frac{R_r}{\sigma} i_{qr} - \frac{L_m}{\sigma L_s} \underbrace{(u_{qs} - R_s i_{qs})}_{\frac{d\psi_{qs}}{dt}} - \underbrace{\omega_r \left(i_{dr} + \frac{L_m}{\sigma L_s} \psi_{ds} \right)}_{cross\ coupling\ term} + \frac{1}{\sigma} u_{qr} \tag{2.14}$$

where $\sigma = L_r - \frac{L_m^2}{L_s}$ Electromagnetic torque of DFIG is controlled by SMC given by

$$\begin{aligned} \tau_e &= \frac{3PL_m}{2L_s} (i_r \times \psi_s) \\ &= \frac{3PL_m}{2L_s} (i_{dr} \times \psi_{qs} - i_{qr} \times \psi_{ds}) \end{aligned} \tag{2.15}$$

where

$$\begin{aligned} \psi_{ds} &= \int (u_{ds} - R_s i_{ds}) dt \\ \psi_{qs} &= \int (u_{qs} - R_s i_{qs}) dt \end{aligned} \tag{2.16}$$

2.3.2 Derivation of sliding mode control law for torque control

Let the switching variable for electromagnetic torque be chosen as

$$S_{\tau_e} = e_{\tau_e} + k_{\tau_e} \int e_{\tau_e} dt \tag{2.17}$$

$$e_{\tau_e} = \tau_e^* - \tau_e \tag{2.18}$$

where k_{τ_e} denotes a positive constant.

The control objective is to drive e_{τ_e} to zero by considering the switching function for (2.17)

as follows

$$\dot{S}_{\tau_e} = (\dot{\tau}_e^* - \dot{\tau}_e) + k_{\tau_e} (\tau_e^* - \tau_e) \tag{2.19}$$

From (2.15),one obtains the following torque equation

$$\dot{\tau}_e = \frac{3PL_m}{2L_s} \left(i_{dr}\dot{\psi}_{qs} + \dot{i}_{dr}\psi_{qs} - i_{qr}\dot{\psi}_{ds} - \dot{i}_{qr}\psi_{ds} \right) \tag{2.20}$$

Substituting (2.13),(2.14) and (2.20) in (2.19) yields

$$\dot{S}_{\tau_e} = g_{\tau_e} - k \underbrace{[a_{11}\ a_{12}]}_{B} \begin{bmatrix} u_{dr} \\ u_{qr} \end{bmatrix} \tag{2.21}$$

where

$$\begin{aligned} g_{\tau_e} &= g_1 \left(i_{dr}, i_{qr}, u_{ds}, u_{qs}, \omega_r, \psi_{dr}, \psi_{qr}, i_{ds}, i_{sq}, e_{\tau_e}, \dot{\tau}_e, k_{\tau e} \right) \\ a_{11} &= P\psi_{qs},\ a_{12} = -P\psi_{ds},\ k = \frac{3L_m}{2\sigma L_s} \end{aligned} \tag{2.22}$$

For approaching zero sliding surface, equivalent following control signals are assumed as

$$\begin{bmatrix} u_{dr_{eq}} \\ u_{qr_{eq}} \end{bmatrix} = \frac{B^{-1}}{k} g_{\tau_e} \tag{2.23}$$

Substituting (2.23) in (2.21) yields

$$\dot{S}_{\tau_e} = 0 = \dot{e}_{\tau_e} + k_{\tau_e} e_{\tau_e} \tag{2.24}$$

Equation (2.24) shows that error in contol variables $u_{dr_{eq}}$ and $u_{qr_{eq}}$ tends to zero. But the control variables in (2.23) are dependent on DFIG parameters. To compensate for the parameter deviations in the DFIG, the following terms are introduced as given in eq(2.25).

$$\begin{aligned} u_{dr} &= u_{dr_{eq}} + u_{dr_c} \\ u_{qr} &= u_{qr_{eq}} + u_{qr_c} \end{aligned} \tag{2.25}$$

where u_{dr_c} and u_{qr_c} are compensation control variables defined as

$$\begin{bmatrix} u_{dr_c} \\ u_{qr_c} \end{bmatrix} = B^{-1} \underbrace{c_{\tau_e} sgn S_{\tau_e}}_{v_{\tau 1}} \tag{2.26}$$

where c_{τ_e} is the positive constant. Equation(2.21) can be rewritten due to consideration of uncertainities or offset change in control variables u_{dr_c} and u_{qr_c} which yields

$$\dot{S}_{\tau_e} = g_{\tau_e} - kB \begin{bmatrix} u_{dr} \\ u_{qr} \end{bmatrix} + d_{r2} \tag{2.27}$$

By substituting eq(2.23),(2.25),(2.26) in the eq(2.27) the following expression is obtained as

$$\dot{S}_{\tau_e} = kc_{\tau_e} sgn(S_{\tau_e}) + d_{r2} \tag{2.28}$$

Equations (2.23),(2.25) and (2.26) are verified for convergence, by considering Lyapunov function chosen as

$$V = \frac{1}{2} S_p^T S_p \geq 0 \tag{2.29}$$

For convergence, derivative of the Lyapunov function V must be negative definite, i.e.

$$\dot{V} = S_p^T \dot{S}_p \leq 0 \tag{2.30}$$

Substituting (2.28) in (2.30) yields

$$\dot{V} = S_{\tau_e} kc_{\tau_e} sgn(S_{\tau_e}) + S_{\tau_e} d_{r2} \leq 0 \tag{2.31}$$

In equation (2.31), control variables converge to zero, if

$$c_{\tau_e} \gg \frac{|d_{r2}|}{B} \tag{2.32}$$

The second term in the control signal in (2.26) is discontinuous due to presence of the *sgn* function. In order to obtain a continuous signal, $v_{\tau 1}$ in (2.26) is passed through low pass

filter(LPF). Equation (2.26) can be modified as follows

$$\begin{bmatrix} u_{dr_c} \\ u_{qr_c} \end{bmatrix} = B^{-1} v_{\tau av} \tag{2.33}$$

where $v_{\tau av}(s) = \frac{1}{1+sT} v_{\tau 1}(s)$, T is the time constant of the LPF. Thus, the discontinuous signal $v_{\tau 1}$ becomes only part of the internal process and the control variables are finally continuous . From equations(2.23),(2.25) and (2.33), the expression of the torque control signal is

$$\begin{bmatrix} u_{dr} \\ u_{qr} \end{bmatrix} = B^{-1} g_{\tau_e} + B^{-1} v_{\tau_e av} \tag{2.34}$$

The second term in eq(2.34), makes the torque control system robust, which is independent of system parameters.

2.3.3 Pitch controller design

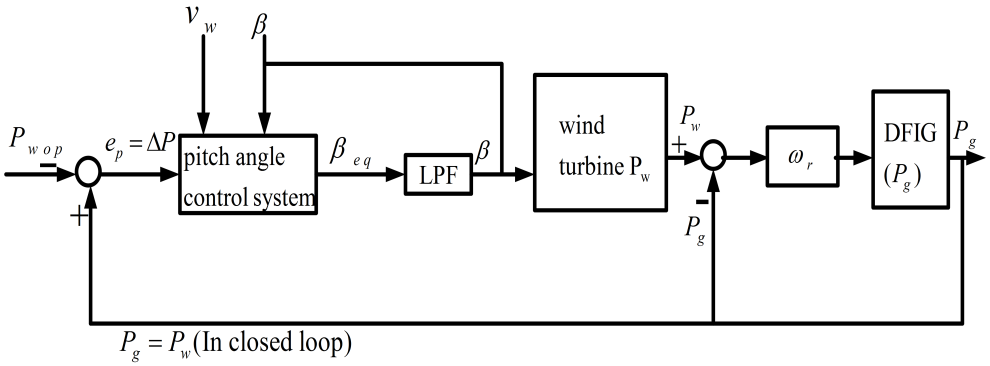

Figure 2.10: Structure of Pitch control system of a WECS

Fig. 2.10 shows the structure of the pitch control system of a DFIG WECS. In this control scheme, the control input to the turbine is pitch angle β, which is obtained from pitch control system. In pitch control system, β is the control variable and error e is taken as the input which is obtained by taking the difference of the output power (P_g) of DFIG and the reference power (P_{wop}). The output of the pitch control system is β_{eq}, which is discontinuous due to switching function in sliding mode controller. β_{eq} is passed through a

Low pass filter which converts β_{eq} into a continuous variable which is given as the input to the wind turbine.

In Fig. 2.11, input to the wind turbine is β and output is aerodynamic power P_w computed

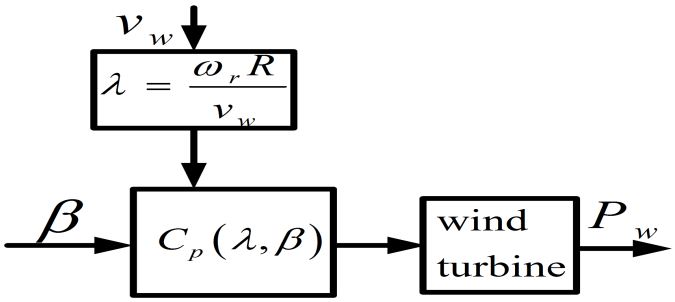

Figure 2.11: Wind turbine model

from equations (2.1) and (2.2). Control quantity of the pitch angle is given by [54], $G(\beta) = \frac{\Delta\beta}{\Delta P}$.

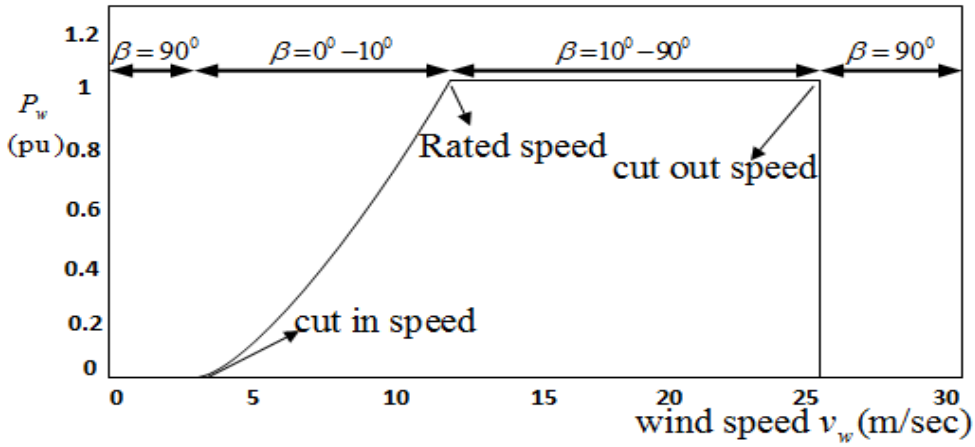

Figure 2.12: Pitch angle characteristics of wind turbine

Fig. 2.12, shows the variation of β in different regions, namely below, above and the rated speed regions of the wind turbine. The wind turbine comes to a halt position by taking 90 degrees angle after cutout region and below cut-off region.

Output power of DFIG wind turbine is given by

$$P_g = \frac{-3s(s+1)E_2^2 r_2}{(r_2 - sr_1)^2 + s(x_1 + x_2)^2} \tag{2.35}$$

$$s = \frac{\omega_s - \omega_r}{\omega_s} \tag{2.36}$$

$$\omega_r = \sqrt{\frac{2}{J}\int (P_w - P_{wop}) \quad dt} \tag{2.37}$$

If $\omega_r > \omega_s$, then slip is negative, DFIG runs above the rated speed and generates power. where J is moment of inertia of a wind turbine, ω_s is angular synchronous speed, P_g is generator output power, P_{wop} is the reference operating power, E_2 is rotor voltage, r_1 is stator resistance, r_2 is rotor resistance, x_1 is stator reactance, x_2 is rotor reactance, s denotes slip.

Since, wind turbine has large inertia and a lossless system is considered, at steady state $P_g = P_w$ and P_w can be approximated as

$$\begin{aligned} P_w &= a_1(\beta) + a_2(\beta)v_w^2 \\ a_1(\beta) &= a_{11} + a_{12}\beta + a_{13}\beta^2 + a_{14}\beta^3 \\ a_2(\beta) &= a_{21} + a_{22}\beta + a_{23}\beta^2 + a_{24}\beta^3 \end{aligned} \tag{2.38}$$

2.3.4 Derivation of sliding mode control law for pitch angle control

For controlling the power generated from wind turbine, SMC is developed by considering the switching variable as

$$S_p = e_p + k_p \int e_p dt \tag{2.39}$$

Fig. 2.13 shows the structure of the proposed sliding mode control scheme developed for pitch angle control. Error in power e_p is taken as input to SMC which generates the control signal β_c and pitch angle control system generates β_{eq} which generates β according to eq(2.47). Then β is given as input to blades of wind turbine for controlling the mechanical power P_w shown in (2.1) which ultimately regulates the output power P_g given in (2.35).

$$e_p = (P_w - P_{wop}) \tag{2.40}$$

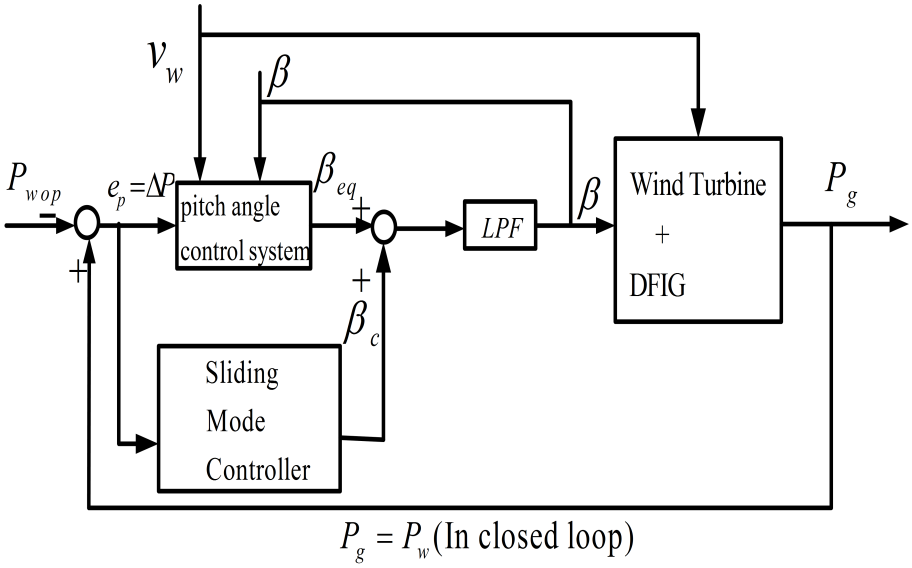

Figure 2.13: Pitch angle control system using SMC

where the integral of e_p, followed by positive weighted constant (gain) k_p approaches the steady State error of P_w to zero.

The error equation e_p is linearised as follows

$$e_p = \Delta P = P_w - P_{wop} = \frac{\partial P_w}{\partial v_w}\Delta v_w + \frac{\partial P_w}{\partial \beta}\Delta\beta = \zeta \Delta v_w + \xi \Delta\beta \tag{2.41}$$

where $\zeta = \frac{\partial P_w}{\partial v_w} = \frac{\rho \Lambda v_w}{2}\left(3C_P v_w - R\frac{\partial C_P}{\partial \lambda}\right)$,
$\xi = \frac{\rho \Lambda {v_w}^3}{2}\frac{\partial C_P}{\partial \beta}$

The control objective is to drive e_p to zero by considering the switching function for (2.39) as

$$\dot{S}_p = \left(\dot{P}_w - \dot{P}_{wop}\right) + k_p\left(P_w - P_{wop}\right) \tag{2.42}$$

From [72], $\dot{P}_w$ can be written as

$$\begin{aligned} \dot{P}_w &= \dot{a}_1(\beta) + \dot{a}_2(\beta) v_w^2 \\ \dot{a}_1(\beta) &= a_{12} + 2a_{13}\beta + 3a_{14}\beta^2 \\ \dot{a}_2(\beta) &= a_{22} + 2a_{23}\beta + 3a_{24}\beta^2 \end{aligned} \tag{2.43}$$

Substituting eq(2.43) and (2.1) in (2.42) yields

$$\dot{S}_p = f_p + H\left[\beta\right] \tag{2.44}$$

where $f_p = \left(C_p, \omega_r, \dot{P}_{wop}, k_p, e_p\right)$, $H = \frac{\rho\Lambda}{2}$
Assume the structure of the equivalent control signal in (2.44) as

$$\left[\quad \beta_{eq}\right] = H^{-1} f_p \tag{2.45}$$

Substituting (2.45) in (2.44) yields

$$\dot{S}_p = 0 = \dot{e}_p + k_p e_p \tag{2.46}$$

Equation (2.46) shows that error in contol variable β_{eq} tends to zero. But the control variable in (2.45) are dependent on non linear dynamics of aerodynamic power of wind turbine, which causes deviations in control variable. To compensate the deviations, second term is introduced in the control signal as

$$\beta = \beta_{eq} + \beta_c \tag{2.47}$$

where β_c is the compensation control variable defined as

$$\left[\beta_c\right] = H^{-1} \underbrace{k_{pc} sgn\left(S_p\right)}_{v_{p1}} \tag{2.48}$$

Equation (2.44) can be rewritten as

$$\dot{S}_p = f_p + H\left[\beta\right] + d_{r1} \tag{2.49}$$

where k_{pc} is the positive constant, d_{r1} is due to non-linearity, the stochastic variations of the input power fluctuations resulting from wind speed variations, and the presence of physical constraints on the variables of the controlled system, such as limits on the pitch angle, pitch angle rate.

By substituting (2.45)(2.47)(2.48) into (2.49), the following expression is obtained

$$\dot{S}_p = Hk_{pc}sgn(S_p) + d_{r1} \tag{2.50}$$

Equations (2.45)(2.47)(2.48) are used to verify whether the switching variables are converging to zero, by considering Lyapunov function as

$$V = \frac{1}{2}S_p^T S_p \geq 0 \tag{2.51}$$

For converge, its derivative must be negative, that is

$$\dot{V} = S_p^T \dot{S}_p \leq 0 \tag{2.52}$$

Substituting (2.50) in (2.52) yields

$$\dot{V} = S_p Hk_{pc}sgn(S_p) + S_p d_{r1} \leq 0 \tag{2.53}$$

In equation (2.53) , control variables converges to zero, if

$$k_{pc} \gg \frac{|d_{r1}|}{H} \tag{2.54}$$

According to (2.48) and (2.54), the robustness of control variables in (2.47) are restricted by the constraints in the pitch angle given by

$$\begin{aligned} &\Delta\beta_{\min} \leq \Delta\beta \leq \Delta\beta_{\max} \\ &\beta_{\min} \leq \beta \leq \beta_{\max} \end{aligned} \tag{2.55}$$

The second terms of control signal in (2.48) becomes discontinuous due to *sgn* function. To obtain a clear continuous signal, v_{p1} in (2.48) is passed through low pass filter(LPF). Equation (2.48) can be rewritten as

$$\left[\beta_c\right] = H^{-1}v_{pav} \tag{2.56}$$

where $v_{pav}(s) = \frac{1}{1+sT} v_{p1}(s)$, T is the time constant of LPF. Thus, the discontinuous signal v_{p1} becomes only part of the internal process and the control variables are finally continuous.

From equations (2.45),(2.47) and (2.56), the expression of the pitch control signal without any disturbance is obtained as

$$\left[\beta\right] = H^{-1} f_p + H^{-1} v_{pav} \tag{2.57}$$

The second term in eq(2.57), makes the pitch control system robust, which is independent of non linear dynamics of aerodynamic power of wind turbine.

2.4 Results and Discussion

The dynamics of WECS has been simulated in MATLAB/SIMULINK and implemented in FPGA. The developed sliding mode controller is applied for a wind turbine with a 2kW DFIG. Speed and power regulation of DFIG are regulated by SM controller in torque and pitch control of wind turbine and has been simulated in MATLAB/SIMULINK and implemented in FPGA. Sliding mode controllers for both torque and pitch control are implemented for a 2kW DFIG coupled with wind turbine. The rated wind speed is considered as of 12m/s, while the mean wind speed increases from 11m/s to 14m/s and then it is kept over the rated value with the wind turbulence and in the simulation the turbulence intensity is 8 percent. The pitch rate is assumed to be limited as 8deg/s. The simulation results are presented into two regions. The region $\omega_g \leq \omega^*{}_g$, the torque controller tries to maximize the generating power, while in the region $\omega_g \geq \omega^*{}_g$, the torque control and pitch control operate in harmony to regulate the DFIG inlet power. Various parameters are plotted i.e.wind speed, torque, pitch angle, DFIG generated power, three phase voltage, three phase current at DFIG stator terminals, rotor speed of DFIG and frequency at stator terminals of DFIG.

In Fig. 2.14, wind speed varies from 8 to 11 m/sec from 2 sec to 3.3 sec and remains constant after 3.3 sec. So the fluctuations in torque (Fig. 2.15)are observed. From (Fig. 2.15),

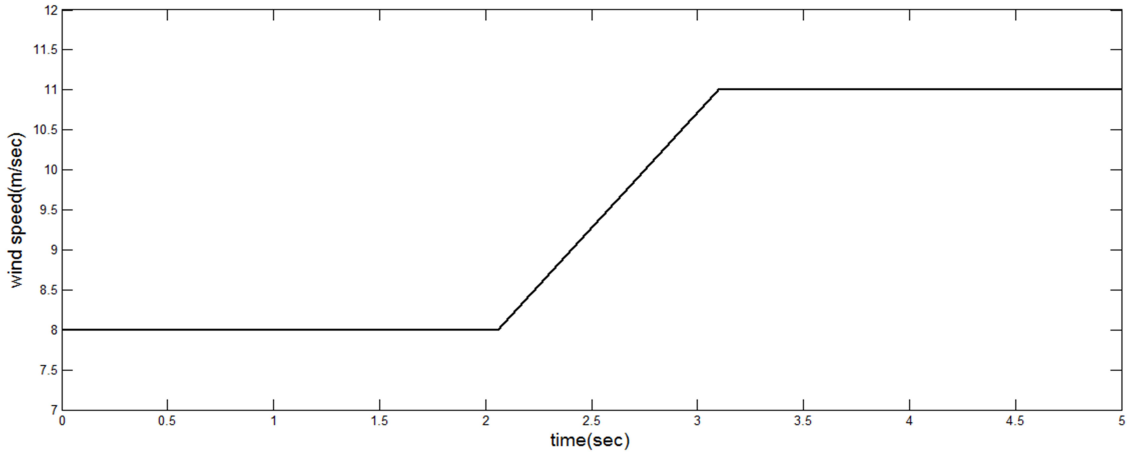

Figure 2.14: Variation of wind speed(m/sec) Versus time(sec)

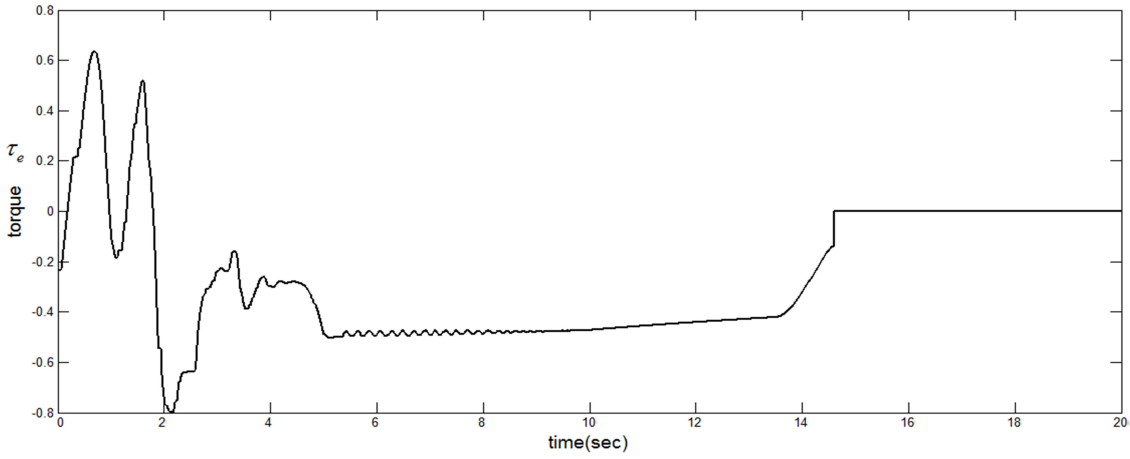

Figure 2.15: Electromagnetic torque(N-m) Versus time(sec)

it is observed that electromagnetic torque has fallen to -0.8 pu at 2 sec, causing abrupt changes in torque pulsations upto 3.3 sec and settling to 0 pu at 15 sec, after the rotor speed of generator reaches to 70% of the rated speed.

From Fig. 2.16, it is observered that power pulsations are from 2 sec to 3.3 sec and settling to 1 pu at 15 sec at rated speed of DFIG. Transients are observed in stator three phase voltage (Fig. 2.17), stator three phase current (Fig. 2.18), rotor speed of DFIG (Fig. 2.19), and frequency (Fig. 2.20) at 2sec.

In Fig. 2.21, the pitch angle varies from zero to 8 degrees during the maximisation of DFIG power generated and settling at stedy value at 7 degrees after transient period. By

using SMC torque and pitch controllers, transients are minimised and are regulated so that the parameters are reaching steady state values at 3.3 sec.

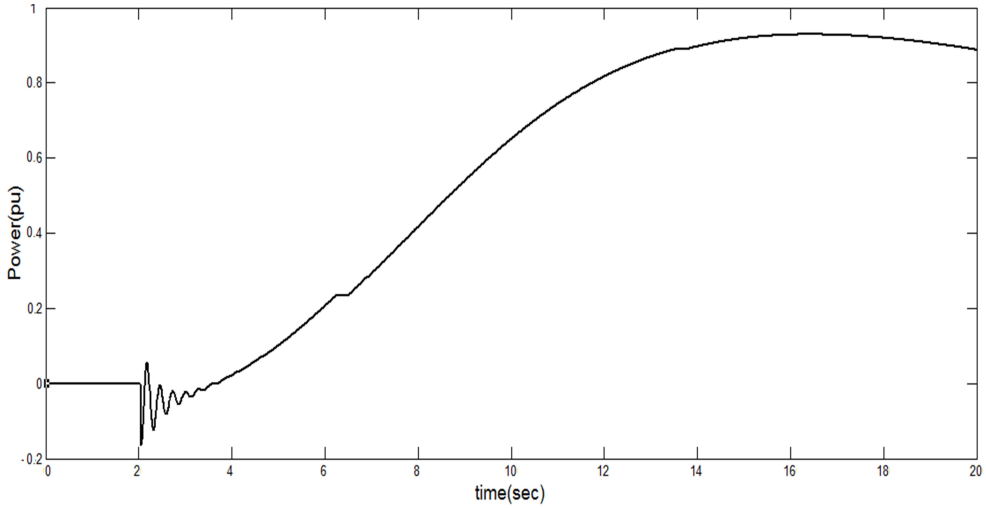

Figure 2.16: Generated power of DFIG(pu) versus time

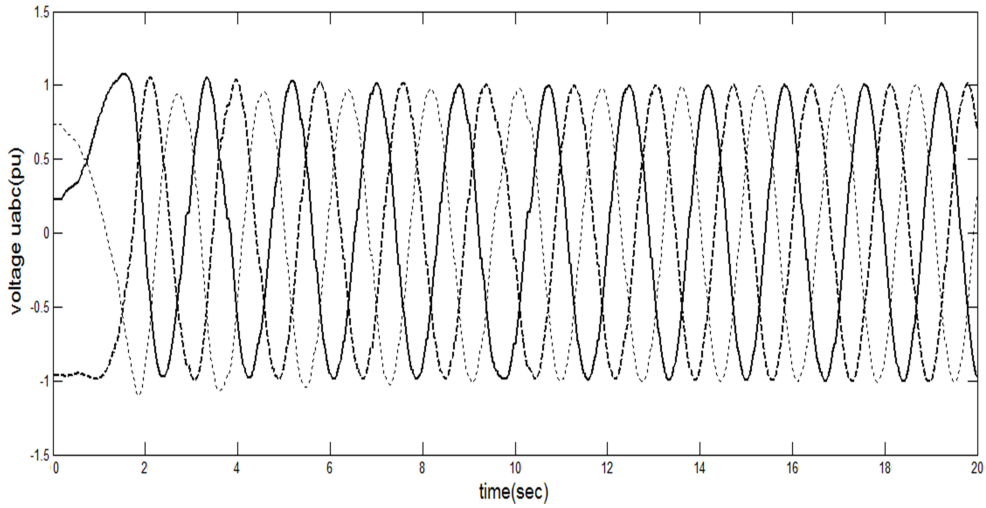

Figure 2.17: Three phase voltage at stator terminals u_{abc} (V) versus time(sec)

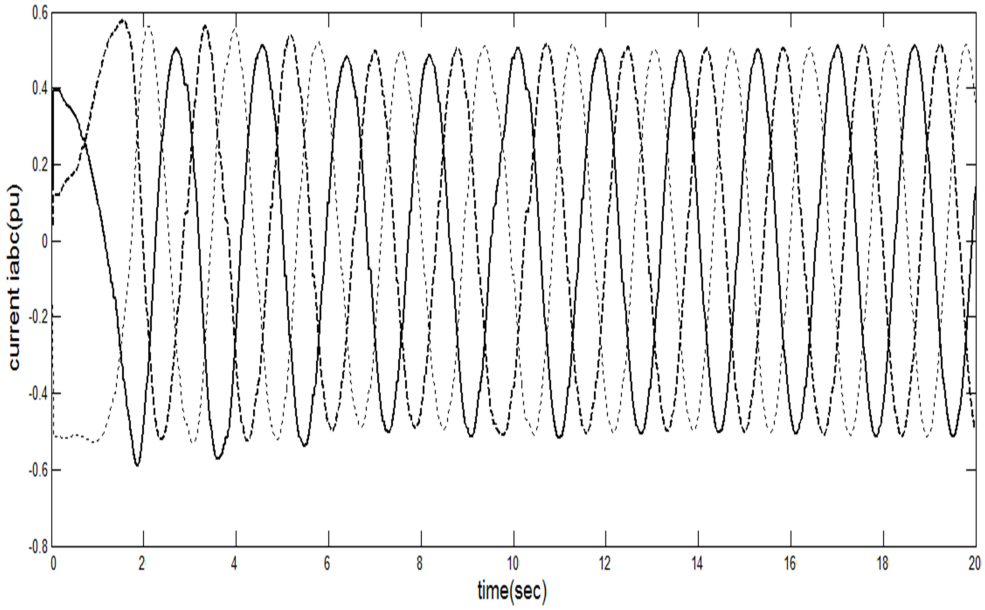

Figure 2.18: Three phase current at stator terminals i_{abc}
(A) versus time(sec)

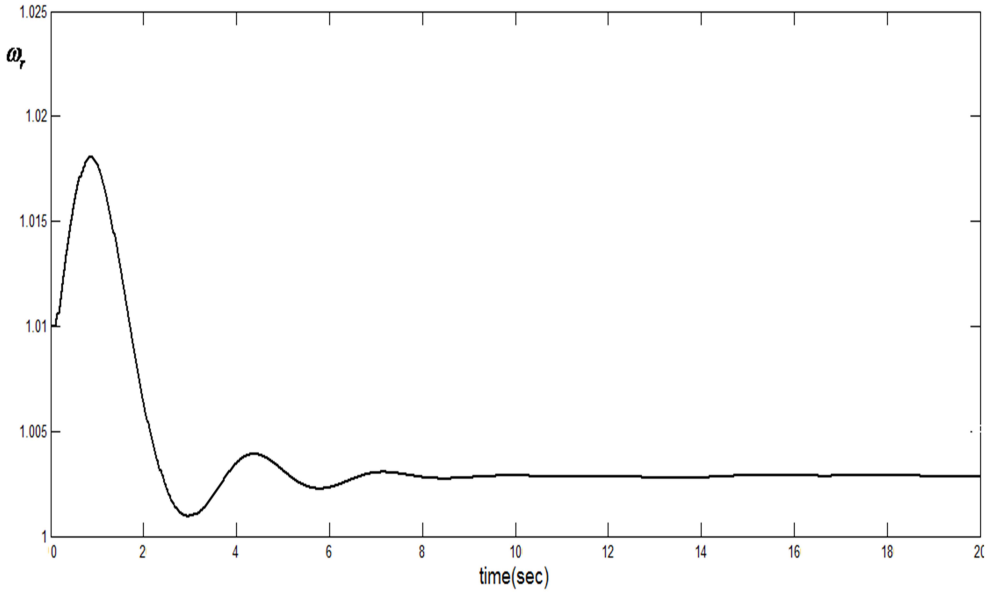

Figure 2.19: Rotor speed of DFIG(rad/sec) versus time

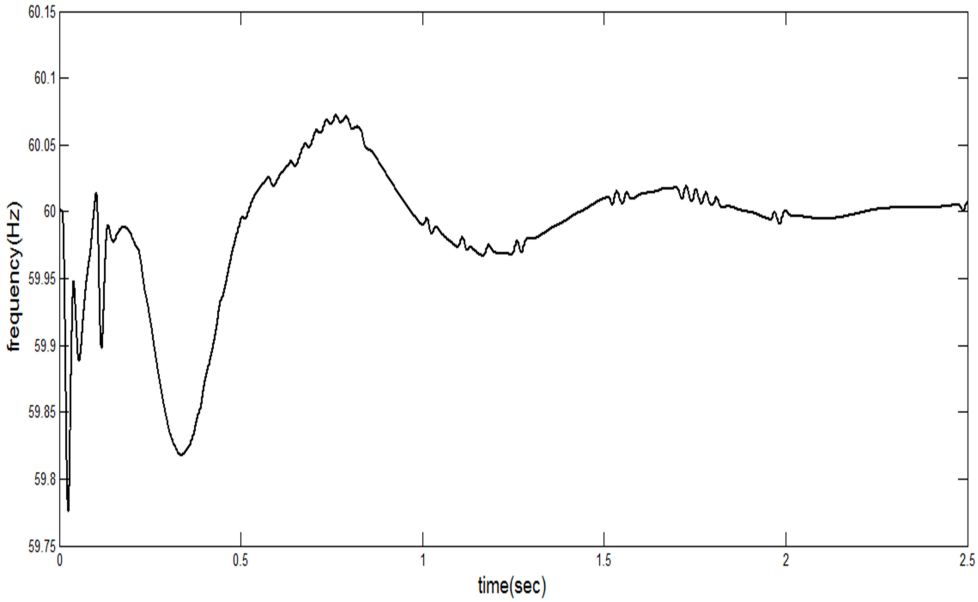

Figure 2.20: Frequency at the stator terminals versus time

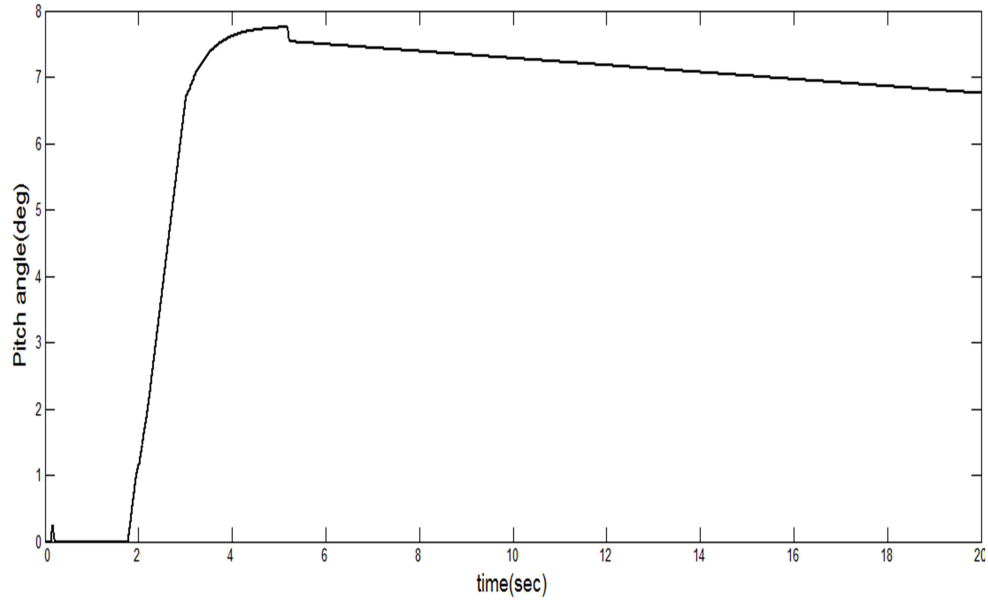

Figure 2.21: Pitch angle(deg) versus time

Comparison of performances of different controllers

Various parameters has been plotted i.e. pitch angle, active power, DFIG rotor speed versus time. In our controller, the rated wind speed is 12m/s. The mean wind speed increases from 8m/s to 13m/s as in Fig. 2.22 and then it keeps over the rated value with the wind turbulence and in our simulation the turbulence intensity is 8 percent. In Fig. 2.23 the pitch rate is limited to 8deg/s. In the region above rated speed of wind turbine, the pitch control operates to regulate the DFIG inlet power. From the simulation results, it turns out that the proposed SMC controller can successfully regulate the DFIG input power. In Fig. 2.23, time taken for varying the pitch angle is less compared to LPV and PI, to obtain the normal speed of wind turbine for better Power regulation.

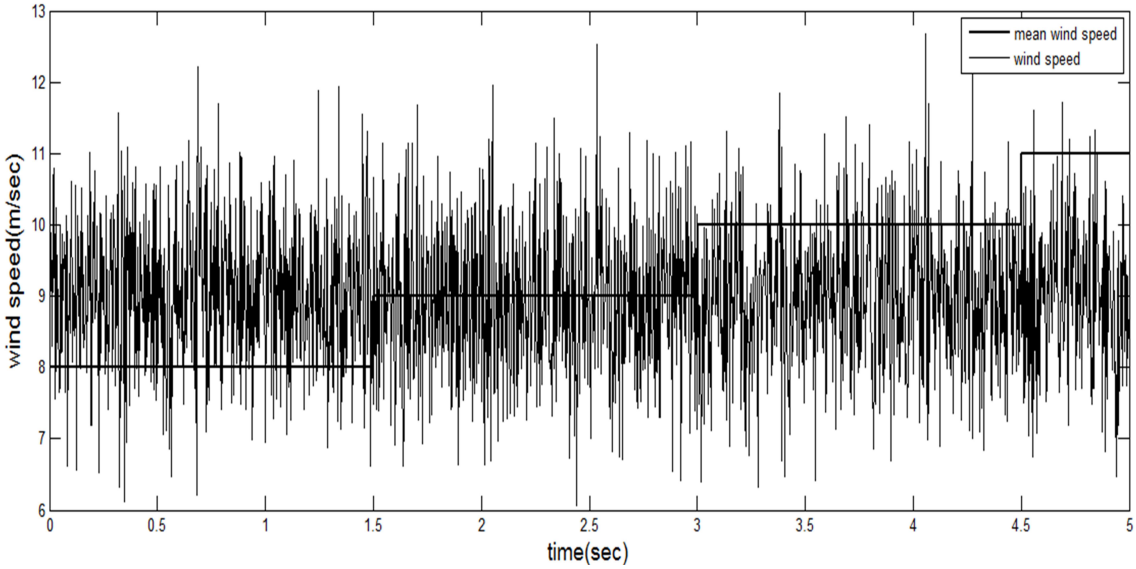

Figure 2.22: Wind profile versus time

In Fig. 2.24, Fig. 2.25 the active power and reactive power variations have been observed. Active power has attained maximum value using SMC when compared to LPV and PI. In Fig. 2.26, the generator rotor speed in pu has been better regulated compared to LPV and PI. From Fig. 2.26, the generating power is determined by the rotor speed ω_r. when the wind speed is above the rated speed, the power is better regulated and this is done by sliding mode Pitch controller. For regulating the power, the Pitch angle β is regulated so that P_g converges to its rated value.

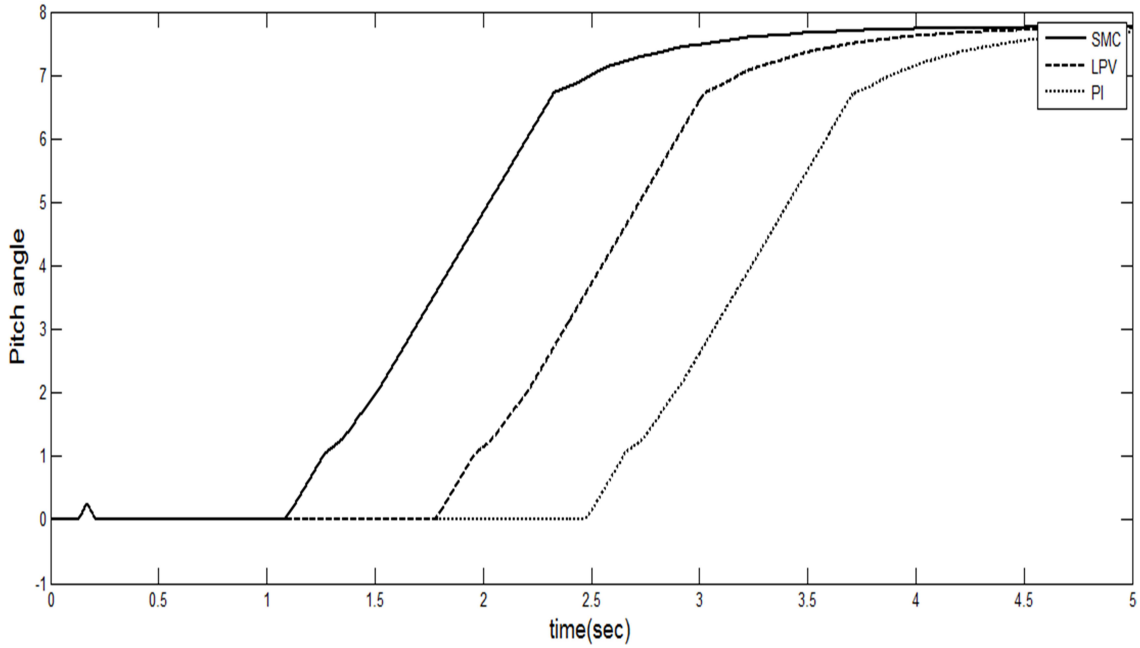

Figure 2.23: Pitch angle β versus time

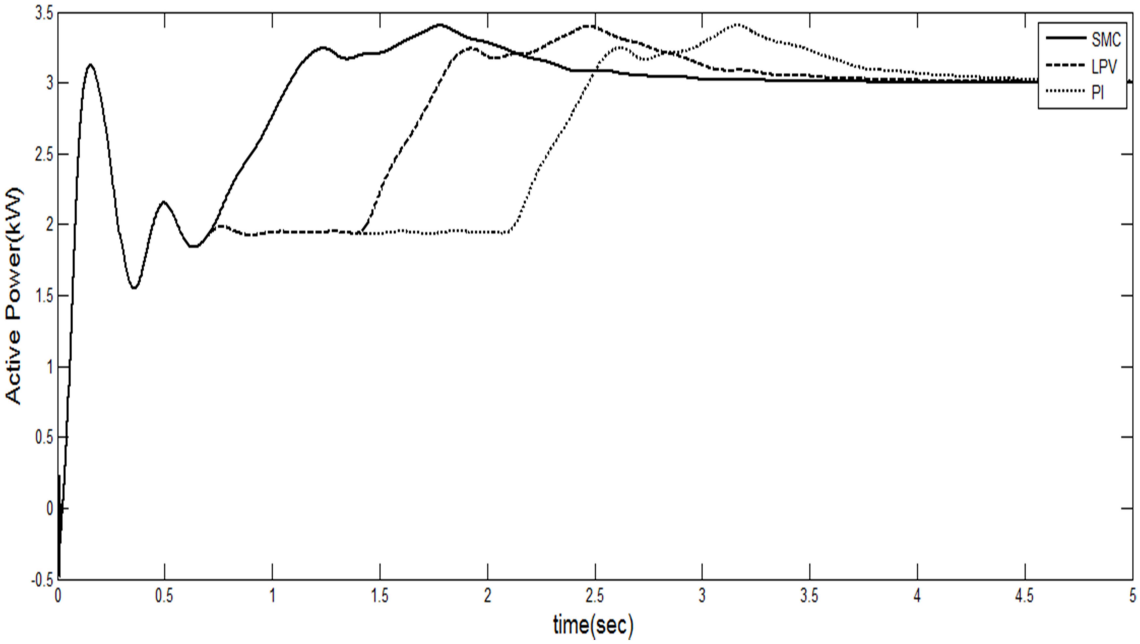

Figure 2.24: Generated Power P(kW) versus time

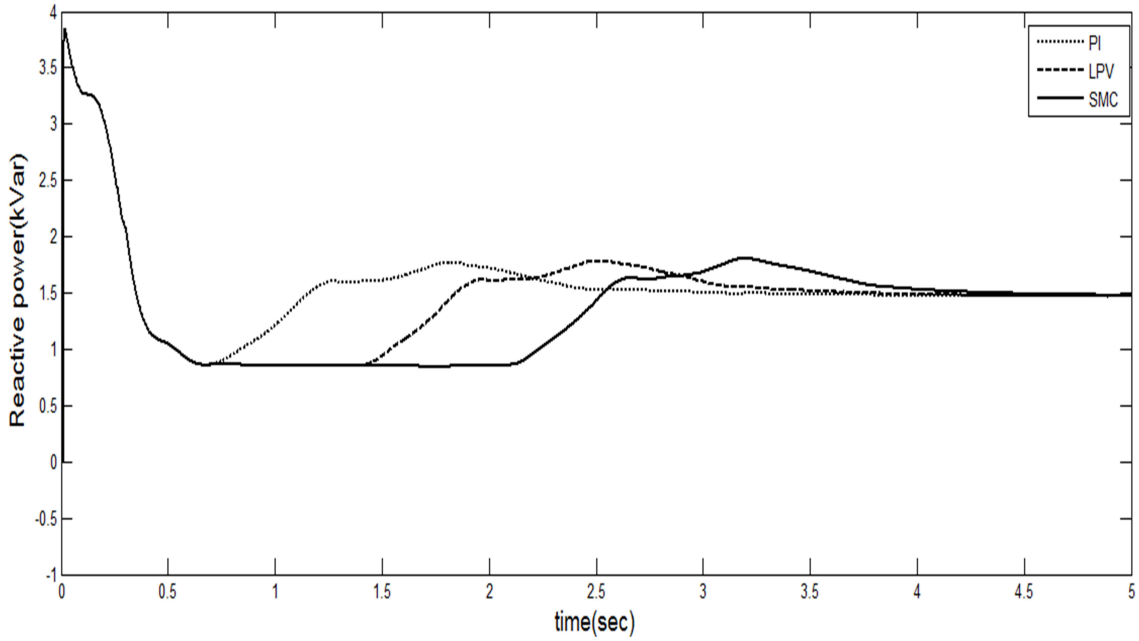

Figure 2.25: Reactive Power Q versus time

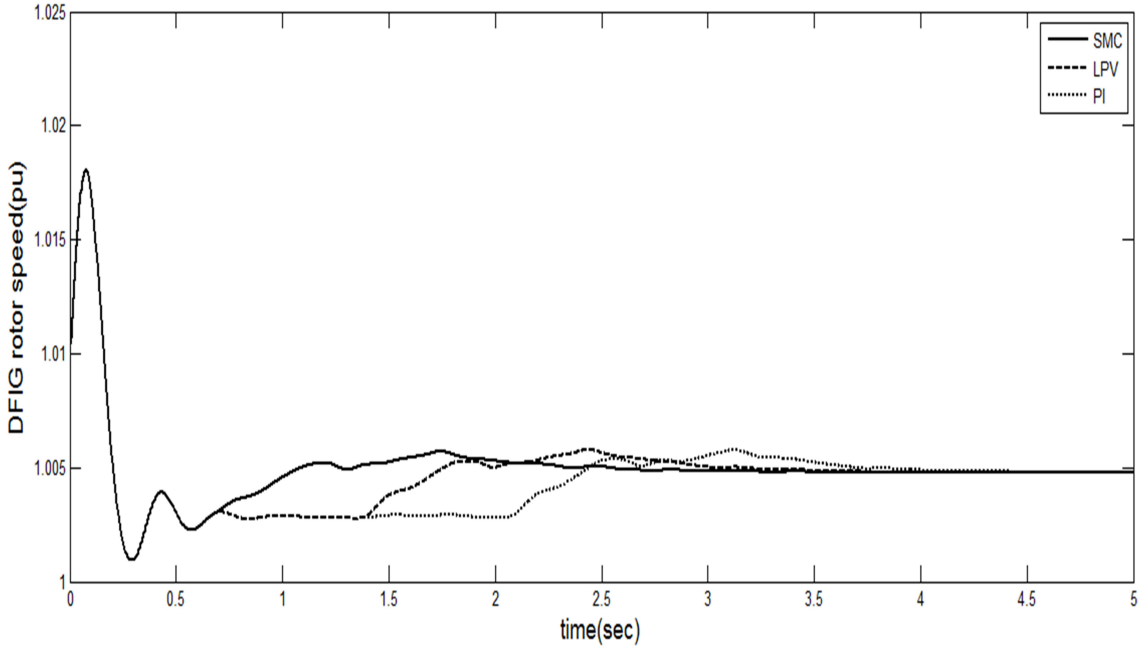

Figure 2.26: generator rotor Speed ω_r versus time

2.5 Chapter Summary

In this chapter, a sliding mode control scheme has been proposed for the DFIG wind energy system. A torque controller and a pitch controller are designed employing the sliding mode control scheme. In order to verify the proposed control strategy, simulations have been done in MATLAB/SIMULINK as well as in FPGA environment. Simulation results obtained from MATLAB and results from FPGA show that control objectives are well achieved in spite of the wind turbulence. Subsequently the performances of the SMC have been compared with that of the LPV and PI controllers. From the obtained results(both simulation and FPGA) it is observed that the sliding mode controller output exhibits superior pitch and torque control performance compared to the LPV and PI controllers.

Chapter 3

NARMAX model based Adaptive Torque and Pitch Control schemes for Wind Energy Conversion System

3.1 Introduction

In chapter 2, a SMC is designed to achieve robustness together with a chattering free response both in torque and pitch control of the WECS. Since wind speed is varying intermittently, wind energy conversion system (WECS) is a stochastic system. Therefore in this chapter, identification technique is developed for WECS system. Nonlinear Autoregressive Moving Average with exogenous input (NARMAX) model is developed to represent the dynamics of WECS which is used for real time implementation. In a doubly fed induction generator (DFIG) WECS, speed and power are the outputs for regulation which are achieved by controlling the torque and pitch angle repetitively. NARMAX model identifies the structure and significant terms of speed and power of DFIG WECS and its parameters are estimated employing an on-line adaptive Recursive Least squares (RLS) algorithm. For optimisation of torque and pitch angle, performance Index is defined in Nonlinear Adaptive Model Pre-

dictive controller (NAMPC) to achieve the control objective i.e torque and pitch angle. The weights in performance index are updated until the optimized values in control inputs (torque and pitch control) is achieved. Boundedness of the WECS is defined by considering the constraints on the outputs and control inputs. Extensive simulations are carried out with NARMAX structure with NAMPC on DFIG WECS using MATLAB/SIMULINK and the performance is compared with conventional PI controller and model predictive controller. From the obtained results, it is observed that the NARMAX model with NAMPC has minimum deviations from the operating point in power, speed, torque and pitch angle compared to other controllers.

Velocity of wind continuously varies with time, therefore adaptive control is necessary for regulating power and speed of the DFIG simultaneously. Since speed and power terms of DFIG contain a large set of unpredictable terms, selection of significant terms is important for controlling the torque and pitch angle and reducing the complexity of the WECS. As the load demand increases, large WECS with variable speed variable pitch controlled wind turbine generator systems has been paid attention to a large extent. Increase in size of wind turbines inevitably causes fluctuations in both aerodynamic power and drive train dynamics.
In the past two decades, different non adaptive controllers such as sliding mode control, linear parameter time varying control, H_∞ control, model predictive control for torque and pitch control have been proposed. Sliding mode control uses the estimated aerodynamic torque of DFIG based WECS for extracting and regulating maximum power by reducing the mechanical stress on the drive train dynamics [70, 71, 73]. In [48], coordination control for disturbances in electrical and mechanical parts of wind turbine have been proposed by using FAST (fatigue, aerodynamics, structures and turbulence code). In [10], robust pitch controller with inverse system controller and robust compensator have been proposed to withstand large disturbances and fatigue of the pitch actuators. In [62], a linear parameter varying (LPV) controller has been proposed by considering quadratic torque speed law in partial load region and LPV pitch controller in full load region. In [63, 13], H_∞ control design based on linear matrix inequality (LMI) has been proposed for both torque and pitch control through minimisation of H_∞ norm. In [54], a self tuning regulator for pitch control

in wind turbine has been designed by imposing the limits on pitch angle and identification is done with fuzzy reasoning for unpredictable wind changes. In [57], second order cone programming (SOCP) has been proposed for power and speed regulation simultaneously by controlling pitch angle and generator torque in the whole operating region (both partial and full load region) as depicted in Fig. 3.1.

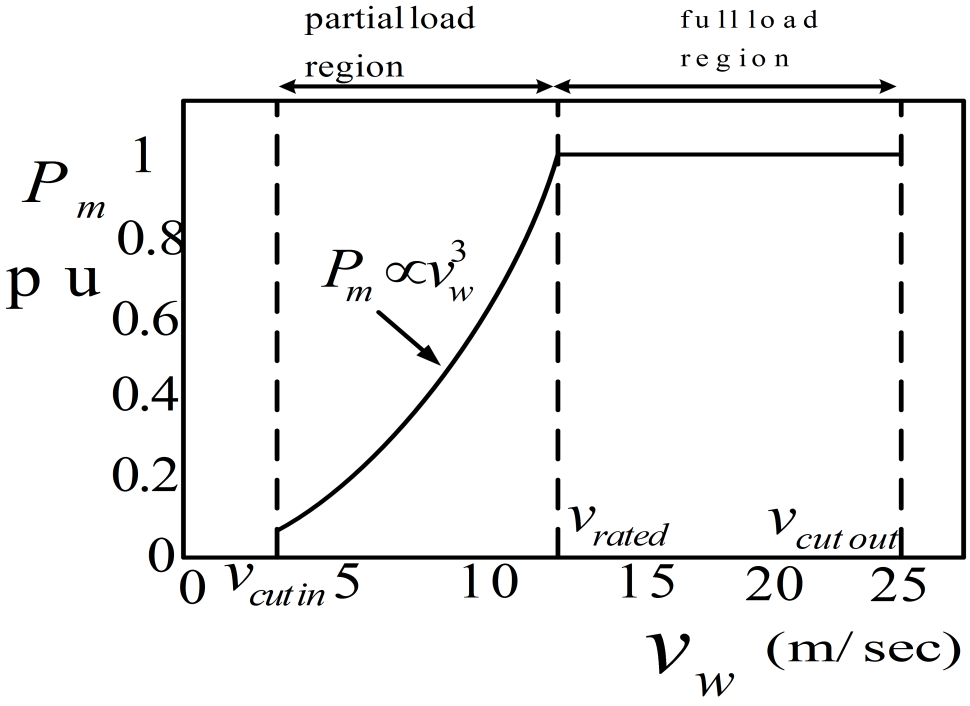

Figure 3.1: Ideal power curve (mechanical power P_m Versus wind velocity v_w) for DFIG WECS

3.2 Problem statement

Two drawbacks are associated with the above controllers. First drawback is non adaptive in nature which leads to deviations in the regulator power and speed regulation. Second drawback is, WECS is a nonlinear system which consists a large number of nonlinear terms. Selection of significant terms and estimation of parameters from this large set of generator speed terms and output power terms is important. In this chapter, the above two problems are solved by selecting an NARMAX model structure and Identifying its parameters by

using adaptive RLS technique. Gram Schmidt recursive orthogonal decomposition method and error reduction ratio (ERR) method are used for selecting the significant terms for a large set of non linear terms.

3.2.1 Chapter Objectives

- To regulate the generator speed and output power of DFIG WECS adaptively by designing torque and pitch angle controllers with minimum deviations. The objective has been achieved by using NARMAX model.
- Just as parameter estimation, the NARMAX model identifies both the structure and the parameters of an unknown non linear system.
- After system identification, selecting the significant model terms using ERR plays a vital role. Thereafter estimating the system parameters using On-line adaptive RLS and finally optimization is done by selecting the performance index to achieve the control objective.

3.3 Physical model of DFIG based WECS

Fig. 3.1 shows the two regions in which WECS has to be operated. Region 1 is the partial load region (non linear region) between cut in speed $v_{cut\,in}$ and the rated speed v_{rated} . This region is the non-linear region, where maximum power extraction can be achieved by controlling the generator speed (ω_G). Region 2 is the full load region that lies between the rated speed v_{rated} and cut-out speed v_{cutout}. In this region, output power (P_G) regulation and generator (turbine) speed regulation are obtained by controlling the generator torque (Γ_G) and pitch angle (β) of wind turbine. In this chapter, regulation of generator power and speed of the DFIG WECS has been developed with adaptive RLS for WECS. Since speed and power depend on controlling the torque and pitch angle, NARMAX structure is used for selecting and determining the significant terms of generator power and speed from large set of terms reducing the complexity in controlling the torque and pitch angle.

WECS comprises mainly of aerodynamic subsystem, pitch actuator subsystem, drive train subsystem, and DFIG with power electronic converters connected to grid as shown in Fig. 3.2.

Wind turbine converts the kinetic energy of wind into mechanical energy which is fed to the DFIG for converting into electrical energy. Drive train dynamics plays a vital role for torque and pitch control of WECS shown in Fig. 3.2.

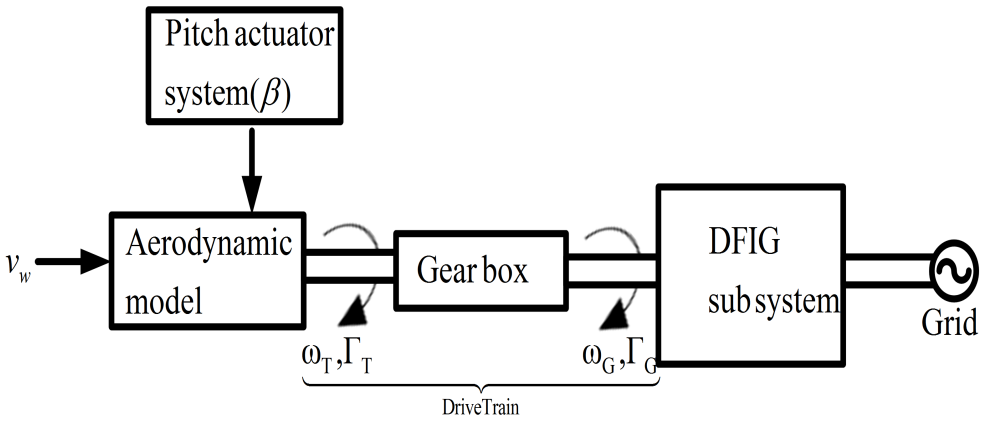

Figure 3.2: Schematic diagram of a WECS

3.4 State space model of DFIG WECS

The discrete time state space model [53, 55] of DFIG WECS is represented as

$$\begin{aligned} x(k+1) &= Ax(k) + Bu(k) + B_v w \\ y(k) &= Cx(k) \end{aligned} \tag{3.1}$$

$$x(k) \in \ R^5,\ x(k)=[\Delta\omega_T\ \Delta\omega_{\mathrm{G}}\ \Delta\Gamma_D\ \Delta\beta\ \Delta v_w]^T \tag{3.2}$$

$$u(k) \in R^2,\ u(k) = [\Delta\Gamma_{Gcmd}\ \Delta\beta_{cmd}]^T \tag{3.3}$$

$$y(k) \in R^2,\ y(k) = [\Delta\omega_G(k)\ \Delta P_G(k)]^T \tag{3.4}$$

where $x(k)$ is the state vector, $u(k)$ is the control input vector, $y(k)$ is the output vector obtained from the states and inputs through matrix C , w is the disturbance input vector, A is the system matrix which affect the state dynamics, B is the gain distribution matrix and B_v is the disturbance input matrix. The state vectors in $x(k)$ are $\Delta\omega_T$, $\Delta\omega_{\mathrm{G}}$, $\Delta\Gamma_D$, $\Delta\beta, \Delta v_w$. These state vectors are calculated from the dynamics of drive train system [70, 71, 73] given

by

$$\begin{aligned} J_T\frac{d\omega_T}{dt} &= \Gamma_T - \Gamma_D \\ J_G\frac{d\omega_G}{dt} &= \Gamma_D - \Gamma_G \\ \Gamma_D &= K_S\left(\theta_T - \theta_G\right) + B_S\left(\frac{d\theta_T}{dt} - \frac{d\theta_G}{dt}\right) \end{aligned} \tag{3.5}$$

where Γ_T is the aerodynamic torque, Γ_G is the generator torque, Γ_D is the drive train tortional torque, ω_G is the electrical angular speed, K_S is the shaft compliance index, B_S is the damping coefficient, $\theta_T,\ \theta_G$ are the angular positions of the shaft at the turbine rotor and generator side. Aerodynamic torque of wind turbine is given by

$$\Gamma_T = \frac{P_m}{\omega_T} = \frac{\rho\Lambda {v_w}^3 C_P(\lambda,\beta)}{2\omega_T} \tag{3.6}$$

where P_m is the mechanical power obtained from the wind turbine , β is turbine blade pitch angle, $\Lambda = \pi R^2$, C_P is power coefficient, ω_T is turbine rotational speed, ρ is the air density in g/m^3, Λ is the cross sectional area of the turbine, v_w is the wind velocity and R is the radius of turbine shaft, λ, β tip speed ratio and pitch angle. Since wind speed v_w is a function of order three, the expression Γ_T[63] has nonlinearity, linearising (3.6) and rewriting as

$$\Gamma_T = f(\omega_T,\ v_w,\ \beta) \tag{3.7}$$

$$\Gamma_{T,OP} = f(\omega_{T,OP},\ v_{w,OP},\ \beta_{OP}) \tag{3.8}$$

Eq(3.7)is expanded by using Taylor series at the operating point as

$$\begin{aligned} \Delta\Gamma_T = \Gamma_T - \Gamma_{T,OP} &= \frac{\partial\Gamma_T}{\partial\omega}\Delta\omega_T + \frac{\partial\Gamma_T}{\partial v}\Delta v_w + \frac{\partial\Gamma_T}{\partial\beta}\Delta\beta \\ \therefore\ \Delta\Gamma_T &= \gamma\Delta\omega_T + \zeta\Delta v_w + \xi\Delta\beta \end{aligned} \tag{3.9}$$

Taking partial derivative of (3.6), yields

$$\begin{aligned}\gamma &= \frac{\partial \Gamma_T}{\partial \omega} = \frac{\rho \Lambda {v_w}^2}{2\omega_T}\left(-C_P\frac{v_w}{\omega_T} + R\frac{\partial C_P}{\partial \lambda}\right)\\ \zeta &= \frac{\partial \Gamma_T}{\partial v} = \frac{\rho \Lambda v_w}{2}\left(3C_P\frac{v_w}{\omega_T} + R\frac{\partial C_P}{\partial \lambda}\right)\\ \xi &= \frac{\partial \Gamma_T}{\partial \beta} = \frac{\rho \Lambda {v_w}^3}{2\omega_T}R\frac{\partial C_P}{\partial \beta}\end{aligned} \tag{3.10}$$

where $\Delta\omega_T = \omega_T - \omega_{T,OP}$, $\Delta v_w = v_w - v_{w,OP}$, $\Delta\beta = \beta - \beta_{OP}$ and Δ is the small signal value(deviation) around (OP). From (3.5), the state vectors are derived as follows

$$\Delta\dot{\omega}_T = \frac{1}{J_T}\left[\gamma\Delta\omega_T + 0 - \Delta\Gamma_D + \xi\Delta\beta + \zeta\Delta v_w\right] \tag{3.11}$$

$$\begin{aligned}\Delta\dot{\omega}_G &= \frac{1}{J_G}\left[\Delta\Gamma_D - \Delta\Gamma_G\right]\\ \Rightarrow \Delta\dot{\omega}_G &= \frac{1}{J_G}\left[0 - \Gamma_G + \Gamma_D + 0 + 0\right]\end{aligned} \tag{3.12}$$

$$\Delta\dot{\Gamma}_D = \left(B_S\frac{1}{J_T}\gamma + K_S\right)\Delta\omega_T - K_S\Delta\omega_G - \left(\frac{B_S}{J_T} - \frac{B_S}{J_G}\right)\Delta\Gamma_D + \frac{B_S}{J_T}\xi\Delta\beta + \frac{B_S}{J_T}\zeta\Delta v_w + \frac{B_S}{J_G}\Delta\Gamma_{G,cmd} \tag{3.13}$$

Pitch system is highly non-linear which is subjected to pitch rate constraints for β and $\dot{\beta}$ given by $\beta_{\min} \le \beta \le \beta_{\max}$, $\dot{\beta}_{\min} \le \dot{\beta} \le \dot{\beta}_{\max}$

$$\begin{aligned}\dot{\beta} &= \frac{1}{T_\beta}\left(\beta_{cmd} - \beta\right)\\ \Delta\dot{\beta} &= \frac{1}{T_\beta}\left(\Delta\beta_{cmd} - \Delta\beta\right)\end{aligned} \tag{3.14}$$

where $\dot{\beta}$ is the derivative of pitch angle, β_{cmd} is the pitch control signal, T_β is the hydraulic lag. Stochastic wind speed in [53] is represented as

$$\dot{v}_t = -\frac{1}{T_v}v_t(k) + m_v(k) \tag{3.15}$$

where $m_v(k) = d(k)$, $d(k)$ is the disturbance, $v_t(k)$ is the rapidly varying turbulence component, $m_v(k)$ is the Gaussian white noise, T_v is the time constant. From (3.11)-(3.15), the following matrices are obtained as

$$[A] = \begin{bmatrix} & \frac{\gamma}{J_T} & 0 & -\frac{1}{J_T} & \frac{\xi}{J_T} & \frac{\varsigma}{J_T} \\ 0 & & 0 & \frac{1}{J_G} & 0 & 0 \\ K_s + \frac{B_s\gamma}{J_T} & & -K_s & -(\frac{B_s}{J_T} - \frac{B_s}{J_G}) & \frac{B_s\xi}{J_T} & \frac{B_s\zeta}{J_T} \\ 0 & & 0 & 0 & -\frac{1}{T_\beta} & 0 \\ 0 & & 0 & 0 & 0 & -\frac{1}{T_v} \end{bmatrix},$$

$$[B] = \begin{bmatrix} 0 & 0 \\ -\frac{1}{J_G} & 0 \\ \frac{B_s}{J_G} & 0 \\ 0 & \frac{1}{T_\beta} \\ 0 & 0 \end{bmatrix}, \; [B_v] = \begin{bmatrix} 0 \\ 0 \\ 0 \\ 0 \\ 1 \end{bmatrix}, [C] = \begin{bmatrix} 0 \\ 1 \\ 0 \\ 0 \\ 0 \end{bmatrix}^T$$

3.5 NARMAX model Structure Representation of DFIG WECS

3.5.1 Structure representation

The discrete time representation of (3.1) using (3.2)-(3.4)in nonlinear form [74, 75, 76, 77] can be expressed as

$$y_i(k) = F_i \begin{bmatrix} y_1(k-1), y_1(k-2), ..., y_1(k-N_y), \\ y_n(k-1), y_n(k-2), ..., y_n(k-N_y), \\ u_1(k-1), u_2(k-2), ..., u_1(k-N_u), \\ u_n(k-1), u_n(k-2), ..., u_n(k-N_u), \\ \xi_1(k-1), \xi_1(k-2), ..., \xi_1(k-N_\xi), \\ \xi_n(k-1), \xi_n(k-2), ..., \xi_n(k-N_\xi) \end{bmatrix} \quad (3.16)$$
$$i = 1, 2..., n$$

where $y_i(k)$ is the autoregressive (AR) variable or system output, $u_i(k)$ is an exogenous (X) variable or system input, $\xi_i(k)$ is the moving average (MA) variable or white noise. N_y , N_u and N_ξ represent the order (or maximum delay) in the output, input and moving average variable respectively. $F_i[\cdot]$ represents the multi input multi output(MIMO) non linear map which contains both the process parameters and noise parameters associated with the model

of the WECS. $F_i^p[\cdot]$ is the i^{th} process model which do not contain noise terms and $F_i^p[\cdot]$ is the i^{th} process model which contain noise terms. The structure of the proposed NARMAX model for the DFIG based WECS is shown in Fig. 3.3.

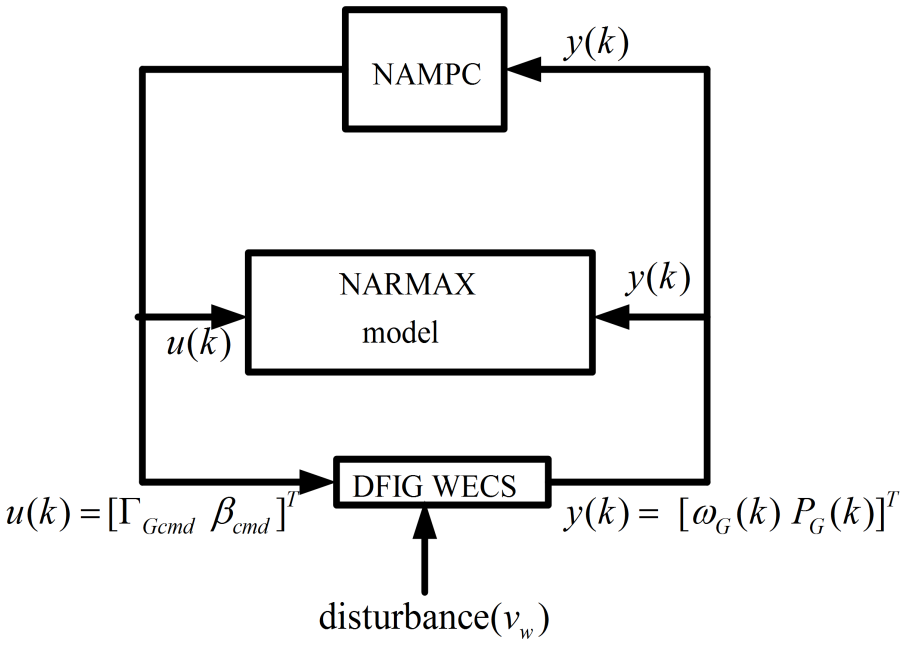

Figure 3.3: Structure of the Multivariable Self Tuning Regulator for DFIG WECS

3.5.2 Extended Polynomial NARMAX Model of DFIG WECS

NARMAX model can be applied to DFIG WECS as

$$y_i(k) = F_i^n \begin{bmatrix} -\omega_{Gi}(k-1), -\omega_{Gi}(k-2), ..., -\omega_{Gi}(k-N_{\omega_G}), \\ -P_{Gi}(k-1), -P_{Gi}(k-2), ..., -P_{Gi}(k-N_{P_G}) \\ \Gamma_{Gi}(k-1), \Gamma_{Gi}(k-2), ..., \Gamma_{Gi}(k-N_{\Gamma_G}), \\ \beta_i(k-1), \beta_i(k-2), ..., \beta_i(k-N_\beta) \\ \xi_i(k-1), \xi_i(k-2), ..., \xi_i(k-N_\xi) \end{bmatrix} \tag{3.17}$$

where $\omega_{Gi}(k), P_{Gi}(k)$ are the outputs with N_{ω_G} and N_{P_G} as maximum delays. $\Gamma_{Gi}(k)$ and $\beta_i(k)$ are the control inputs with N_{Γ_G} , N_β as maximum delays and $\xi_i(k)$ is the driving force of the wind which is considered as white noise from the noise generator of order N_ξ.

The linear difference equation of the ARMAX $(N_{\omega_G}, N_{P_G}, N_{\Gamma_G}, N_\beta, N_\xi)$ model obtained from (3.17) is represented by

$$y(k) = \sum_{i=1}^{N_{\omega_G}} -a_i\omega_{Gi}(k-i) + \sum_{i=1}^{N_{P_G}} -a_i P_{Gi}(k-i) + \sum_{j=1}^{N_{\Gamma_G}} b_j\Gamma_{Gj}(k-j) + \sum_{j=1}^{N_{\Gamma_G}} b_j\beta_j(k-j) + \sum_{l=1}^{N_\xi} c_l\xi_l(k-l) \tag{3.18}$$

$$\begin{aligned} y(k) = & -a_1\omega_{G1}(k-1) - a_2\omega_{G2}(k-2) - .....a_{N_{\omega_G}}\omega_{GN_{\omega_G}}(k-N_{\omega_G}) \\ & - a_1P_{G1}(k-1) - a_2P_{G2}(k-2) - .....a_{N_{P_G}}P_{GN_{\omega_G}}(k-N_{P_G}) \\ & + b_1\Gamma_{G1}(k-1) + b_2\Gamma_{G2}(k-2) + ...b_{N_{\Gamma_G}}\Gamma_{GN_{\Gamma_G}}(k-N_{\Gamma_G}) \\ & + b_1\beta_1(k-1) + b_2\beta_2(k-2) + ...b_{N\beta}\beta(k-N_\beta) \\ & + c_1\xi_1(k-1) + c_2\xi_2(k-2) + ... + c_{N_\xi}\xi_{N_\xi}(k-N_\xi) + \xi(k) \end{aligned} \tag{3.19}$$

The above equation in WECS is linear in parameters, considering a linear regression model for (3.19) as

$$y(k) = \sum_{i=1}^{n} \varphi_i(k)\theta_i(k) + \xi(k) \quad k = 1, 2...., N \tag{3.20}$$

where $y(k)$ is the output or dependent variable to be regressed (speed and power of the DFIG to be controlled),

$$\theta_i(k) = \begin{bmatrix} a_1, a_2, ..., a_{N_{\omega_G}}, a_{N_{P_G}}, b_1, b_2, ..., b_{N_{\Gamma_G}}, b_{N_\beta} \\ c_1, c_2, ..., c_{N_\xi} \end{bmatrix}^T$$

is the unknown parameter model to be estimated,

$$\varphi_i(k) = \begin{bmatrix} -\omega_{Gi}(k-1), -\omega_{Gi}(k-2), ..., -\omega_{Gi}(k-N_{\omega_G}), \\ -P_{Gi}(k-1), -P_{Gi}(k-2), ..., -P_{Gi}(k-N_{P_G}), \\ \Gamma_{Gi}(k-1), \Gamma_{Gi}(k-2), ..., \Gamma_{Gi}(k-N_{\Gamma_G}), \\ \beta_i(k-1), \beta_i(k-2), ..., \beta_i(k-N_\beta) \end{bmatrix}^T$$

is the regression matrix and $\xi = \xi_i(k-1), \xi_i(k-2), ..., \xi_i(k-N_\xi)$ is the modelling error. Eq(3.20) can be rewritten as

$$y = \varphi\Theta + \Xi \tag{3.21}$$

where $y = [\omega_{\mathrm{G}}(1), \omega_G(2), ..., \omega_G(N), P_G(1), P_G(2), ..., P_G(N)]^T$,
$\varphi = \left[\varphi^T(1), \varphi^T(2), ...\varphi^T(N)\right]^T$,
$\Theta = [\theta_1, \theta_2, ...\theta_n]^T$,
$\Xi = [\xi(1), \xi(2)....., \xi(N)]^T$,
$\varphi^T(k) = [\varphi_1(k), \varphi_2(k), ...\varphi_n(k)]\,; \qquad k = 1, 2..., N$

3.5.3 Orthogonal Least squares QR decomposition of the regression matrix

The advantage of orthogonal transformation is that it preserves the Euclidian norm of a vector. Orthogonal transformation is numerically stable when applied on inaccurate vector or matrix which results that error will not increase. QR Decomposition is applied on linear regression matrix φ having the length N proposed by Gram Schmidt.
Let $\varphi^T\varphi$ be a symmetric positive definite matrix, then it can be decomposed as

$$\varphi^T\varphi = R^T D R = R^T \left(Q^T Q\right) R \tag{3.22}$$

$$\varphi = QR \tag{3.23}$$

where $R = \begin{bmatrix} 1 & x_{12} & x_{13} .... & x_{1n} \\ & 1 & x_{23} .... & x_{2n} \\ & & \ddots \quad \ddots & \\ & & \ddots \quad \ddots & \\ & & 1 \quad x_{n-1n} & \\ & & & 1 \end{bmatrix}$ is an $n \times n$ upper triangular matrix and

$Q = \begin{bmatrix} q_1(1).....q_n(1) \\ \vdots \qquad \vdots \\ \vdots \qquad \vdots \\ q_1(N).....q_n(N) \end{bmatrix} = [q_1\, q_2.....q_n]$ is an $N \times n$ orthogonal matrix with orthogonal columns which satisfies $Q^TQ = \left(\varphi R^{-1}\right)^T \left(\varphi R^{-1}\right) = D = diag\left[\sum_{k=1}^{N} q_1^2(k), ..., \sum_{k=1}^{N} q_n^2(k)\right]$ where D has positive diagonal entries given by $D = diag\left\{d_1\, d_2 .....d_n\right\}$ with $d_i = \langle q_i, q_i \rangle$

where $\langle\cdot\rangle$ denotes the inner product, that is $\langle q_i, q_j\rangle = q_i^T, q_j = \sum_{t=1}^{N} q_i(t), q_j(t)$

$$Q(n) = \varphi(n)R_N^{-1}(n) \tag{3.24}$$

Eq(3.20) can be rewritten as

$$y = Qg + \Xi \tag{3.25}$$

where

$$Q = \varphi R^{-1}$$
$$g = R\Theta$$

3.5.4 Normalizing the columns of Q

Classical Gram Schmidt (CGS) normalises the columns of Q , by taking one column at a time and orthogonalizing φ . The process is repeated by augmenting the resultant matrix with $(N - n)$ further orthonormal columns of Q which covers the full set of orthonormal vectors for N dimensional Eucledian space. A decomposition equivalent to (3.20) can be obtained as

$$\varphi = \bar{Q}\begin{bmatrix} R_1 \\ 0 \end{bmatrix} \tag{3.26}$$

where R_1 is an $n \times n$ upper triangular matrix with positive diagonal elements and $\bar{Q} = [\bar{q}_1, ..., \bar{q}_N]$ is an $N \times N$ orthogonal matrix, i.e.

$$\langle \bar{q}_i, \bar{q}_j \rangle = 1 \qquad i = j$$
$$0 \qquad i \neq j$$

The estimated value of g can be found by

$$\hat{g}_i = \frac{\langle q_i, y\rangle}{\langle q_i, q_i\rangle} \; i = 1, 2, ..., n \tag{3.27}$$

where $g = [g_1, g_2, ...g_n]^T$

3.5.5 Structure determination (sub set selection)

From (3.25), sum of the squares of output is

$$\langle y, y \rangle = \sum_{i=1}^{n} g_i^2 \langle q_i, q_i \rangle + \langle \xi, \xi \rangle \tag{3.28}$$

For model structure selection, error reduction ratio (ERR) is defined as proportion of the output variance in terms of q_i as

$$[err]_i = \frac{g_i^2 \langle q_i, q_i \rangle}{\langle y_i, y_i \rangle} \quad 1 \leq i \leq n \tag{3.29}$$

ERR can also be defined as

$$[err]_i = \frac{\left(y_i^2\right)}{\langle y_i, y_i \rangle} \quad 1 \leq i \leq n \tag{3.30}$$

Since regression matrix φ contains large number of terms, selection of subset containing significant terms plays a vital role. ERR is employed for subset selection through forward regression manner. In ERR, at each step, a term is selected and verify for largest $[err]_i$ when compared to remaining terms.

Selection of terms is terminated when the following is satisfied

$$1 - \sum_{i=1}^{n_s} [err]_i < \rho \tag{3.31}$$

where $\rho\,(0 < \rho < 1)$ is the specified tolerance, which leads to subset model of $n_s\,(n_s < n)$ terms.

Procedure for subset selection in linear regression model φ :

Initially user specifies value of ρ and full model set of n terms. At the n_s stage:

(i) Assume each term as n_s term in the selected model, compute ERR for each $n = n_s + 1$, and corresponding orthogonalization is being done.

(ii) Term which yields largest value of ERR is selected. If condition $1 - \sum_{i=1}^{n_s} [err]_i < \rho$ is satisfied, go to (iii), otherwise set $n = n_s + 1$ and go to (i).

(iii) Final subset model contains n_s terms, then parameter estimate $\hat{\Theta}_s$ is determined from

$R_s\Theta_s = g_s \, or \, \Theta_s = [\bar{y}_1, ..., \bar{y}_{n_s}]^T$ where R_s is an $n_s \times n_s$ upper triangular matrix.

(iv) The parameter estimate $\hat{\Theta}$ satisfies $g = R\Theta$ and can be estimated by backward substitution i.e

$$\begin{aligned} \hat{\theta}_n &= \hat{g}_n, \\ \hat{\theta}_i &= \hat{g}_i - \sum_{k=i+1}^{n} x_{ik}\hat{\theta}_k, \quad i = n-1, ...1 \end{aligned} \tag{3.32}$$

3.5.6 Parameter estimation

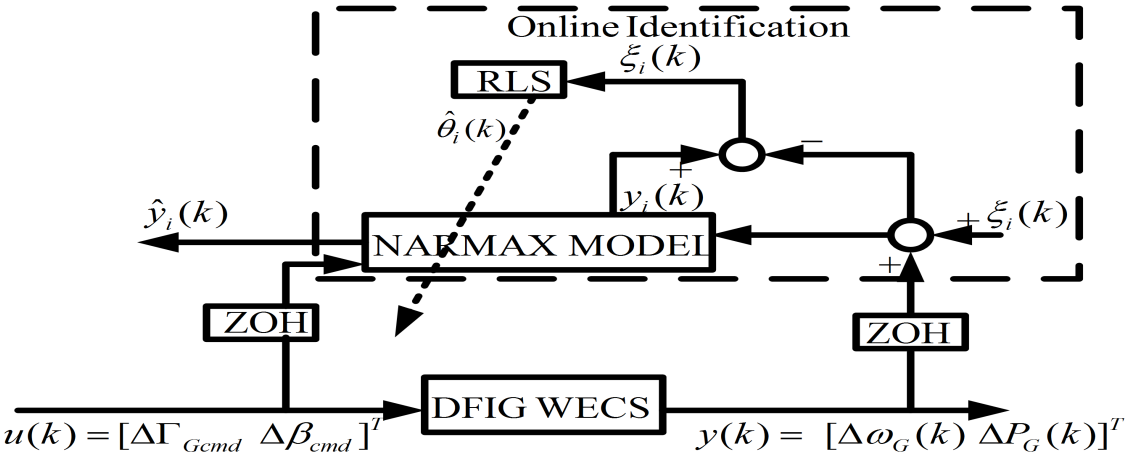

Figure 3.4: Parameter extraction using on-line Recursive structure identification

The parameter matrix $\hat{\theta}_n$ is estimated not only by backward substitution but also can be estimated on-line by using RLS algorithm [78] shown in Fig. 3.4. Within the time limit, the parameters are updated recursively based on sampling period for converging to the true system parameters. Matrix computations of RLS algorithm are summarised as follows

(i) Parameter estimate $\hat{\theta}(k)$ is calculated as

$$\hat{\theta}(k+1) = \hat{\theta}(k) + M(k)\xi(k) \tag{3.33}$$

(ii) Model prediction error is achieved based on new output data $y(k+1)$ and old estimated

parameter $\hat{\theta}(k)$ and regression vector $\varphi(k)$ as

$$\xi(k+1) = y(k+1) - \hat{\theta}(k+1)\varphi(k) \tag{3.34}$$

(iii) Error covariance matrix $P(k) = E\left\{\xi(k)\,\xi^T(k)\right\}$ is updated by

$$P(k+1) = P(k)\big[I - M(k+1)\varphi^T(k+1)\big]^{-1} \tag{3.35}$$

where $\xi(k) = y(k) - \hat{y}(k)$ is the error signal for predicting outputs $y(k)[\omega_G(k)$ and $P_G(k)]$ based on the parameter estimate $\hat{\theta}(k)$

(iv) Solve the Kalman gain $M(k)$(blending factor) for the next sample to minimize the mean square error in terms of covariance given by

$$M(k+1) = P(k+1)\varphi(k)\big[I + \varphi(k)P(k+1)\varphi^T(k)\big]^{-1} \tag{3.36}$$

3.6 Optimization of torque and pitch angle using NAMPC technique

Inner loop (Torque and Pitch controller) is derived as shown in Fig. 3.5. The optimized parameters are given to NAMPC to obtain the control inputs $u(k)$. Performance Index is defined for (3.18) to achieve the control objective as in [79]

$$PI = J(k) = \sum_{i=1}^{N_{\omega_G}} \left[z_1(\hat{\omega}_G(k+i) - \omega_G(k+i))^2\right] + \sum_{i=1}^{N_{P_G}} \left[z_2\Big(\hat{P}_G(k+i) - P_G(k+i)\Big)^2\right] + \sum_{i=1}^{N_{\Gamma_G}} \left[v_1\Big(\hat{\Gamma}_G(k+i) - w\Gamma_G(k+i)\Big)^2\right] + \sum_{i=1}^{N_{\beta}} \left[v_2\Big(\hat{\beta}(k+i) - w\beta(k+i)\Big)^2\right] \tag{3.37}$$

subjected to constraints of

$$\begin{aligned}
&\beta_{\min} \leq \beta(k+i) \leq \beta_{\max},\ i = 1, 2, ...N_\beta \\
&\dot{\beta}_{\min} \leq \dot{\beta}(k+i) \leq \dot{\beta}_{\max},\ i = 1, 2, ...N_\beta \\
&P_G(k+i) \leq P_{G\max},\ i = 1, 2....N_{P_G} \\
&\omega_G(k+i) \leq \omega_{G\max},\ i = 1, 2....N_{\omega_G}
\end{aligned} \tag{3.38}$$

where N_{P_G}, N_{ω_G} are the predefined prediction horizons and N_β is the predefined control horizon. z_1 and z_2 are the weighting matrices(observable matrices) of outputs ω_G and P_G, v_1 and v_2 are weighting matrices(controllable matrices) of control inputs Γ_G and β, w is the unit diagonal matrix.

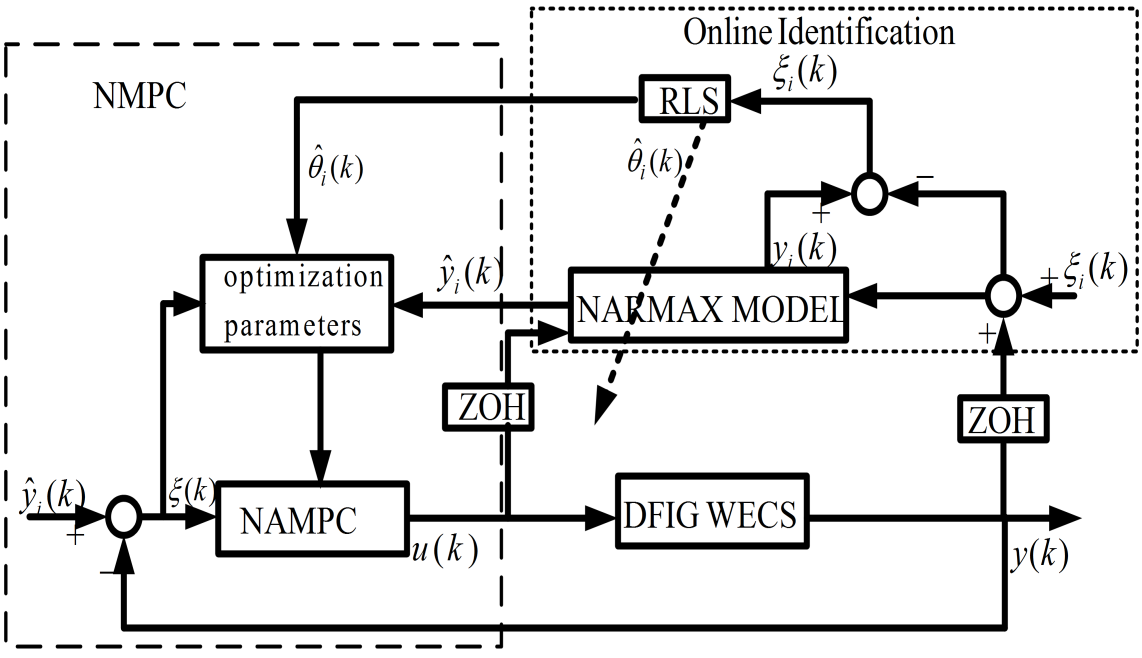

Figure 3.5: NAMPC structure with RLS NARMAX identification technique

Control input torque command $\Gamma_{Gref}(k)$ and reference pitch angle $\beta_{cmd}(k)$ are generated from control law as

$$u(k)\left[\Gamma_{Gref}(k),\beta_{cmd}(k)\right]=-\left[B_1^TZB_1+V\right]^{-1}\left[\begin{array}{c} B_1^TZ\left\{\begin{array}{c}\sum_{i=1}^{N_{\omega G}}-a_i\omega_{Gi}(k-i+1)+\\ \sum_{i=1}^{N_{PG}}-a_iP_{Gi}(k-i+1)\end{array}\right\} \\ +\left\{\begin{array}{c}\sum_{i=1}^{N_{\Gamma G}}b_i\Gamma_{Gi}(k-i+1)-Vw\Gamma_{Gi}(k-1)+\\ \sum_{i=1}^{N_{\beta}}b_i\beta_i(k-i+1)-Vw\beta_i(k-1)\end{array}\right\}\end{array}\right]. \tag{3.39}$$

The parameter matrices a_i, b_j in $\hat{\theta}_n$ for $i,j=1,2...n$ are estimated on-line with RLS algorithm and then the control law is proposed. For saving identification time B_1 is taken as unit matrix.

The control law is defined after parameter estimation of $\hat{\theta}_n$. For deriving the control law, performance index has to be minimised by taking partial derivative of J with respect to control inputs Γ_G and β as $\frac{\partial J}{\partial \Gamma_G}$ and $\frac{\partial J}{\partial \beta}$ setting it to zero. The observable matrix $Z=[z_1\ z_2]^T$ defines the identical input output equivalent subsystem of the original system for all initial states as

$$Z=\left[\begin{array}{c} CA\ CA^2\ CA^3\ .....CA^{N_{\omega G}} \\ CA\ CA^2\ CA^3\ .....CA^{N_{PG}}\end{array}\right] \tag{3.40}$$

3.7 Results and Discussion

Performance of the DFIG WECS using NARMAX structure with recursive NAMPC has been verified with extensive simulations carried using MATLAB/SIMULINK. Using tool boxes such as Linear matrix inequality (LMI), Model Predictive control (MPC), control system, Power system and system identification. Parameters used for simulation study are given in Table 3.1.

As wind is not a constant parameter, for statistical analysis, simulation studies are pursued by randomly generating the data for wind speed using a Gaussian noise generator. Fig. 3.6 shows the instantaneous wind speed and the mean wind speed varying in-between 8 to 8.5 m/sec. From (3.37), for minimising the cost function, the weights (z_1,z_2,v_1,v_2) have been relatively adjusted with respect to other weights. For example for minimising the

Table 3.1: Simulation Parameters for DFIG WECS ([57, 55])

Wind Turbine and Rotor	
Number of blades	3
Cut in speed v_{cutin}	3 m/sec
Cut out speed v_{cutout}	25 m/sec
Rated speed v_{rated}	12 m/sec
Air density ρ	1.25 Kg/m^3
Optimum tip speed ratio λ	8
Power coefficient C_p	0.49
Rated rotor speed ω_T	22rpm
Maximum rotor speed	23rpm
Blade radius	40m
Drive Train	
Gear ratio	250:3
Turbine inertia J_T	$90 \times 10^6 kgm^2$
Low speed shaft tortional stiffness K_s	$160 \times 10^6 Nm/rad$
Low speed shaft tortional stiffness B_s	$10 \times 10^6 Nm/rad$
DFIG	
Rated power P_g	$2kW$
Maximum Generator speed	1500rpm
Generator inertia J_G	60 kgm^2
Generator torque Γ_T	$13.4KNm$
Pitch actuator	
Time constant	0.1sec
Minimum/maximum pitch angle $\beta_{\min}/\beta_{\max}$	$0^o/90^o$
Minimum/maximum pitch rate$\dot{\beta}_{\min}/\dot{\beta}_{\max}$	$-10^o/10^o per\ sec$
Number of poles	4
Supply frequency	50Hz

fluctuations in wind speed, the weight z_1 has to be increased with respect to z_2 and vice versa. Similarly, if the pitch angle has to be kept in a tolerable limit, the control weight v_2 has to be increased with respect to v_1 and vise versa. The weight updates is presented in Fig. 3.7-Fig. 3.10. It is observed that the results obtained are in close approximation with [55].

Fig. 3.7, 3.8, 3.9, 3.10 show response of parameters $(\omega_G, P_G, \Gamma_G, \beta)$ for Gaussian noise disturbance in wind speed from 8 to 8.5 m/sec. For validation of the proposed NARMAX method, comparison has been done with three different controllers (i.e MPC without NAR-

MAX structure, PI and NAMPC with NARMAX structure). The results are analysed for variations in both outputs (ω_G, P_G) and control inputs (Γ_G, β).

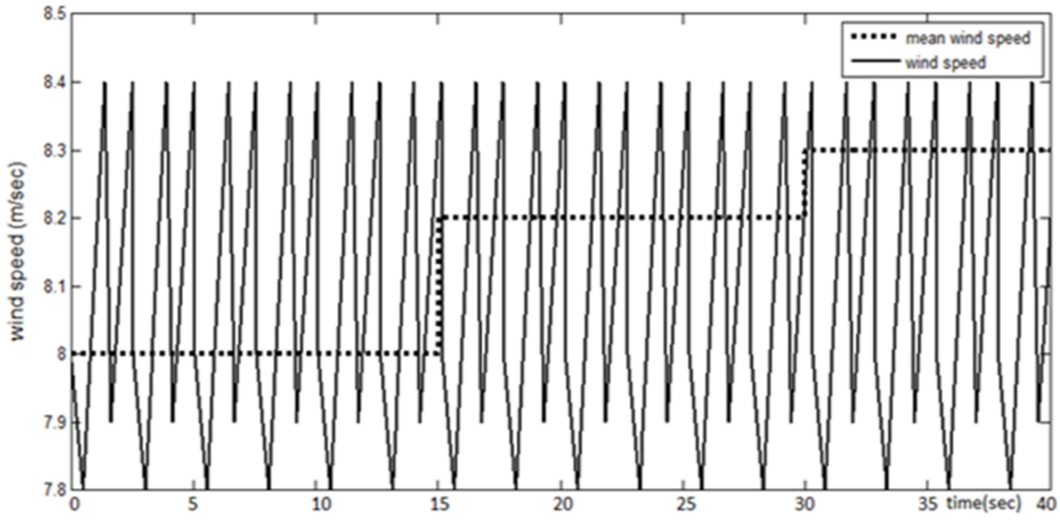

Figure 3.6: Wind speed profile in partial load region for Gaussian noise disturbance(actual wind speed and mean wind speed)

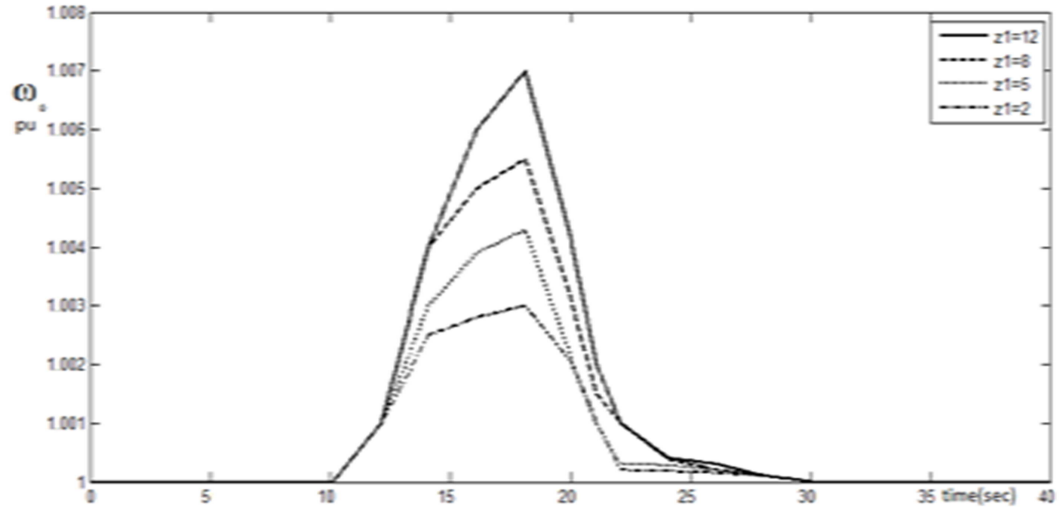

Figure 3.7: Response of Generator speed ω_G for different values of weight z_1

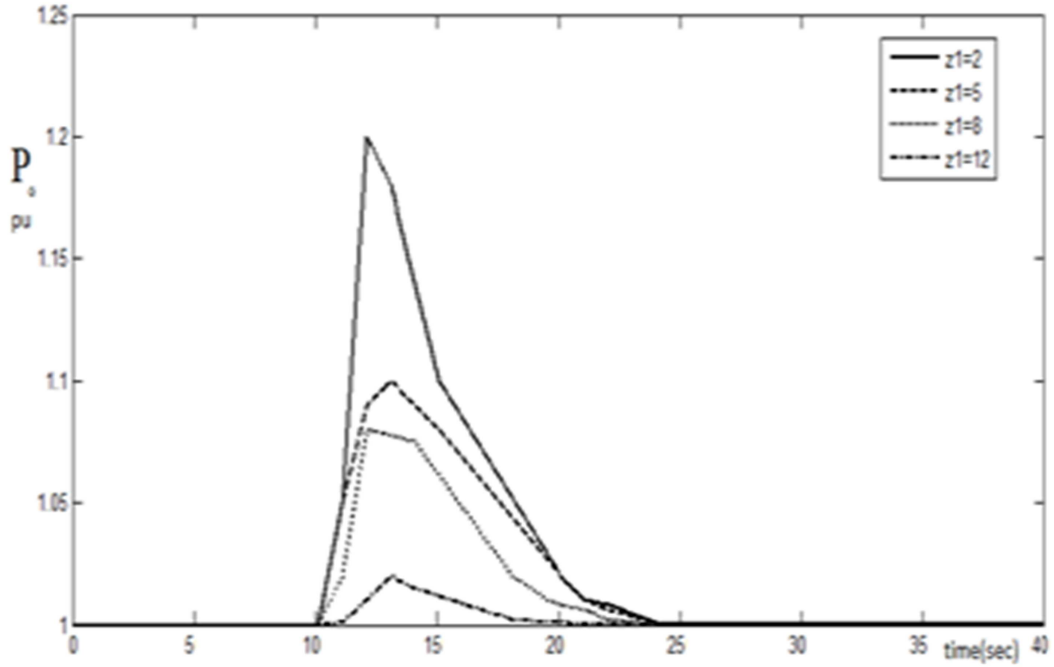

Figure 3.8: Response of Output Power P_G for different values of weight z_1

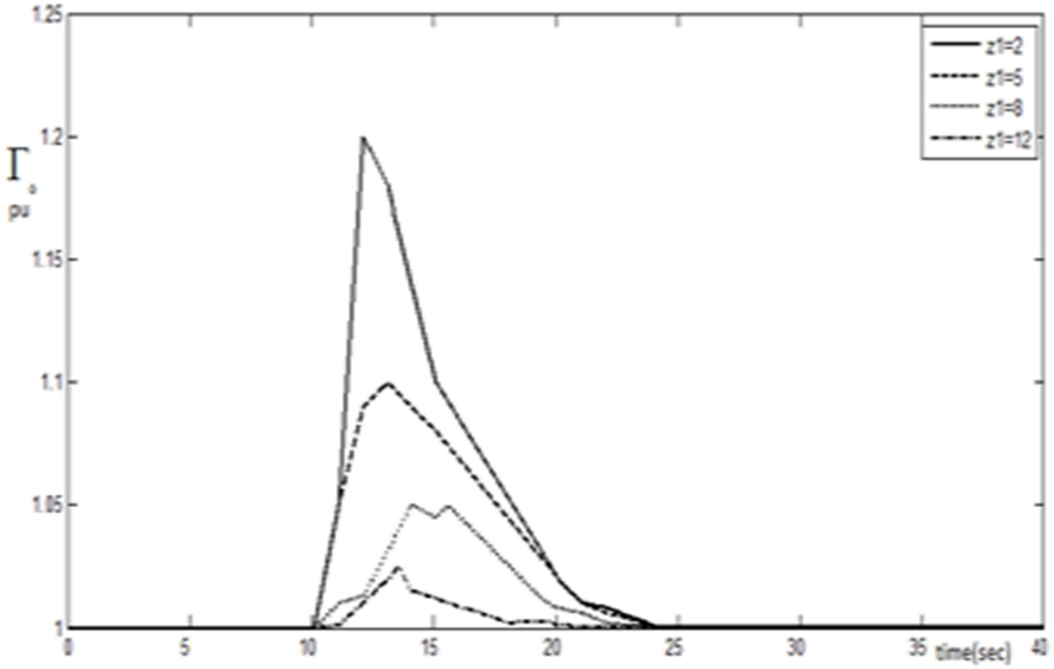

Figure 3.9: Response of control input Γ_G for different values of control weight z_1

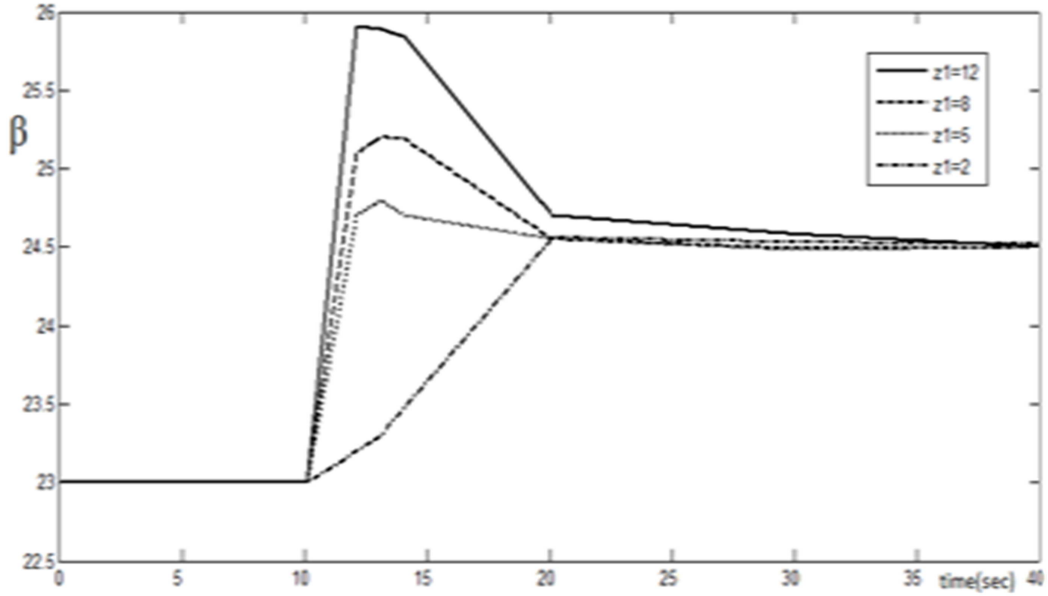

Figure 3.10: Response of control input β for different values of control weight z_1

Performance comparison of controllers

From Fig. 3.11, the deviations in generator speed is large in PI controller, but minimised to some extent using MPC controller and the deviations are drastically reduced approximating to 1 pu, by using NAMPC with NARMAX. The tortional fluctuations in drive train have also been reduced avoiding the damage to the wind turbine.

In Fig. 3.12, output power has been levelled around 1 pu by appropriate sub set selection using NARMAX as explained in section 3.4. In Fig. 3.13, by updating the control weights recursively using the RLS algorithm and the optimal parameters for $\hat{\theta}(k)$ are obtained to obtain the optimal control law as described in section 3.5 for torque command generation.

From Fig. 3.13 it is seen that there are the minimum torque pulsations in NAMPC as compared to PI and MPC controllers. In Fig. 3.14, by considering the constraints in (3.38), the parameter matrix b_j in $\hat{\theta}_n$ for $i, j = 1, 2...n$ are estimated on-line with RLS algorithm for avoiding the damage to the turbine blades. Since the on-line estimation has been used in NARMAX structure, pitching of the blades has been updated according to the instantaneous values instead of mean value which results in poor stability for PI and MPC.

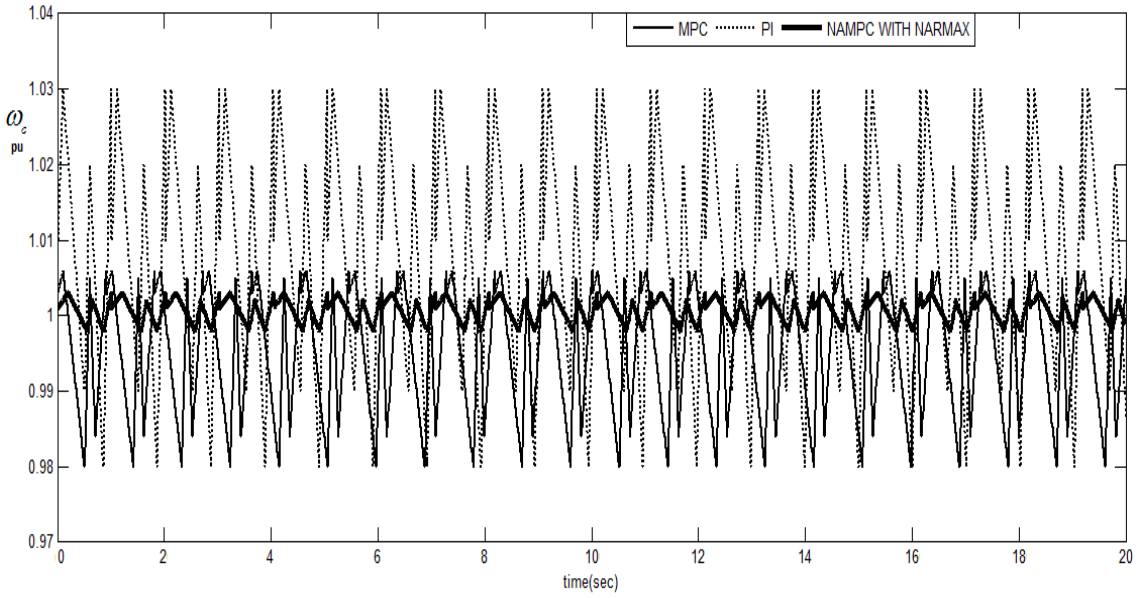

Figure 3.11: Performance comparison of PI, MPC and NAMPC with NARMAX structure identification for regulated speed ω_G

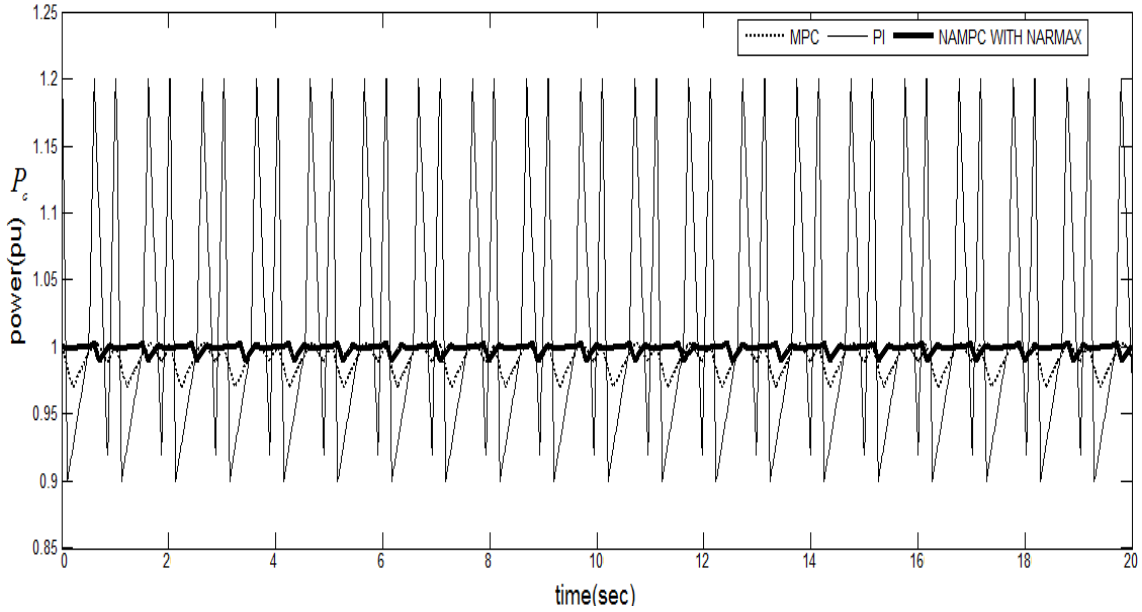

Figure 3.12: Performance comparison of PI, MPC and NAMPC with NARMAX structure identification for generated power P_G

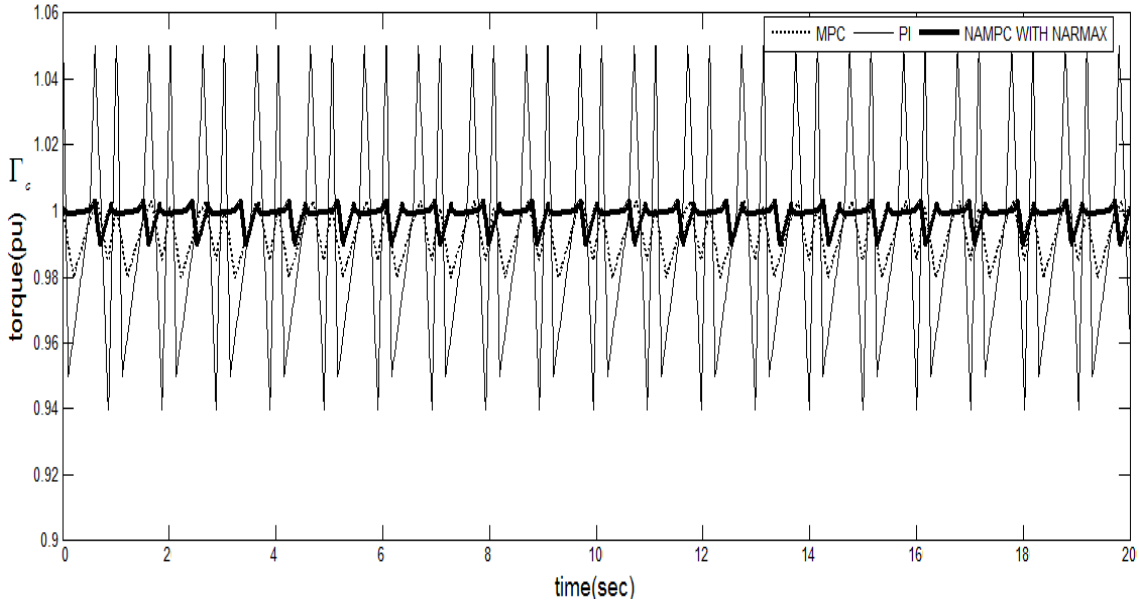

Figure 3.13: Performance comparison of PI, MPC and NAMPC with NARMAX structure identification for torque control input Γ_G

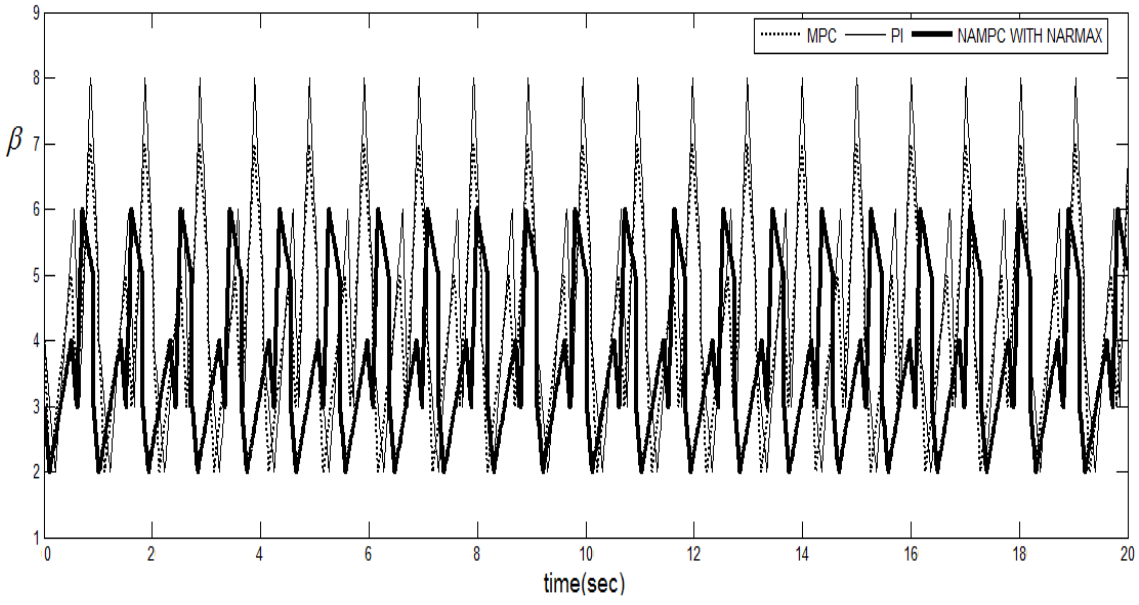

Figure 3.14: Performance comparison of PI, MPC and NAMPC with NARMAX structure identification for pitch angle β

Table 3.2: Comparison of computational burden for PI, MPC and NAMPC with NARMAX structure identification controllers

Parameter	Computatioal time (sec)
PI	5.2 sec
MPC	5.5 sec
NAMPC	5.7 sec

The computational time for three different controllers namely PI, MPC, NAMPC with NARMAX model structure of the wind turbine are provided in Table 3.2. From the comparison of computational times, it is observed that although the proposed NAMPC takes slightly more time i.e 5.7 sec but its performance is superior amongst the three controllers in terms of minimum torque pulsations and excellent speed and power regulations.

3.8 Chapter Summary

In this chapter, performance of the NARMAX structure on DFIG variable speed variable pitch WECS is verified by comparing power and speed performances with the conventional PI and model predictive controllers in both partial and full load regions. DFIG parameter deviations are minimised to a large extent in outputs (output power and generator speed regulation) and control inputs (torque and pitch angle) in DFIG WECS. Simulation results confirmed that proposed NARMAX adaptive NAMPC technique exhibits excellent performance around the operating point. In above rated speed region, generator power loss has been reduced with the proposed method. Subset selection in the NARMAX structure has reduced the computational time drastically instead of considering all the terms in the structure. The parameter coefficients are estimated by using an adaptive RLS algorithm and are updated on on-line according to the instantaneous changes in outputs and operated at the operating point for running the WECS system very efficiently when compared to the non adaptive techniques.

Chapter 4

Active and Reactive Power Control of DFIG Wind Energy Conversion System with Optimal Preview Stator Voltage Oriented Control

4.1 Introduction

In chapter 3, focus was on regulation speed and power of DFIG connected to wind turbine using torque and pitch control. In previous chapters power converters and grid were not considered. So, in this chapter, both electrical and mechanical subsystems are considered for active and reactive power control of DFIG WECS. WECS DFIG is connected with two voltage source converters connected back to back, one in rotor side and the other on grid side connected directly to stator side. Field current and torque of the DFIG are controlled by Rotor Side Converter (RSC) while reactive power of the grid and DC link voltage is controlled by the Grid Side Converter (GSC). In [7], field oriented control (FOC) is considered for stability analysis of a DFIG by orienting d axis of the stator flux in synchronous reference frame. Since stator flux cannot be measured directly, a flux estimator is required. In flux oriented control, flux dynamics has not been eliminated which causes cross coupling of induced

emfs in rotor current dynamics resulting in transients of DFIG. In [20], the rotor dynamics are considered without any compensation for induced emfs due to rotor flux linkages which possess serious concern for achieving stable operation. This causes overshoot in the active and reactive power response, which do not react instantaneously leading to fluctuations on terminal voltage profile. In [80], state space model analysis has been presented for studying power system dynamics by observing eigen values and participation factors for stability analysis of DFIG. But the DFIG system becomes unstable without any closed loop control for large values of external grid reactance. In [81], model predictive direct power control has been proposed but the harmonic content in gid voltage is high according to grid codes. In [82], SMC-FOC is proposed for controlling active power and minimisation of copper loss but due to switching function and chattering effect in sliding mode, the harmonic content is more. In [72], sliding mode control has been proposed both on RSC and GSC. on GSC, active power generation and reactive power is compensated, but due to selection of many control variables, frequency distortions and ripples may occur. In [46], analysis of wind farm has been made by considering a 6th order dynamic model of DFIG. The nonlinear model is linearized by state space analysis and the dynamic simulations are performed by eigen value analysis. But the state parameters have not been optimised for model oscillations related to sub synchronous resonance. In [49], rotor currents has been regulated for active and reactive power generation. In [83], sliding mode control has been used for direct active and reactive power regulation. In view of the above short comings in this paper, SVOC using LQR is proposed. In the proposed controller, instead of flux, stator voltage is oriented with d axis, since stator voltage is directly measured; there is no necessity of estimator. Since the d-q components for voltages and currents are controlled independently by rotor side converters in SVOC, the complexity is also less in SVOC. Feedforward compensation is also considered for compensating the transients occurred due to disturbance signal.

In this chapter, a state feedback controller for a Double Fed Induction Generator (DFIG) based wind energy conversion system (WECS) has been proposed with stator voltage oriented control (SVOC).This state feedback controller uses the concept of Linear Quadratic Regulator (LQR) with preview control. Preview control is applied for disturbance suppression and tracking in discrete domain for various applications. Stator active and reactive

power are controlled by using quadrature and direct axes currents respectively. Inner rotor current loop of the DFIG is controlled using LQR optimal preview control (OPC) with SVOC technique. In the inner rotor current loop, a feedforward compensation is used together with a proportional Integral control for compensating cross coupling induced emfs and stator flux induced emf. The OPC uses a performance index in which the weighing factors are used in view of achieving fast current control dynamics. The weighing factors in performance index are made large for minimising the augmented error in current dynamics of DFIG to yield zero steady state error. A PWM switching for the voltage source converters has been designed with outputs of DFIG rotor current control loop dynamics.

4.1.1 Chapter Objectives

- To control stator active and reactive power by rotor quadrature current and direct axis current respectively, by developing an LQR-OPC for the inner rotor current control of the DFIG with SVOC.
- To minimise the disturbances due to flux dynamics and eliminating cross coupling induced emf and emf induced due to stator flux.
- For achieving the above objective, performance index is considered with large weighing factors for minimising the augmented error by which the actual rotor currents coincides with the reference rotor currents to reach to steady state quickly.

4.2 Proposed structure of WECS

Fig.4.1 shows the schematic diagram of Wind Simulator based power generation of DFIG for grid connected system. Wind turbine and gear box are replaced with a DC shunt motor as emulator for generating the wind turbine speed. A DC shunt motor is coupled with the rotor of a DFIG for operating the DFIG both in sub and supersynchronous speeds. A LQR OPC is designed for the DFIG by linearising the DFIG dynamic equations as follows. Firstly state equations of the DFIG are derived, after that, performance index is defined involving the state equation of DFIG, then Ricatti equations are solved to obtain steady state optimal solutions.

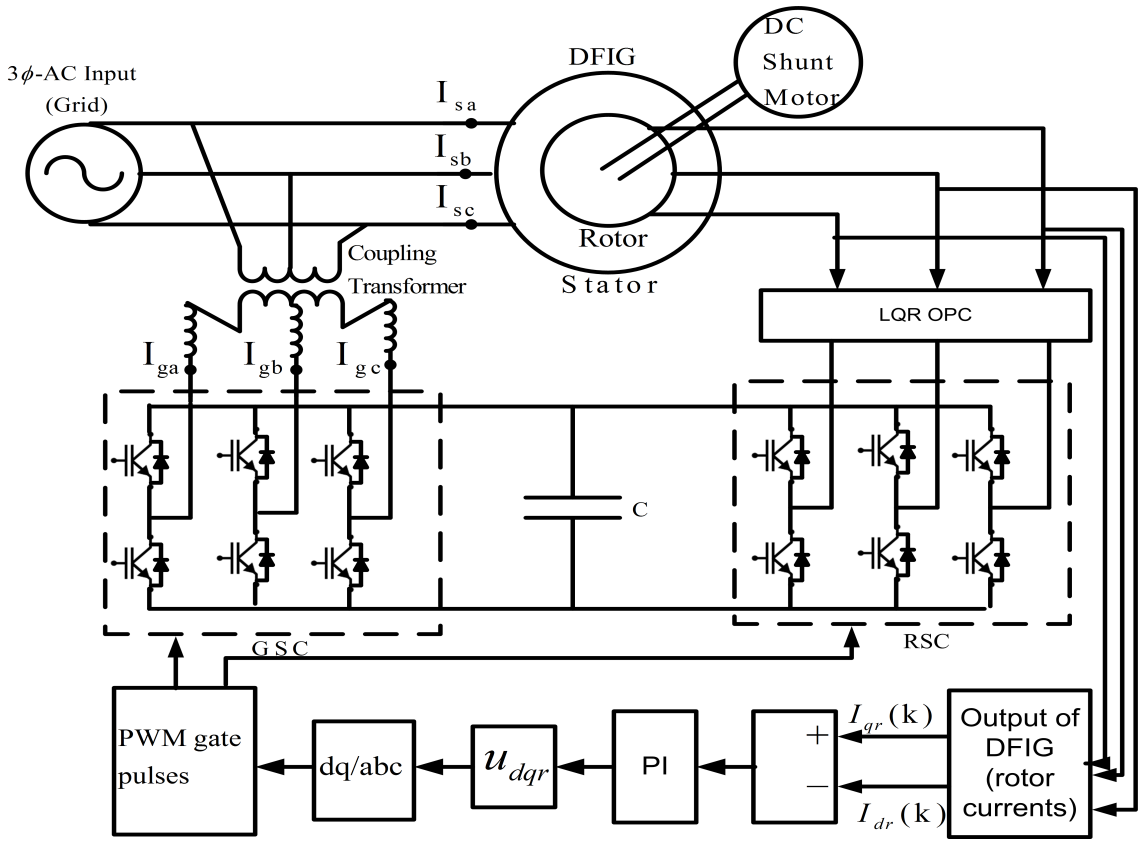

Figure 4.1: Schematic diagram of DFIG based WECS

Finally full state optimal feedback controller is obtained by multiplying the Kalman gain with state variables to achieve the full state feedback controller.

Fig.4.2 shows the space vector representation of DFIG with SVOC. The stator d axis rotates at ω_s and rotor rotates at ω_r . Stator voltage vector $\bar{u}_s$ is aligned with the d axis in which $u_{qs} = 0$, $u_{ds} = u_s$. In Fig.4.2, θ_s denotes stator voltage vector angle, θ_r denotes rotor position angle with respect to stator frame, and θ_{sl} is the slip angle between $\bar{u}_s$ and rotor. In DFIG, the grid is connected to the stator and the power converter system(RSC and GSC) is connected to the rotor of the DFIG which is used to adjust the rotor speed. In Fig.4.3, model of the DFIG is represented by two sets of equations in namely voltage and flux equations. These are presented below

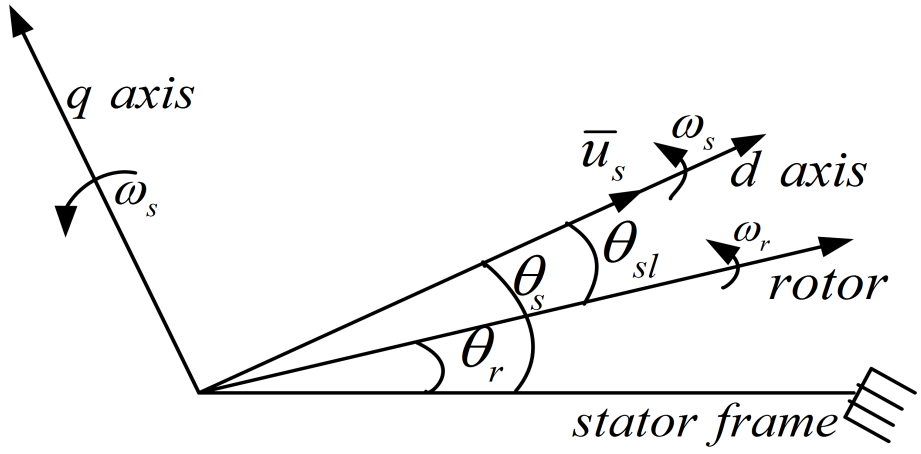

Figure 4.2: Space Vector representation of DFIG

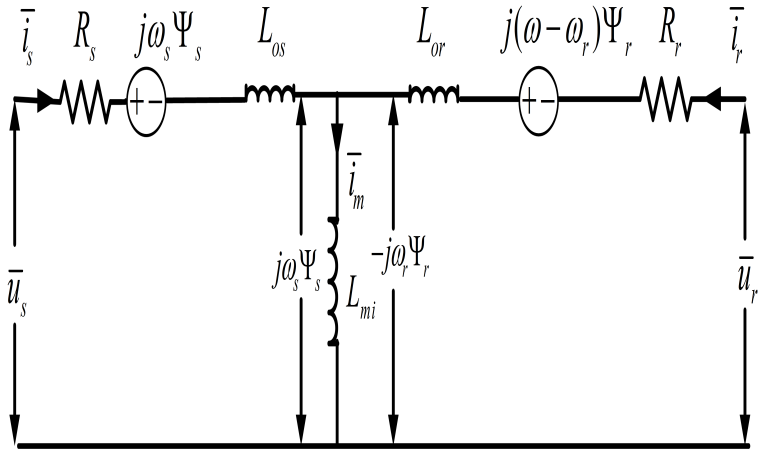

Figure 4.3: Equivalent circuit of DFIG

From Fig.4.3, voltage equations are given by

$$\begin{aligned} u_{ds} &= R_s I_{ds} + j\omega\psi_{ds} + \omega_s\psi_{qs} \\ u_{qs} &= R_s I_{qs} + j\omega\psi_{qs} + \omega_s\psi_{ds} \\ u_{dr} &= R_r I_{dr} + j\omega\psi_{dr} + (\omega_s - \omega_r)\psi_{qr} \\ u_{qr} &= R_r I_{qr} + j\omega\psi_{qr} + (\omega_s - \omega_r)\psi_{dr} \end{aligned} \tag{4.1}$$

Flux linkage equations are given by

$$\begin{aligned}
\psi_{ds} &= (L_{os} + L_{mi})\ I_{ds} + L_{mi}\ I_{dr} = L_{ss}\ I_{ds} + L_{mi}\ I_{dr} \\
\psi_{qs} &= (L_{os} + L_{mi})\ I_{qs} + L_{mi}\ I_{qr} = L_{ss}\ I_{qs} + L_{mi}\ I_{qr} \\
\psi_{dr} &= (L_{or} + L_{mi})\ I_{dr} + L_{mi}\ I_{ds} = L_{rr}\ I_{dr} + L_{mi}\ I_{dr} \\
\psi_{qr} &= (L_{or} + L_{mi})\ I_{qr} + L_{mi}\ I_{qr} = L_{rr}\ I_{qr} + L_{mi}\ I_{qr}
\end{aligned} \tag{4.2}$$

u_{ds} =d axis stator voltage, u_{qs} =q axis stator voltage, u_{dr} =d axis rotor voltage, u_{qr} =q axis rotor voltage, ψ_{ds} =d axis stator flux linkage,ψ_{qs} =q axis stator flux linkage, ψ_{dr} =d axis rotor flux linkage,ψ_{dr} =q axis rotor flux linkage, I_{ds} =d axis stator current, I_{qs} =q axis stator current,I_{dr} =d axis rotor current,I_{qr} =q axis rotor current, R_s =stator resistance, R_r =rotor resistance, L_{mi} =magnetizing inductance, L_{os} =stator leakage inductance, L_{or} =rotor leakage inductance, $L_{ss} = L_{os} + L_{mi}$=stator self inductance, $L_{rr} = L_{or} + L_{mi}$ =rotor self inductance, f_s =synchronous frequency, ω_r =rotor electrical frequency, ω_{sl} =slip angular frequency, $\omega_{sl} = \omega_s - \omega_r,\ \omega_s = 2\pi f_s,\ a_s = \frac{L_{mi}}{L_{rr}},\ a_r = \frac{L_{mi}}{L_{ss}},\ L_r = L_{rr} - \frac{L_{mi}^2}{L_{ss}},\ L_{\sigma s} = L_{ss} - \frac{L_{mi}^2}{L_{rr}},\ L_{\sigma r} = L_{rr} - \frac{{L_{mi}}^2}{L_{ss}}$.

4.2.1 Stator active and reactive power control (slow control loop)

It is intended to control the stator active power and reactive power by using the rotor q axis current and d axis current respectively for a given stator voltage (u_{ds}). Since stator resistance is very small [2], neglecting the stator resistance R_s , stator active and reactive power can be represented in terms of rotor current as follows.

$$P_s = -\frac{3}{2} u_{ds} \frac{L_{mi}}{L_{ss}} I_{dr} \tag{4.3}$$

$$Q_s = \frac{3}{2} u_{ds} \left[\frac{u_{ds}}{\omega L_{ss}} - \frac{L_{mi}}{L_{ss}} I_{qr} \right] \tag{4.4}$$

Rearranging (4.3) and (4.4), one obtains

$$i_{dr} = -\frac{2L_{ss}}{3u_{ds}L_{mi}} P_s \tag{4.5}$$

$$i_{qr} = \frac{2L_{ss}}{3u_{ds}L_{mi}}Q_s - \frac{u_{ds}}{\omega_s L_{mi}} \tag{4.6}$$

4.2.2 Inner rotor current control loop (Fast control loop)

From (4.7) and (4.8), it is necessary to compensate the cross coupled emf terms and induced emf due to stator flux disturbance in inner rotor current control loop. Rearranging (4.1) and (4.2), rotor voltage equations u_{dr} and u_{qr} can be obtained in terms of the rotor currents and stator flux as [22, 84] follows

$$\begin{aligned} u_{dr} &= R_r I_{dr} + \left[L_{rr} - \frac{L_{mi}^2}{L_{ss}}\right]\frac{dI_{dr}}{dt} - \omega_{sl}\left[L_{rr} - \frac{L_{mi}^2}{L_{ss}}\right] I_{qr} \\ &\quad - \omega_{sl}\frac{L_{mi}}{L_{ss}}\psi_{qs} + \frac{L_{mi}}{L_{ss}}\frac{d\psi_{ds}}{dt} \\ &= R_r I_{dr} + L_{\sigma r}\frac{dI_{dr}}{dt} - \omega_{sl}L_{\sigma r}I_{qr} - \omega_{sl}\frac{L_{mi}}{L_{ss}}\psi_{qs} + \frac{L_{mi}}{L_{ss}}\frac{d\psi_{ds}}{dt} \end{aligned} \tag{4.7}$$

let $u_{d1} = -\omega_{sl}L_{\sigma r}I_{qr}$ is the cross coupled induced emf on d axis voltage due to q axis rotor current, $u_{d2} = -\omega_{sl}\frac{L_{mi}}{L_{ss}}\psi_{qs}$ is the induced emf due to q axis stator flux, $L_{\sigma r}$ is the equivalent inductance from rotor side with stator terminals short circuited.

$$\begin{aligned} u_{qr} &= R_r I_{qr} + \left[L_{rr} - \frac{L_{mi}^2}{L_{ss}}\right]\frac{dI_{qr}}{dt} + \omega_{sl}\left[L_{rr} - \frac{L_{mi}^2}{L_{ss}}\right] I_{dr} \\ &\quad + \omega_{sl}\frac{L_{mi}}{L_{ss}}\psi_{ds} + \frac{L_{mi}}{L_{ss}}\frac{d\psi_{qs}}{dt} \\ &= R_r I_{qr} + L_{\sigma r}\frac{dI_{qr}}{dt} + \omega_{sl}L_{\sigma r}I_{dr} + \omega_{sl}\frac{L_{mi}}{L_{ss}}\psi_{ds} + \frac{L_{mi}}{L_{ss}}\frac{d\psi_{qs}}{dt} \end{aligned} \tag{4.8}$$

Let $u_{q1} = \omega_{sl}L_{\sigma r}I_{dr}$ is the cross coupled induced emf on q axis voltage due to d axis rotor current, $u_{q2} = \omega_{sl}\frac{L_{mi}}{L_{ss}}\psi_{ds}$ is the induced emf due to d axis stator flux. In simplified form (4.7) and (4.8) can be rewritten as

$$\begin{aligned} u_{dr} &= u'_{dr} + u_{d1} + u_{d2} \\ u_{qr} &= u'_{qr} + u_{q1} + u_{q2} \end{aligned} \tag{4.9}$$

where u'_{dr} and u'_{qr} are the outputs of the PI controller. u_{d1}, u_{q1}, u_{d2} and u_{q2} are the feed

forward compensation terms.

$$\begin{aligned} u'_{dr} &= k_p(I_{dr_{Ref}} - I_{dr}) + \frac{k_i}{\omega_s}\int (I_{dr_{Ref}} - I_{dr})dt \\ u'_{qr} &= k_p(I_{qr_{Ref}} - I_{qr}) + \frac{k_i}{\omega_s}\int (I_{qr_{Ref}} - I_{qr})dt \end{aligned} \tag{4.10}$$

where k_p and k_i are the proportional and integral gains, $u_1 = u_{d1} + ju_{q1}$ is the cross coupled emf, $u_2 = u_{d_2} + ju_{q_2}$ is the induced emf due to stator flux. The main objective in inner rotor current control loop is to compensate the cross coupling induced emf and emf induced due to stator flux using feedforward compensation by employing the optimal preview control.

4.3 State space model of DFIG

Based on (4.1) and (4.2), state space model of the DFIG can be derived. DFIG dynamic equations in $d-q$ synchronous reference frame can be linearized and the resulting discrete time space model of the DFIG is given by

$$x(k+1) = Ax(k) + Bu(k-1) + Cd(k) \tag{4.11}$$

$$y(k) = Ex(k) \tag{4.12}$$

where the state vector x(k) is defined as

$$x(k) = [u_{dr}(k)\ u_{qr}(k)\ I_{ds}(k)\ I_{qs}(k)]^T \tag{4.13a}$$

$$u(k) = [u_{ds}(k)\ u_{qs}(k)\ ]^T \tag{4.13b}$$

$$y(k) = [\ I_{dr}(k)\ I_{qr}(k)]^T \tag{4.13c}$$

$$d(k) = \psi_{dqs}(k) \tag{4.13d}$$

where $x(k+1)$ is the future state variable, k denotes k^{th} sampling instant, $x(k)$ is model state variable, $u(k)$ is control input variable, $y(k)$ is output variable and $d(k)$ is disturbance signal. A, B, C, E are constant matrices with dimensions $(6\times6), (6\times4), (6\times1), (5\times6)$ respectively. One sampling delay period is provided to the input vector for compensating the execution

time of the processor. Matrices A, B, C, E are given as

$x_{31} = -\frac{1}{\omega_s L_{\sigma r}}, x_{33} = -\frac{1}{L_{\sigma r}}\left[1 + R_r\right],$

$$x_{34} = \left(\frac{-\omega_{sl}+a_s a_r \omega_s}{-1+a_s a_r}\right) - \frac{\omega_{sl}}{L_{\sigma r}}\left(L_{\sigma r} + a_r L_{mi}\right),$$

$$x_{35} = \frac{-R_s a_r}{L_{\sigma r}}, x_{36} = \frac{-a_s \omega_r}{-1+a_s a_r} + \frac{\omega_{sl} a_r L_{ss}}{L_{\sigma r}},$$

$$x_{42} = \frac{1}{\omega_s L_{\sigma r}}, x_{43} = -\left(\frac{-\omega_{sl}+a_s a_r \omega_s}{-1+a_s a_r}\right) + \frac{\omega_{sl}(L_{\sigma r}+a_r L_{mi})}{L_{\sigma r}},$$

$$x_{44} = -\frac{1}{L_{\sigma r}}\left(1 + R_r\right), x_{45} = \frac{a_s \omega_r}{-1+a_s a_r} - \frac{\omega_{sl} a_r L_{ss}}{L_{\sigma r}},$$

$$x_{46} = \frac{-R_s a_r}{L_{\sigma r}}, x_{51} = -\frac{1}{\omega_r}\frac{L_m}{L_{rr} L_{\sigma s}}, x_{53} = \frac{-a_s}{L_{\sigma s}}\left(1 + R_r\right),$$

$$x_{54} = -\left(\frac{a_r \omega_r}{-1+a_s a_r}\right) - \frac{a_s}{L_{\sigma s}}\left(L_{\sigma r} + a_r L_{mi}\right), x_{55} = -\frac{R_s}{L_{\sigma s}},$$

$$x_{56} = \left(\frac{a_s a_r \omega_{sl}-\omega_s}{-1+a_s a_r}\right) + \frac{a_s a_r L_{ss}}{L_{\sigma s}}, x_{62} = -\frac{a_s}{\omega_r L_{\sigma s}},$$

$$x_{63} = -\left(\frac{a_r \omega_r}{-1+a_s a_r}\right) + \frac{a_s}{L_{\sigma s}}\omega_{sl}\left(L_{\sigma r} + a_r L_{mi}\right),$$

$$x_{64} = -\frac{a_s}{L_{\sigma s}}\left[1 + R_r\right],$$

$$x_{65} = -\left(\frac{a_s a_r \omega_{sl}-\omega_s}{-1+a_s a_r}\right) - \frac{a_s a_r L_{ss}}{L_{\sigma s}}, x_{66} = -\frac{R_s}{L_{\sigma s}}$$

$$y_{31} = y_{33} = y_{42} = \frac{1}{L_{\sigma r}}$$

$$y_{44} = \frac{a_r}{L_{\sigma r}}\left[-1 + \frac{\omega_{sl}}{\omega_s}\right]$$

$$y_{51} = y_{62} = \frac{a_s}{L_{\sigma s}}, y_{53} = -\frac{1}{L_{\sigma s}}$$

$$y_{64} = -\frac{1}{L_{6s}} + \frac{a_s \omega_{sl} a_r}{L_{6s} \omega_s}$$

Equation(4.13) shows that the DFIG has six state variables, two output variables and four control inputs. Flux is added as disturbance for analysis the stability of DFIG, since stator flux is a function in terms of both stator voltage and rotor current. Hence, cross coupling is present in between stator flux and rotor current.

Fig.4.4 depicts the structure of the proposed OPC. LQR OPC model is employed for

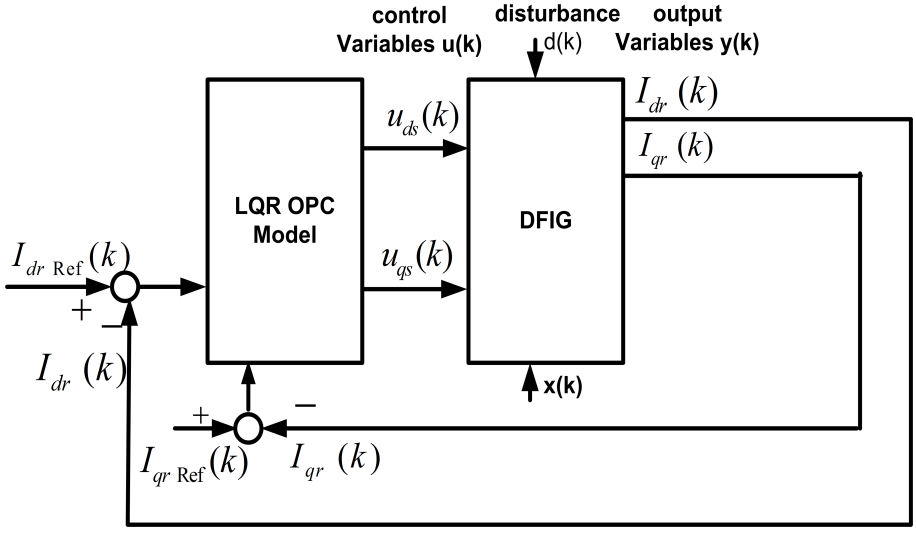

Figure 4.4: Structure of Proposed optimal preview control of DFIG

adjusting instantaneous values of rotor currents and to compensate the error in rotor control loop by using feed forward compensation terms(flux compensation and DFIG output currents compensation). By adjusting the stator voltage in such a way that $u_{sq} = 0$ and $u_{sd} = u_s$ where u_s is the stator nominal voltage.

4.4 Augmented Error System for DFIG

The objective of SVOC is to keep the stator voltage u_s constant by adjusting the rotor current arbitrarily. For achieving this objective, the stator flux linkages and cross coupling terms have to be eliminated with the help of feed-forward compensation. For minimizing the model uncertainties and disturbances, flux is considered as disturbance and the control system is synthesized for multi input(DFIG rotor voltages and stator currents) and multi output(rotor currents) system with LQR optimal regulatory theory. The augmented error

is defined as

$$e(k) = [e_{I_{dr}}(k)\ e_{I_{qr}}(k)]^T \tag{4.14}$$

and the reference signal is

$$r(k) = [I_{dr\,Ref}(k)\ I_{qr\,Ref}(k)] \tag{4.15}$$

The forward operator difference Δ of the error signal is defined as

$$\begin{aligned} \Delta e(k+1) &= \Delta r(k+1) - \Delta y(k+1) \\ &= \Delta r(k+1) - E\Delta x(k+1) \\ &= \Delta r(k+1) - E[A\Delta x(k) + B\Delta u(k-1) + C\Delta d(k) \end{aligned} \tag{4.16}$$

where $\Delta e(k) = e(k+1) - e(k)$

For achieving the robustness for DFIG parameter uncertainities, reference or desired signal second difference is defined as

$$\begin{aligned} \Delta^2 r(k+1) &= \Delta r(k+1) - \Delta r(k) \\ &= r(k+1) - 2r(k) + r(k-1) \end{aligned} \tag{4.17}$$

Similarly state vector $x(k+1)$ first difference is given by

$$\Delta x(k+1) = A\Delta x(k) + B\Delta u(k-1) + C\Delta d(k) \tag{4.18}$$

Equations(4.16-4.18) can be represented in matrix form as follows

$$\begin{aligned} \begin{bmatrix} \Delta e\,(k+1) \\ \Delta x\,(k+1) \end{bmatrix} &= \begin{bmatrix} I & \text{-EA} \\ 0 & \text{A} \end{bmatrix} \begin{bmatrix} \Delta e\,(k) \\ \Delta x\,(k) \end{bmatrix} + \begin{bmatrix} \text{-EB} \\ \text{B} \end{bmatrix} \\ &\Delta u\,(k-1) + \begin{bmatrix} I \\ 0 \end{bmatrix} \Delta^2 r\,(k+1) + \begin{bmatrix} \text{-CE} \\ \text{C} \end{bmatrix} \Delta d\,(k) \end{aligned} \tag{4.19}$$

$$x(k+1) = \phi x(k) + \zeta\Delta u(k-1) + \zeta_r\Delta^2 r(k+1) + \zeta_d\Delta d(k) \tag{4.20}$$

where $\phi, \zeta, \zeta_r, \zeta_d$ are the coefficient matrices

The above system equation (4.20) is the error state equation of DFIG which represents the error system dynamics. For optimum preview control, error system is the basic equation for synthesis of the control law. The objective of the OPC design is to set the output $y(k)$, such that q-axis voltage component of the stator is zero for SVOC and desired signal $r(k)$ is tracked with zero steady state error.

4.5 Optimal Preview Control Law

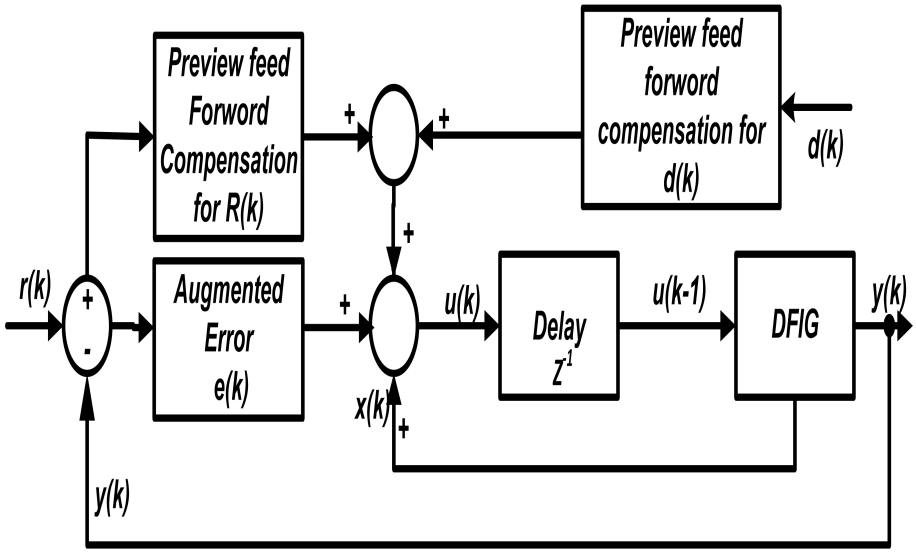

Figure 4.5: Structure of the Proposed Optimal Preview Controller

The proposed optimal preview controller comprises of a feedforward compensation loop for both output and disturbance. In Fig.4.5, augmented error system plays a vital role for tracking the desired response. The constraints in the error state equation $x(k+1)$ has to be minimized for tracking the desired DFIG output rotor currents by selecting the quadratic performance index formulated as follows

$$J_{opc} = \sum_{k=0}^{\infty} [x^T(k+1)Px(k+1) + \Delta u^T(k)Q\Delta u(k)] \tag{4.21}$$

where P and Q are weighing factors for state and control variables, $P \geq 0$ and $Q > 0$.

$$P = \begin{bmatrix} \Gamma_1\ 0\ 0\ 0\ 0\ 0 \\ 0\ \Gamma_2\ 0\ 0\ 0\ 0 \\ 0\ 0\ \Gamma_3\ 0\ 0\ 0 \\ 0\ 0\ 0\ \Gamma_4\ 0\ 0 \\ 0\ 0\ 0\ 0\ \Gamma_5\ 0 \\ 0\ 0\ 0\ 0\ 0\ \Gamma_6 \end{bmatrix},\ Q = \begin{bmatrix} h_1\ 0\ 0\ 0 \\ 0\ \mathrm{h}_2\ 0\ 0 \\ 0\ 0\ \mathrm{h}_3\ 0 \\ 0\ 0\ 0\ \mathrm{h}_4 \end{bmatrix}$$

From [85], optimal control input $\Delta u(k)$ for the error system equation $x(k+1)$ can be obtained with

$$\Delta u(k) = Fx(k) \tag{4.22}$$

$$\Delta u(k) = Fx(k) + \sum_{j=1}^{M_r} F_{PR}(j) r(k+j) \tag{4.23}$$

where $r(k+j) = \zeta_r \Delta^2 r(k+j) + \zeta_d \Delta d(k)$

$F = -[H + \zeta^T Z \zeta]^{-1} \zeta^T Z \phi$

$F_{PR} = -[H + \zeta^T Z \zeta]^{-1} \zeta^T [(\phi + \zeta F)^T]^{j-1} Z \zeta_R$

In preview control, the desired signal r varies periodically by M_r steps for closed loop system $(\phi + \zeta F)$. The LQR OPC controller is not complex, since feedback matrix and feed forward matrix are time invariant. Asymptotic solution for the Ricatti equation Z is given by

$$Z = P + (\phi + \zeta F)^T Z (\phi + \zeta F) + F^T H F \tag{4.24}$$

For simplicity, the above equation is splitted into three simpler Ricatti equations as follows

$$\begin{aligned} Z(k) &= P + \phi^T \lambda(k+1) \phi \\ \lambda(k+1) &= Z(k+1)[I_{14} - \zeta \gamma(k+1) \zeta^T Z(k+1)] \\ \gamma(k+1) &= [H + \zeta^T Z(k+1) \zeta]^{-1} \end{aligned} \tag{4.25}$$

where Z, λ, γ represent the steady state optimal solutions of the Ricatti equation. $u(k)$ can be obtained as follows

$$u(k) = -M(k)x(k) \tag{4.26}$$

where $M(k)$ is the Kalman gain which can be obtained by substituting the solutions of

Ricatti equations in the following equation

$$M(k) = [B^T(k)Z(k+1)B(k) + H(k)]^{-1} B^T(k)Z(k+1)A(k) \tag{4.27}$$

Thus the feedback gain can be determined from the following expression as

$$F = [f_1 f_2 f_3 f_4] = -\gamma \zeta^T Z \phi \tag{4.28}$$

Feed forward gains are given by

$$\begin{aligned} f_1 &= -\gamma \zeta^T Z \\ f_2 &= -\gamma \zeta^T \phi^T \lambda \\ f_j &= f_{j-1} k_1, j = 2, 3, 4, ..., M_r \end{aligned} \tag{4.29}$$

where $k_1 = Z^{-1}\phi^T\lambda$ The optimal feedback control law $u(k)$ can be obtained by substituting (4.29) in (4.26) yields

$$\begin{aligned} u(k) = f_1 \sum_{x=0}^{k} e(x) + (f_2 - f_1)e(k) + f_3 x(k) + f_4 u(k-1) + \\ \sum_{x=1}^{N_r} G_{rx}[\Delta r(k+x) - \Delta r(x)] + \sum_{x=1}^{N_d} G_{dx}[d(k+x-1) - d(x-1)] \end{aligned} \tag{4.30}$$

where $G_{rx} = G_x \zeta_r$ and $G_{dx} = G_x \zeta_d; x = 1, 2, 3.....,(N_r or N_d)$ $N_r, N_d \geq 1$ are the preview feed forward steps.

In (4.30), $f_1 \sum_{x=0}^{k} e(x) + (f_2 - f_1)e(k)$ denotes the PI controller elements for error signal in DFIG. These terms are related to DFIG rotor side voltage dq terms given by (4.10).

The output of the PI controller is taken as the control input for optimum state feedback controller. The third term $f_3 x(k)$ in (4.30) represents the state feedback controller for closed path approaching origin of z plane. Fourth term $f_4 u(k-1)$ compensates for delay in processor computation time. Fifth term $\sum_{x=1}^{N_r} G_{rx}[\Delta r(k+x) - \Delta r(x)]$ represents preview feedforward compensation term $\Delta r(k+j) - \Delta r(j)$ is used to track the desired signal by compensating

the cross coupling induced emf $u_1 = u_{d1} + ju_{q1}$ of DFIG as

$$\begin{aligned} ud_1 &= \omega_{sl} L_{\sigma r} \left(-I_{qr}\right) \\ uq_1 &= \omega_{sl} L_{\sigma r} \left(-I_{dr}\right) \end{aligned} \tag{4.31}$$

Finally the last term in (4.30) is the disturbance feed forward compensation term $d(k+x-1) - d(x-1)$ which eliminates the induced emf associated with disturbance flux as

$$\begin{aligned} u_2 = u_{d_2} + ju_{q_2} &= (\omega_s - \omega_r)\frac{L_m}{L_{ss}}(-\psi_{qs} + j\psi_{ds}) \\ &= \omega_{sl}\frac{L_m}{L_{ss}}(-\psi_{qs} + j\psi_{ds}) \end{aligned} \tag{4.32}$$

4.6 Design of controller for Voltage source converter with optimised rotor current dynamics

In Fig.4.6 the outputs $I_{dr}(k)$ and $I_{qr}(k)$ of the optimum preview control are considered for generating the PMW pulses to control the VSC [both the grid side and generator side].

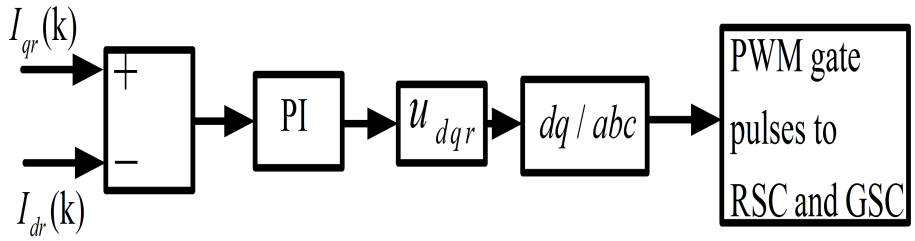

Figure 4.6: Controller design for VSC using current regulator

Rotor currents are fed to PI controller both on RSC and GSC which results in u_{dq_r} synchronous rotating voltage. u_{dq_r} which is transformed into $3-\phi$ stationary voltage by using Park transformation given in [48]. These three phase voltages will act as modulating pulses for generating PWM gate pulses for RSC and GSC. Modulation Index m required for obtaining 1pu generated voltage by the converter is given by $m = u_{dc} \times 2 \times \sqrt{\left(\frac{2u_{dc}}{3}\right)}$ when u_{abc} is the RMS phase to phase voltage.

4.7 Results and Discussion

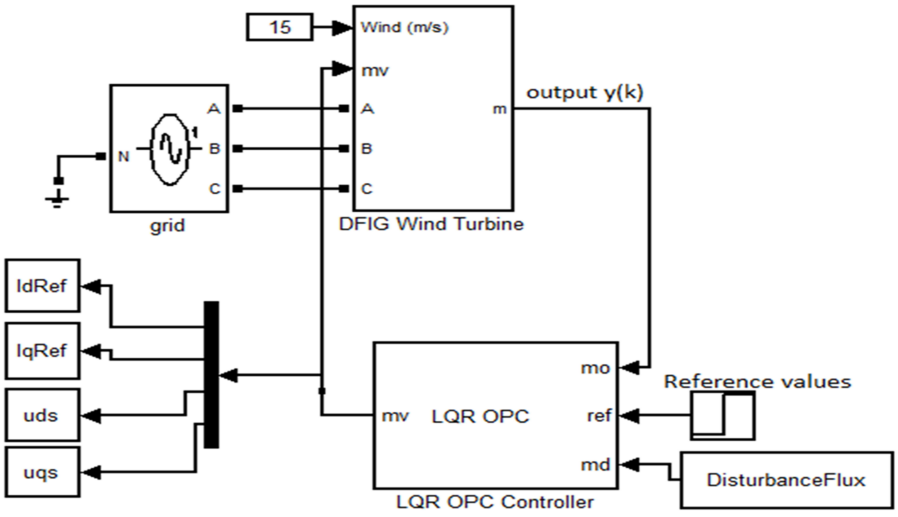

Figure 4.7: Implementation of LQR OPC in DFIG WECS using SIMULINK

In order to verify the efficacy of the proposed LQR OPC in a DFIG based WECS using SVOC, simulation set up has been proposed using MATLAB/SIMULINK in Fig.4.7 and then by using RTLAB in Fig.4.8, Fig.4.9, Fig.4.10, Fig.4.11 and Fig.4.12. The parameters are taken from experimental set up for the DC machine and DFIG, which are used for simulation. The parameters are listed in Table 4.1 and Table 4.2.

Table 4.1: DC Machine Parameters

Parameter	Rating
Power rating	1.5 kW
Armature Voltage	180V
Armature current	8A
Field current	0.3A
Inertia(J)	0.006 kgm^2

In Fig.4.7, DFIG coupled with the wind turbine has been simulated for active and reactive power control of WECS. The stator of DFIG is directly connected to grid and the rotor is fed to grid through power electronic converters. LQR OPC controller has been designed

Table 4.2: DFIG Parameters

Parameter	Rating
Rated Capacity	1HP
Synchronous speed	1500 rpm
Stator Resistance R_s	9.3 Ω
Rotor referred resistance R_r	3.5Ω
Stator Inductance L_s	0.248H
Rotor referred inductance L_r	0.086H
Mutual Induccctance L_{mi}	1H
Shaft Inertia	$0.008kgm^2$
Number of poles	4
frequency	50Hz
Rated Voltage(line to line)	415V
DC-link voltage	350V
DC-link Capacitor	1300×10^{-6}F
Moment of Inertia (J)	0.025 kgm^2
Stator voltage	415V Star connection
Stator Current	2.4A
Rotor Voltage	230V Star connection

with rotor current dynamics of DFIG. Actual output values of rotor currents are set at m_o and the reference values of rotor currents are set at m_f and the disturbance flux m_d is taken as feed forward compensation term in LQR OPC controller as shown in Fig.4.7. The control outputs are fed to DFIG along with state variables. In LQR OPC controller, feed forward compensation has been applied for both the desired rotor current signals and the disturbance flux. Finally the outputs obtained from LQR OPC controller are taken as control inputs for controlling the DFIG, which ultimately controls the active and reactive power of WECS.

For implementing the MATLAB/SIMULINK design in RT lab environment, three subsytems have to be created defined as Master Subsystem, slave subsystem and console subsystem.

In Fig.4.8, the master slave subsystem has two slave subsystems, namely one is LQR OPC slave subsystem and the other is drive train slave subsystem. Master Subsystem consists of all the computational elements of the model, the mathematical operations, the I/O blocks, the signal generators. In Fig.4.9 master subsystems has been designed which consists of

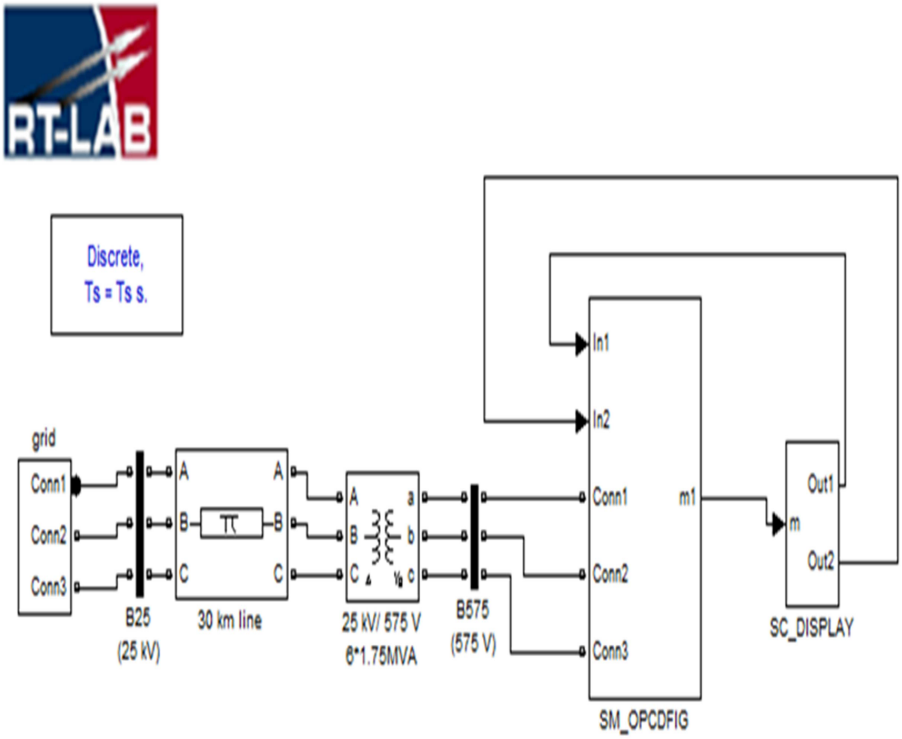

Figure 4.8: Simulation of DFIG WECS using RT LAB

DFIG wind turbine design, OPC control design and drive train subsystems with NARMAX model design as slave subsystems. In Fig.4.10, LQROPC slave subsystem has been designed for LQROPC algorithm in MATLAB/SIMULINK s-function. In Fig.4.11, console subsystem has been designed for observing the outputs of DFIG WECS(voltage, current, power, power factor,phase angle, flux quantities, pitch angle and phase angles).

All the computational outputs are inserted in slave subsystem which are required for computation when distributed across multiple nodes. Host computer is interfaced with the target RT Lab system using TCP/IP as shown in Fig.4.12.

Since the proposed LQR is based on optimal regulator theory, the weighting factor values (P, Q) in the performance index are predetermined. Two steps have to be followed for SVOC to bring the system to the steady state very quickly. Initially, the values of weighting factors for error terms $I_{dr\,\mathrm{ref}} - I_{dr}$ and $I_{qr\,\mathrm{ref}} - I_{qr}$ of the output current are made large.

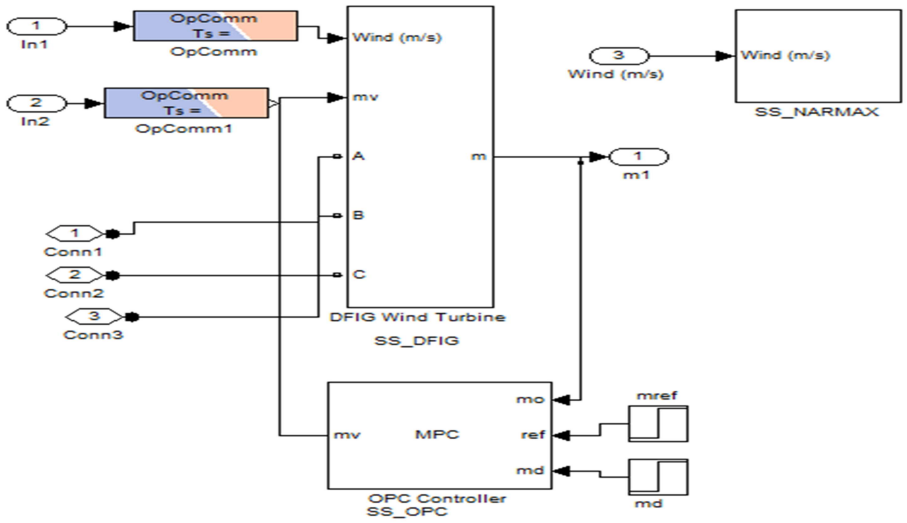

Figure 4.9: Design of Master Subsystem using RT LAB

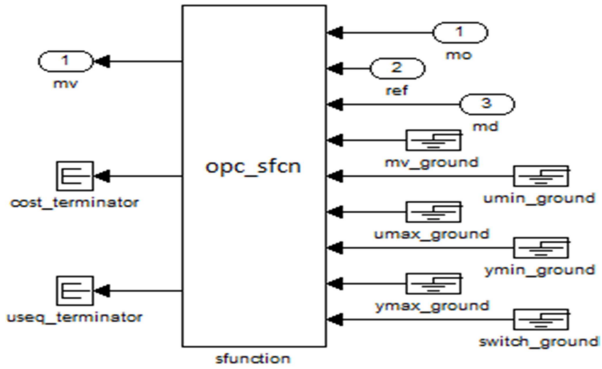

Figure 4.10: Design of Slave Subsystem of LQR OPC

The control input weighting factors (h_1, h_2, h_3, h_4) of eq(4.21) are selected by trial and error so that the current dynamics becomes faster to reach the steady state quickly. For achieving steady state, the values of performance Index for P and Q in eq(4.21)are chosen arbitrarily as follows $\Gamma_1 = 4, \Gamma_2 = 16, \Gamma_3 = 20, \Gamma_4 = 25, \Gamma_5 = 28, \Gamma_6 = 30$, $h_1 = 30, h_2 = 15, h_3 = 25, h_4 = 12$. Coefficient matrices A and B vary around the steady state operating point of (I_{dr}, I_{qr}). The control objective is that the stator voltage u_{ds} should follow u_s by making $u_{qs} = 0$ as depicted in Fig.4.14(b). The simulation model of DFIG WECS is implemented for Fig.4.4 and Fig.4.5 as described in section 4.3 and 4.4 based on state equations for LQR OPC with stator voltage oriented control.

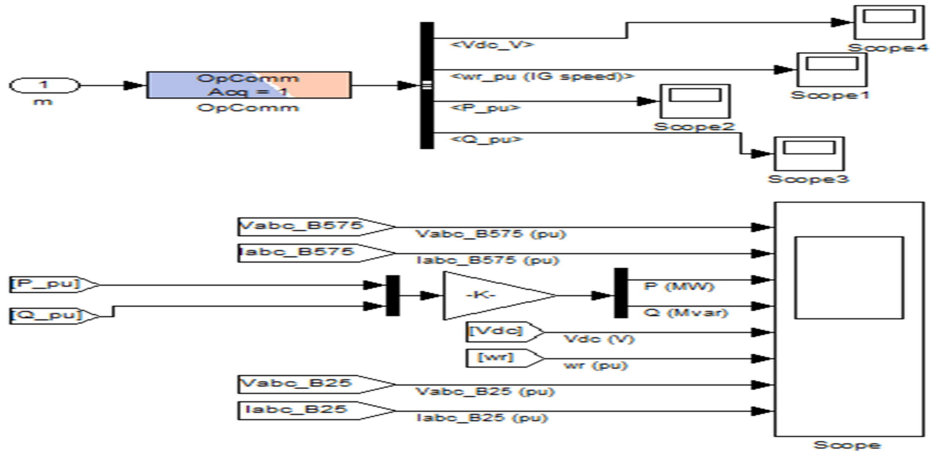

Figure 4.11: Design of Console Subsystem of DFIG WECS using RT LAB

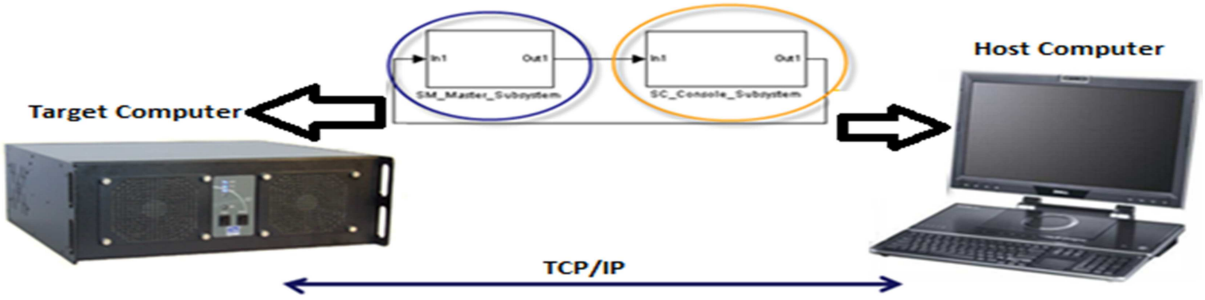

Figure 4.12: Interfacing host computer and RT lab

The step responses for different parameters are shown in Fig.4.13(a)to Fig.4.13(c), Fig.4.14(a)to Fig.4.14(c) and Fig.4.15(a)to Fig.4.15(c). The responses of various parameters are plotted in Fig.4.13(a)to Fig.4.13(c), Fig.4.14(a)to Fig.4.14(c) and Fig.4.15(a)to Fig.4.15(c)respectively by considering the flux as disturbance element from 0.6 to 2.6 sec. In feedforward controller for preview control, large values of M_r makes the response to vary from desired reference rotor current signal (r) to output rotor current response of DFIG(y) quickly. But the computation time increases if M_r is large, so M_r is taken only 10 preview steps for reaching the steady state.

The stator active and reactive power have been controlled by using rotor currents I_{dr} and I_{qr} respectively by keeping the stator voltage constant as shown in Fig.4.13(a)-(b). Fig.4.13(a)-(b)show that during normal operation, active power P is in steady state and during transient period(i.e 0.6 to 2.6 sec), reactive power variation is more than the active power. In

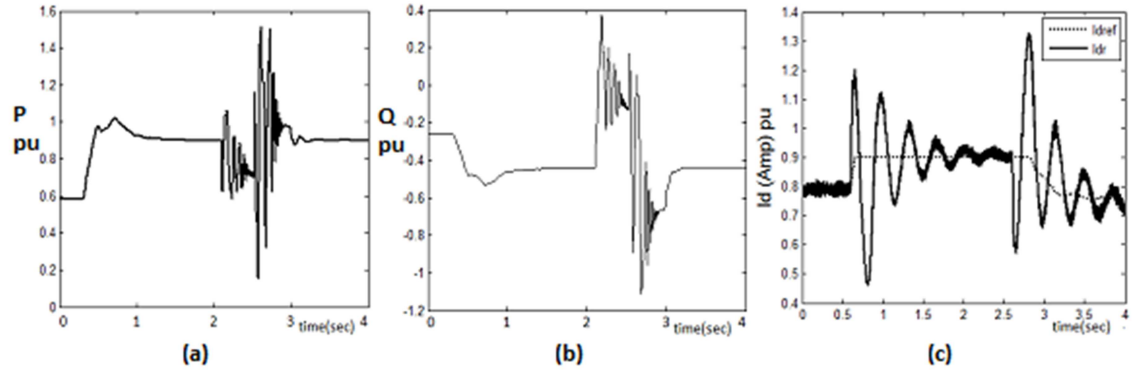

Figure 4.13: Performance plots for power, d axis rotor current versus time for LQR OPC controller

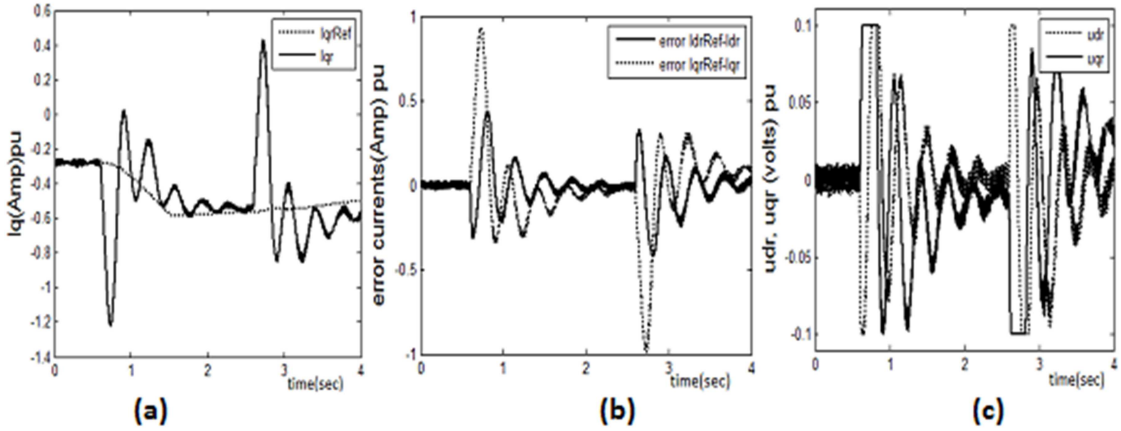

Figure 4.14: Performance plots for q axis rotor current and error currents and error voltages versus time for LQR OPC controller

Fig.4.13(c), *d*-axis rotor current for desired and reference currents have been shown, where desired signal is following the reference signal after 2.6 sec. *d*-axis rotor current exhibits large transient between 0.6 to 2.6 sec, but due to preview steps followed in LQR-OPC, I_{dr} reaches to $I_{dr\text{ref}}$ within 2.6 sec by forcing steady state error to zero. In Fig.4.14(a) I_{qr} is the q axis actual rotor current which tracks the reference current $I_{qr\text{Ref}}$ after 2.6 sec after performing the feedforward compensation for measured disturbances. In Fig.4.14(b), the error current dynamics for *dq*-axis are shown, where the error decays almost to zero at steady state at 2.6 sec. The d and q axes currents are obtained by taking the difference of reference and actual output rotor currents.In Fig.4.14(c), *dq* axis rotor voltage variations are observed. Since the

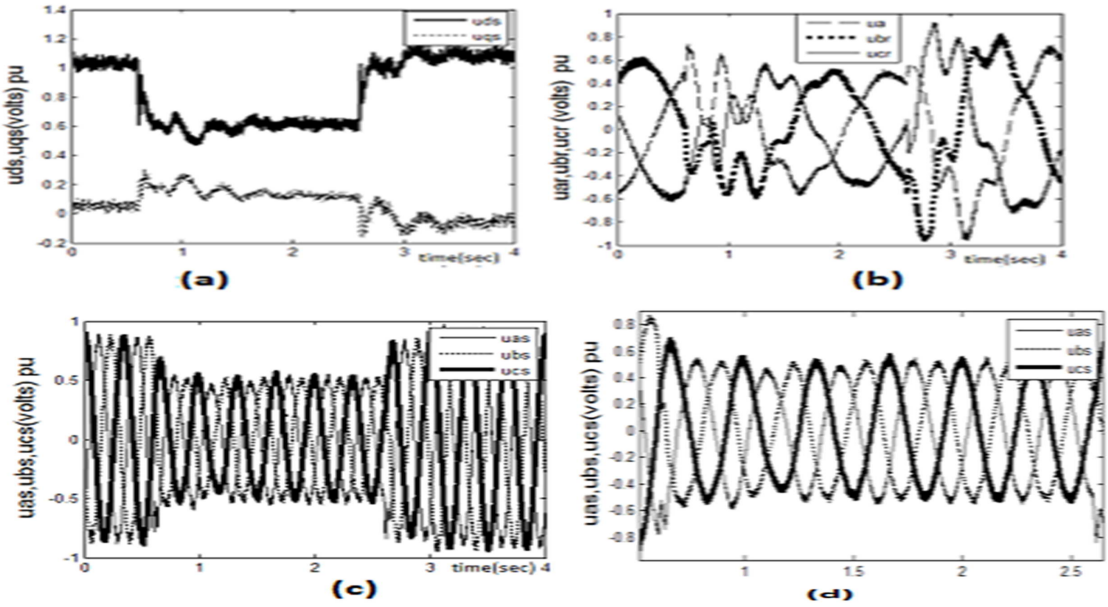

Figure 4.15: Performance plots for stator and rotor voltages versus time for LQR OPC controller

stator voltage is considered in SVOC instead of flux in FOC, the rotor voltages for both d and q axes converge to zero at the steady state.

From Fig.4.15(a), it is observed that u_{qs} becomes zero, thus the objective is achieved. This results in steady state voltage for $u_{ds} = u_d$, where $u_d = \sqrt{u_{ds}^2 + u_{ds}^2} = u_{ds}$. i.e at steady state, at approximately 2.6 sec, d axis stator voltage coincides with the stator voltage u_{ds}, making q axis stator voltage zero. In Fig.4.15(b) and Fig.4.15(c), three phase voltages on rotor and stator side of the DFIG are shown, from which it is observed that large transients occur during flux disturbances arising from 0.6 to 2.6 sec and the zoomed part of transient from 0.6 to 2.6 sec in Fig.4.15(c) is shown in Fig.4.15(d). The purpose of considering the rotor current control dynamics using SVOC is to eliminate the stator flux disturbance, so that the cross coupling effects of induced emfs shown in Fig.4.15(b) and Fig.4.15(c) is reduced. In Fig.4.16(a),Fig.4.16(b) and Fig.4.16(c), the flux disturbances for d, q and dq-axes are considered as external noise signals. Flux is considered as an external disturbance and observed the variations for rotor current control dynamics and cross coupling effects on induced emfs due to rotor currents. By considering the preview feedforward compensation, the fifth term of (4.30) is used to converge the desired signal by compensating the cross coupling induced

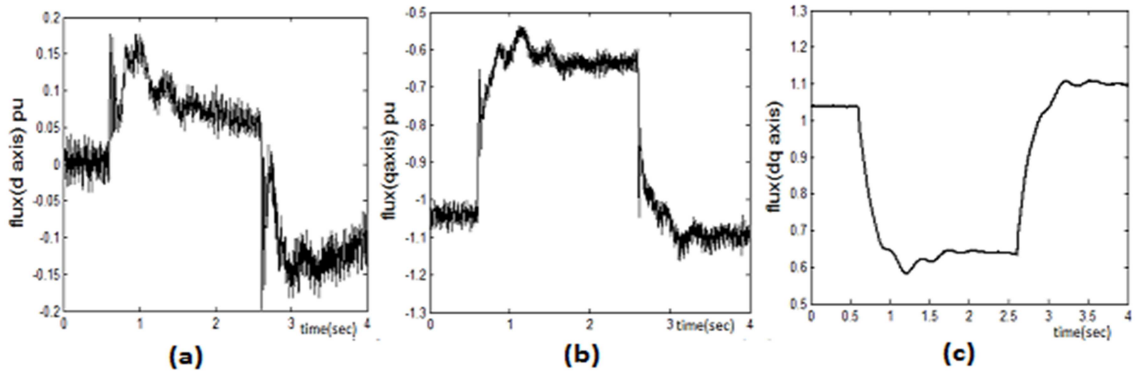

Figure 4.16: Performance plots for flux versus time for LQR OPC controller

emf of the DFIG.

In Fig.4.17, the performances of the proposed LQR OPC SVOC are compared with that of the SM-DTC and SM-FOC for active power, reactive power and rotor currents (d and q axes). In Fig.4.17(a), transient and steady state stability analyses have been presented. During transients from 0.6 to 2.6 sec, active power deviate from 300 W and reached steady state faster in case of LQR OPC SVOC as compared to the SM-FOC and SM-DTC. In Fig.4.17(b), reactive power becomes zero at 2.6 sec with the proposed LQR OPC control technique. In Fig.4.17(c)-(d), transients are shown for rotor d and q axes respectively in pu. It has been observed that transients are very less and the rotor currents are around 1 pu reaching to steady state at a faster rate.

4.8 Experimental set up

Fig.4.18 shows the picture of the experimental set up for DFIG WECS. It has the following components namely intelligent power module (IPM), DSPIC 4011 DSP controller, OPAL-RT simulator, three flat ribbon cables (FRC) and it has a VPE SPARTAN6 FPGA module.
IPM consists of six IGBT and diodes, four hall effect current sensors for measuring DC link voltage and three output currents of inverter bridge, one hall effect DC voltage sensor to sense the DC link voltage. All the PWM signals are isolated by an opto isolator and are fed to the FPGA/DSP controller through a flat ribbon cable.

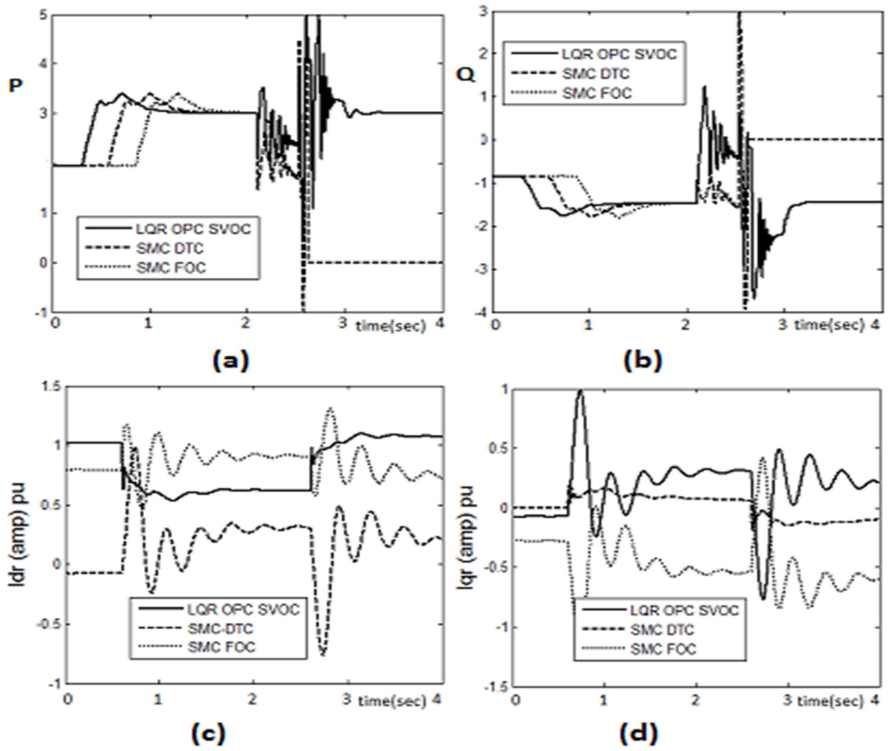

Figure 4.17: Comparison of active power, reactive power and rotor d and q axis currents for LQROPC,SMC-DTC and SMC-FOC controllers

The DSPIC controller has a Quadrature Encoder Interface(QEI) which provides interface to incremental encoders to obtain mechanical position data of the DFIG rotor. QEI has three outputs, such as phase A, phase B and an index pulse. These signals are necessary for position and speed control of the DFIG. If phase A leads phase B,then the direction of the motor is forward or positive. If Phase A lags Phase B, then the direction of the motor is reverse or negative. A third output termed as index pulse which occurs once per revolution is used as a reference to establish an absolute position.

DC shunt motor is coupled with slip ring induction motor. A shaft encoder is mounted on the DC shunt motor for speed tracking and for setting absolute position of the rotor through quadrature encoder interface. The DC shunt Motor coupled with slipring motor set are used as an emulator of wind turbine.

Fig.4.19 shows the V model for RT lab simulator. Initially modelling of DFIG WECS is performed using MATLAB/SIMULINK. Then the OPC algorithm is implemented through

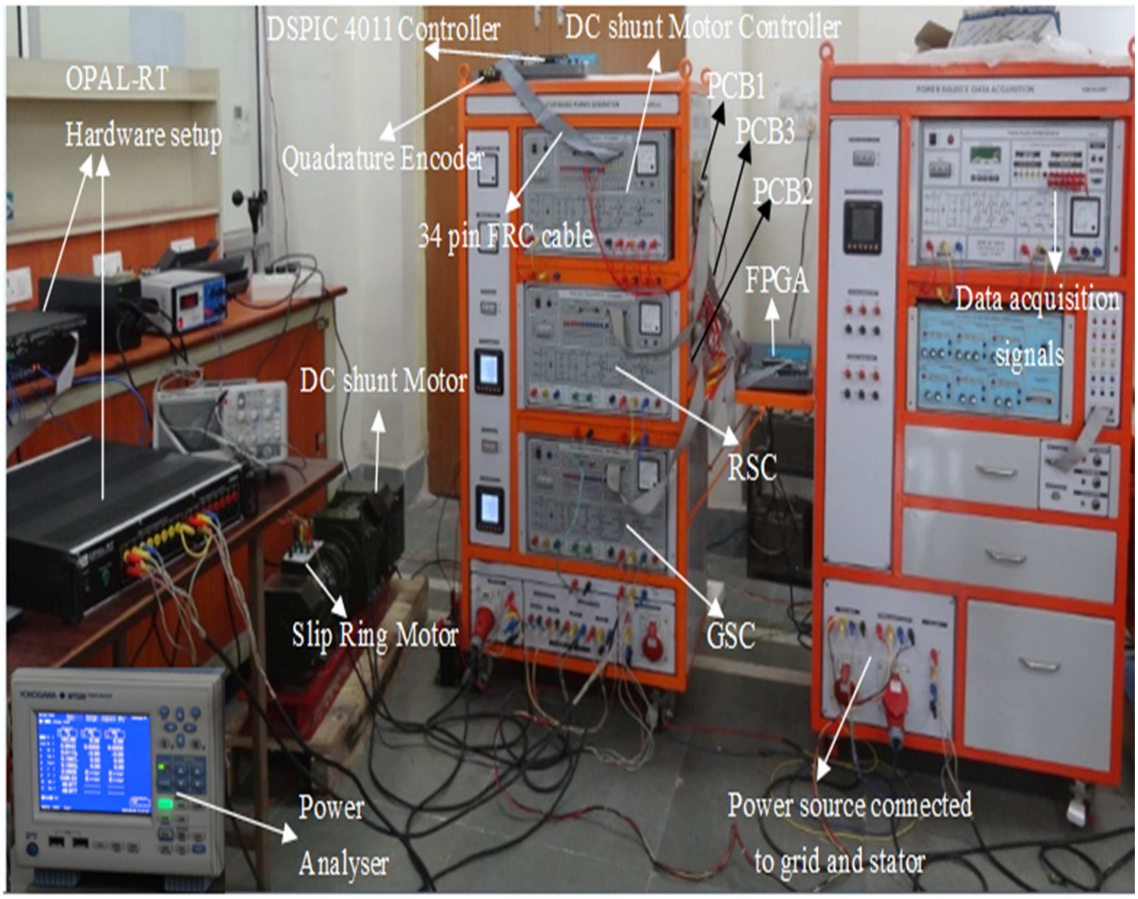

Figure 4.18: Experimental setup for DFIG WECS using RT-LAB simulator

rapid control prototyping (RCP). Automatically code generation is then initiated for LQR OPC control algorithm. Later, the algorithm is tested by using the RT lab simulator through hardware-in-the-loop (HIL). Finally if no fault is found, then the control algorithm is implemented in hardware for validation. Fig.4.20 shows the RT lab set up of DFIG WECS. The OPC algorithm is implemented in MATLAB/SIMULINK and the control algorithm is implemented in the OPAL RT real-time digital simulator. High voltage and current measurements are interfaced with signal conditioning unit shown in Fig.4.20. RT lab simulator results are interpreted and validated through experimental set up.

By using a $3-\phi$ variac, $3-\phi$ voltage is given to the stator and GSC which are in parallel with the stator. The RSC terminals are connected to rotor $3-\phi$ terminals of DFIG. Zero

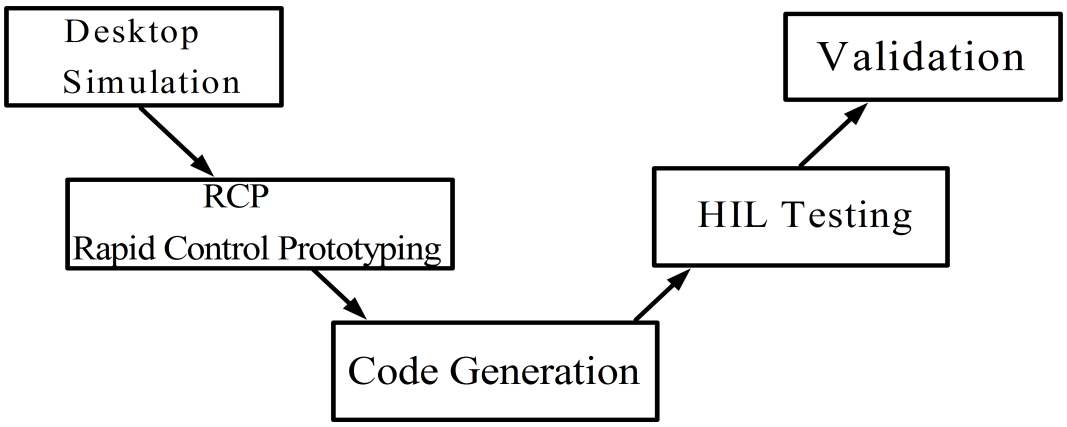

Figure 4.19: V model for RT lab Simulator

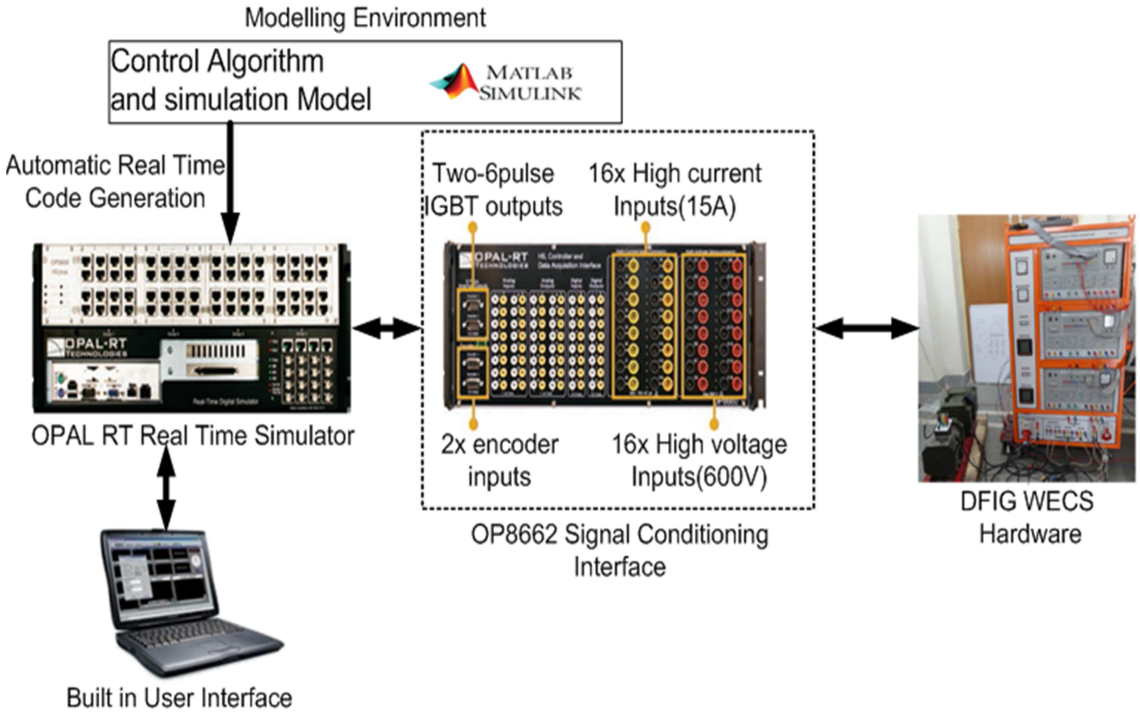

Figure 4.20: Block diagram for RT Lab set up of DFIG WECS

crossing detector(ZCD) output, that is $1-\phi$ phase input is given to the DC shunt motor IPM module. By using a 34 pin FRC cable(speed sensor interface card), DC shunt motor IPM module is interfaced to the DSPIC 4011 controller which senses the speed of DC shunt motor through quadrature encoder. The DSPIC controller generates PWM pulses which are fed to the DC shunt motor IPM module for operating the speed of DC shunt motor by setting the closed loop speed(sub and super synchronous speed). In the closed loop, set speed is equal to the actual speed. Now shunt motor speed (set speed) is given to PCB1 as input. PCB1 output (speed sensor output) is then given to FPGA which inturn generates PWM pulses which are given as input to IPM for the RSC. Then the wind speed is set in the FPGA as sub and super synchronous speeds, followed by setting the actual power as 300W, 450W. FPGA generates PWM pulses through 34 pin FRC cable and send to PCB2 which are given to the GSC through the 20 pin FRC. Finally readings of stator and rotor of DFIG are taken from PCB3 through the 26 pin FRC cable connected to FPGA. PCB3 is used as connector in between DFIG and FPGA. From FPGA, various parameters such as stator voltage and current, rotor voltage and current, active power, reactive power, power factor, phase angle, frequency of voltage and current and total harmonic distortion are analysed in both numeric and waveform analyses with the help of a power analyser.

4.9 Sub synchronous mode

Fig.4.1 show the schematic diagram of the wind turbine emulator based power generation of DFIG for grid connected system.

Fig.4.21,4.23 shows the numeric data analysis for subsynchronous mode i.e at a speed of N=1300rpm and active power set at P=300W, 450W respectively. For the same numeric data, waveform analysis is performed for phase voltage and current for all the elements such as the open circuit, R-phase, Y-phase, B-phase, GSC and RSC as shown in Fig.4.22 and 4.24. It is observed from Fig.4.22,4.24 that the GSC voltage(U5),current(I5) are in phase and the power P is positive, which signifies that the power is fed from the grid to the rotor side in the subsynchronous mode due to the fact that grid power is less than than the rotor power, but the stator R-phase, Y-phase, B-phase voltages(U2,U3,U4) and currents(I2,I3,I4) are out of

phase and the values of P are negative which signifies that power is generated by the stator. In subsynchronous mode, on grid side power factor is positive which makes the angle<90 degrees, i.e the GSC acts as a rectifier. It is observed that the total harmonic distortions for voltage and currents for all the elements described was below 5 % thus satisfy to the grid codes both in subsynchronous and supersynchronous modes. In sub synchronous mode, grid supplies power and GSC acts as rectifier which converts AC to DC and capacitor(battery) stores the DC voltage and is fed to the RSC which acts as an inverter for converting DC to AC and AC is fed to the rotor through the RSC. Now rotor rotates if excitation is given through DC shunt motor.

The proposed LQROPC control algorithm has been applied both in sub synchronous and super synchronous modes. Table 4.3 shows the representation of different element readings taken by using a Yokogawa power system analyser. Open circuit condition, stator R-phase, Y-phase, B-phase parameters and GSC and RSC parameters are measured as shown in Table 4.3. Various parameters such as Vrms, Irms, active power, apparent power, reactive power, power factor, phase angle, total harmonic distortion for voltage and current are measured as shown in Table 4.3.

4.9.1 Sub synchronous mode for N=1300 rpm and P=300 w of DFIG WECS

Fig.4.21 and Fig.4.22 show the numeric data and waveform analysis for the sub synchronous operation mode with speed set at N=1300 rpm and active power set at P=300 w. In the sub synchronous mode, actual speed is less than the rated speed(1500 rpm) of the DFIG. From Fig.4.21, open circuit voltage is defined where current is zero and open circuit voltage is 84.27 V. Since current is zero, active power, apparent power and reactive power are zero. Power factor and phase angle are observed as errors, since phase angle will not exist if current is zero.

R , Y and B phase voltages are set as 231.5V, 235.82V and 233.74V respectively. Current flowing in three phases are observed as 0.49A, 0.45A, 0.48A respectively. From the analysis of waveform given in Fig.4.22, it is observed that angle in between voltage and currents of R

phase(U2,I2), Y phase(U3,I3), B phase (U4,I4) are out of phase which signifies that active power is generated in all the three phases on stator side and the active powers generated are negative as shown in numerical data of Fig.4.21.

GSC and RSC are voltages are set at 231.7V and 125.37 V. Since a coupling transformer with turns 2:1 ratio is used on rotor side, rotor side voltage is approximately half of the stator and grid side voltages. From waveform analysis of Fig.4.22, it is observed that angle in between voltage and currents of GSC (U5,I5) are in phase which signifies that active power is absorbed on rotor side as indicted by a positive value of 0.0714kW in Fig.4.21. In sub synchronous mode, power factor on GSC is positive and phase angle is less than 90 degrees, which implies that the GSC acts as a rectifier and RSC acts as inverter for feeding the power from the grid to the rotor circuit. The grid supplies the power(314.3W) to the rotor side(71.4W) through power electronic converters. From Fig.4.21, it is observed that total voltage and current harmonic distortions are less than 5% adhering to the standard grid codes.

Table 4.3: Descriptions of the parameters for figures Fig.4.21,4.23,4.25,4.27

Parameter	Open Circuit (OC)	R-Phase (RP)	Y-Phase (YP)	B-Phase (BP)	GSC	RSC
Vrms[V]	OC voltage	RP voltage	YP voltage	BP voltage	GSC voltage	RSC voltage
Irms[A]	OC current	RP current	YP current	BP current	GSC current	RSC current
Active power P(W)	OC power	RP power	YP power	BP power	GSC power	RSC power
Apparent power S(VA)	OC power	RP power	YP power	BP power	GSC power	RSC power
Reactive power Q(Var)	OC power	RP power	YP power	BP power	GSC power	RSC power
Power Factor(pf)	OC pf	RP pf	YP pf	BP pf	GSC pf	RSC pf
Phase angle(ϕ)	OC ϕ	RP ϕ	YP ϕ	BP ϕ	GSC ϕ	RSC ϕ
Total voltage Harmonic Distortion VTHD	OC VTHD	RP VTHD	YP VTHD	BP VTHD	GSC VTHD	RSC VTHD
Total current Harmonic Distortion ITHD	OC ITHD	RP ITHD	YP ITHD	BP ITHD	GSC ITHD	RSC ITHD

	Open Circuit	R phase	Y phase	B phase	GSC	RSC
Vrms	84.27	231.50	235.82	233.74	231.70	125.37
Irms	0.0000	0.4918	0.4537	0.4827	1.3589	3.2440
Active Power (P)	-0.0000k	-112.66	-104.38	-111.59	0.3143k	0.0714k
Apparent Power (S)	0.0000k	113.85	106.98	112.82	0.3148k	0.4067k
Reactive Power (Q)	0.0000k	-16.43	-23.46	-16.58	0.0184k	0.4004k
Power Factor	Error	-0.9895	-0.9757	-0.9891	0.9983	0.1755
Phase angle	Error	D171.70	D167.33	D171.55	G3.36	G79.89
Voltage Harmonic Distortion	-------	1.420	1.392	1.578	1.420	-------
Current Harmonic Distortion	-------	4.261	5.506	6.176	1.545	-------

Figure 4.21: Sub synchronous numeric data for N=1300rpm and P=300w of DFIG WECS

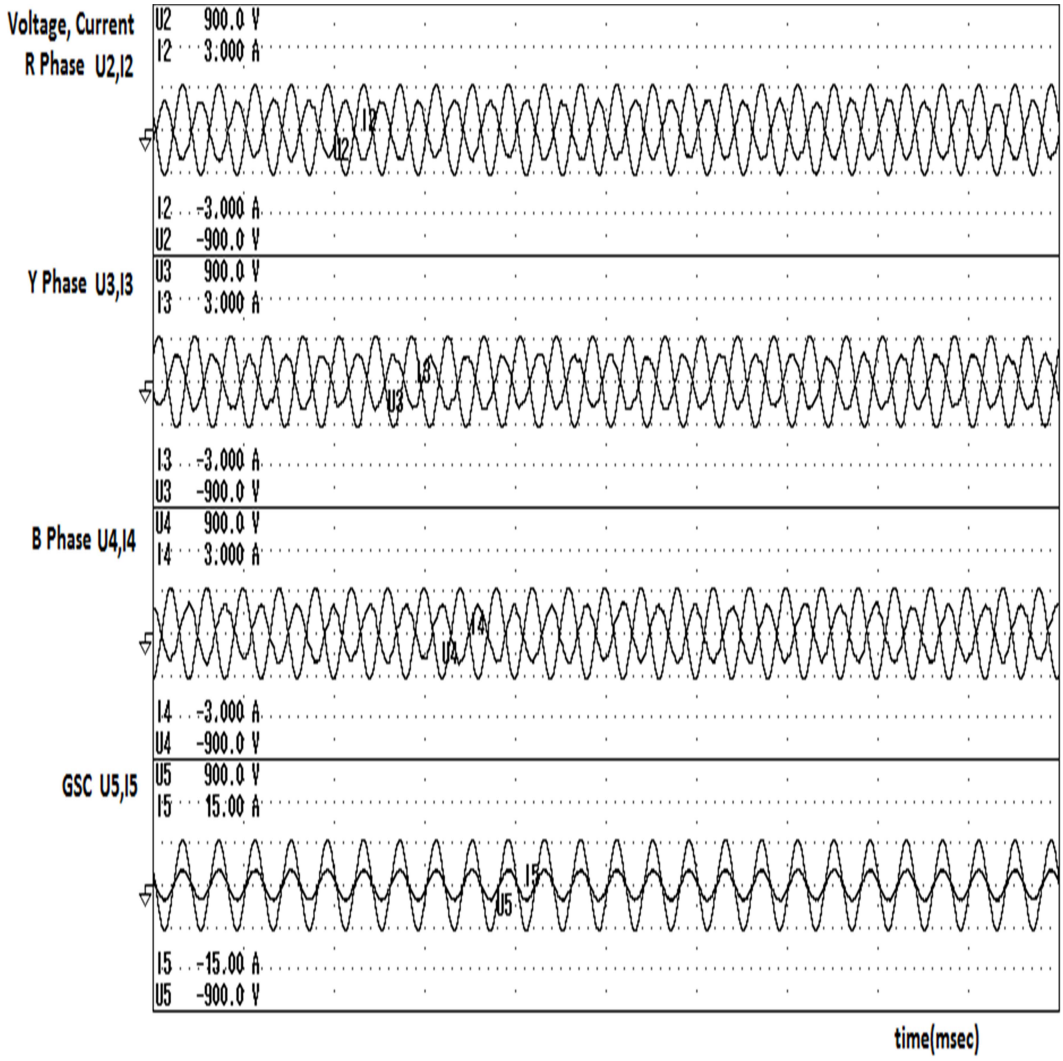

Figure 4.22: Subsynchronous waveform analysis for N=1300rpm and P=300w of DFIG WECS

4.9.2 Sub synchronous mode for N=1300 rpm and P=450 w of DFIG WECS

Fig.4.23 and Fig.4.24 show the numeric data and waveform analysis for subsynchronous operation mode with speed set at N=1300rpm and active power set at P=450w of DFIG WECS. From Fig.4.23, open circuit voltage is where current is zero and open circuit voltage is 87.35. Since current is zero, active power, apparent power and reactive power are zero. Power factor and phase angle are observed as errors, since phase angle will not exist if current is zero.
R phase, Y phase and B phase voltages are set at 4. 230.49V, 235.02V and 233.51V respectively. Current flowing in 3 phases are observed as 0.65A, 0.6A, 0.659A respectively. From waveform analysis in Fig.4.24, it is observed that angle in between (U2,I2), (U3,I3), (U4,I4) are out of phase which signifies that active power is generated in all the three phases on stator side and the active powers generated are negative as shown in numerical data of Fig.4.23.
GSC and RSC are voltages are set at 230.73V and 111.97 V. Since coupling transformer of 2:1 ratio is used on rotor side, rotor side voltage is approximately half of the stator and grid side voltages. From waveform analysis of Fig.4.24, it is observed that angle in between (U5,I5)is in phase which signifies that active power is absorbed on rotor side and the active power absorbed is indicted as positive value(0.0919kW) as shown in numerical data of Fig.4.21. In subsynchronous mode, power factor on GSC is positive and phase angle is less than 90 degrees, which implies that GSC will act as rectifier and RSC will act as inverter for feeding the power from grid to rotor circuit. Grid is supplying the power(371.5W) to the rotor side(91.9W) through power electronic converters. From Fig.4.23, it is observed that total voltage and current harmonic distortions are less than 5% adhering to the standard grid codes.

	Open Circuit	R phase	Y phase	B phase	GSC	RSC
Vrms	87.35	230.49	235.02	233.51	230.73	111.97
Irms	0.0000	0.6564	0.6075	0.6590	1.6112	3.7245
Active Power (P)	-0.0000k	-150.45	-141.03	-152.85	0.3715k	0.0919k
Apparent Power (S)	0.0000k	151.28	142.78	153.88	0.3718k	0.4170k
Reactive Power (Q)	0.0000k	-15.88	-22.29	-17.77	0.0151k	0.4068k
Power Factor	Error	-0.9945	-0.9877	-0.9933	0.9992	0.2204
Phase angle	Error	D173.98	D171.02	D173.37	G2.33	G77.27
Voltage Harmonic Distortion	-------	1.354	1.187	1.288	1.354	-------
Current Harmonic Distortion	-------	2.967	4.414	4.572	1.464	-------

Figure 4.23: Sub synchronous numeric data for N=1300rpm and P=450w of DFIG WECS

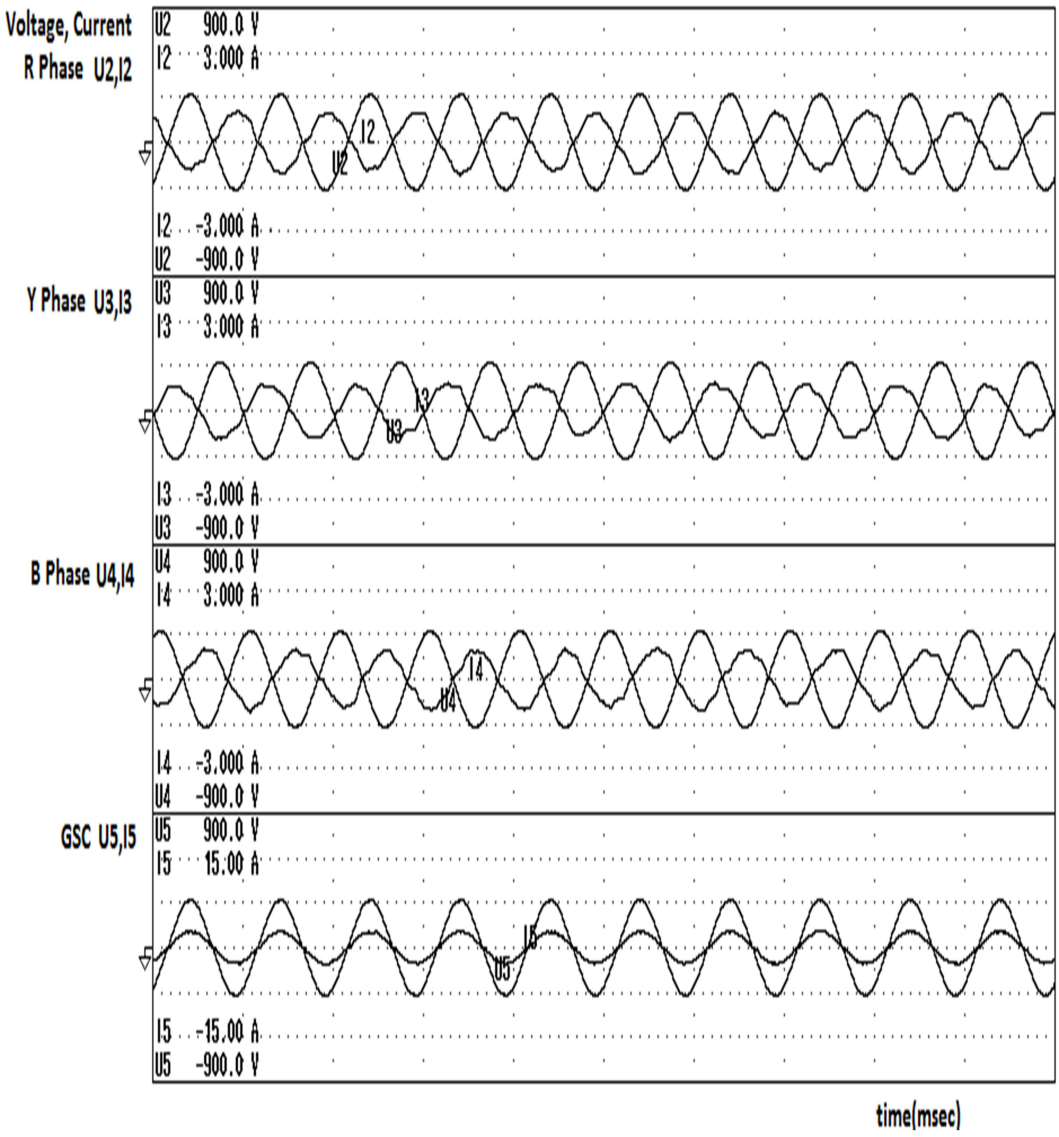

Figure 4.24: Subsynchronous waveform analysis for N=1300rpm and P=450w of DFIG WECS

4.10 Super synchronous mode

Fig.4.25,4.27 show the numeric data analysis for the supersynchronous mode with N=1700 rpm and active power set at different power values i.e. P=300W and P=450W respectively. For the same numeric data as in Fig.4.25 and Fig.4.27 waveform analysis is done for phase voltages and currents for all the elements as shown in Fig.4.26,4.28. It is observed from Fig.4.26,4.28, that GSC voltage(U5),current(I5) are out of phase and the power P is negative, which signifies that power is fed to the grid from stator and rotor sides in supersynchronous mode [rotor power >grid power]. In supersynchronous mode, in the grid side, power factor is negative which makes the angle>90 degrees, so that GSC acts as an inverter. In supersynchronous mode, stator and rotor feed power to grid and RSC will act as rectifier and GSC will act as inverter. Since rotor speed is above the rated speed, rotor generates power which causes DC link voltage to increase. For operating in closed loop control DC link voltage should be equal to set value. Because of change in DC link voltage, there is phase difference coming inbetween voltage and current. Due to phase difference, now power is fed to grid both from stator and rotor side. On GSC, PF and DC link voltage are regulated. In super synchronous mode, rotor side is controlled. Rotor side control means power generated is injected into the grid.

4.10.1 Super synchronous mode for N=1700 rpm and P=300 w of DFIG WECS

Fig.4.25 and Fig.4.26 show the numeric data and waveform analysis for super synchronous operation mode with speed set at N=1700 rpm and active power set at P=300 W of DFIG WECS. In super synchronous mode, actual speed is greater than than the rated speed(1500 rpm) of the slip ring motor. From Fig.4.25, the open circuit voltage is defined where current is zero and open circuit voltage is 77.42Volts. Since the current is zero, active power, apparent power and reactive power are zero.

R , Y and B phase voltages are set at 225.19V, 228.07V and 226.79V respectively. Current flowing in three phases are observed as 0.47A, 0.43A, 0.466A respectively. From the waveform analysis shown in Fig.4.26, it is observed that the angle between (U2,I2), (U3,I3), (U4,I4) are

out of phase. This signifies that active power is generated in all the three phases on stator side and the active powers generated are negative as shown in numerical data of Fig.4.25. GSC and RSC are voltages are set at 225.86V and 144.34 V. Since the coupling transformer with voltage ratio 2:1 ratio is used on rotor side, rotor side voltage is approximately half of the stator and grid side voltages. From the waveform analysis shown in Fig.4.26, it is observed that angle between (U5,I5)is out of phase i.e. active power is generated on rotor side and the active power generated is indicted as negative value(-0.0533kW) as shown in numerical data of Fig.4.25. In supersynchronous mode, power factor on GSC is negative and phase angle is greater than 90 degrees, which implies that GSC will act as inverter and RSC will act as rectifier for feeding the power from rotor side to grid side. Rotor is generating and supplying the power(-0.0533kW) to the grid side(-0.0472kW) through the VSI. From Fig.4.25, it is observed that total voltage and current harmonic distortions are less than 5% which is in the permissible limit specified by IEEE grid code.

	Open Circuit	R phase	Y phase	B phase	GSC	RSC
Vrms	77.42	225.19	228.07	226.79	225.86	144.34
Irms	0.0000	0.4763	0.4361	0.4669	0.2127	2.7454
Active Power (P)	-0.0000k	-103.90	-97.52	-101.25	-47.26	-0.0533k
Apparent Power (S)	0.0000k	107.27	99.46	105.90	48.03	0.3963k
Reactive Power (Q)	0.0000k	26.65	-19.54	31.03	-8.57	-0.3927k
Power Factor	Error	-0.9687	-0.9805	-0.9561	-0.9839	-0.1345
Phase angle	Error	G165.62	D168.67	G162.96	D169.72	D97.73
Voltage Harmonic Distortion	-------	1.081	0.772	1.044	1.666	-------
Current Harmonic Distortion	-------	2.854	5.163	4.311	2.308	-------

Figure 4.25: Super synchronous numeric data for N=1700rpm and P=300w of DFIG WECS

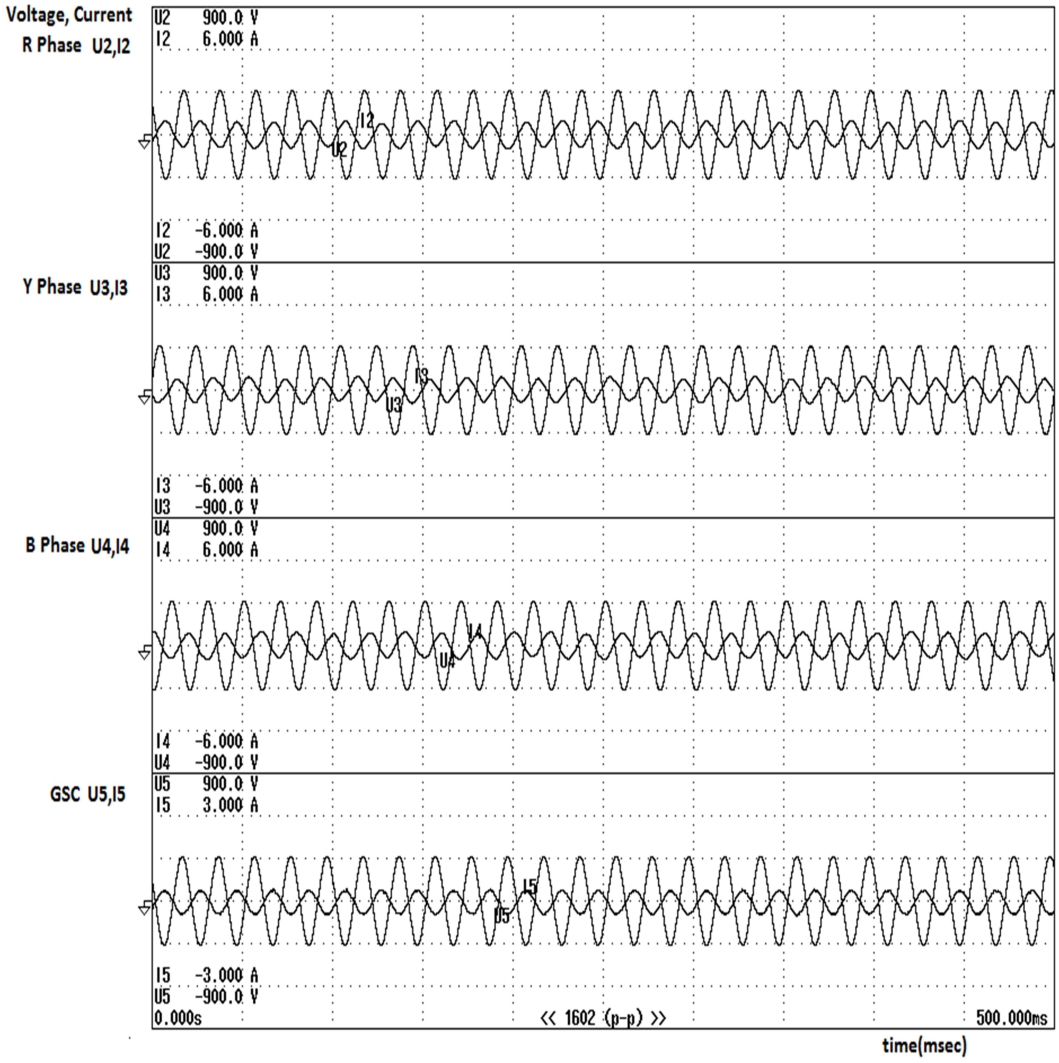

Figure 4.26: Supersynchronous waveform analysis for N=1700rpm and P=300w of DFIG WECS

4.10.2 Super synchronous mode for N=1700 rpm and P=450 w of DFIG WECS

Fig.4.27 and Fig.4.28 show the numeric data and waveform analysis for supesynchronous operation mode with speed set at N=1700rpm and active power set at P=450w of DFIG WECS. In supersynchronous mode, actual speed is greater than than the rated speed(1500rpm) of the slip ring motor. From Fig.4.27, open circuit voltage is defined where current is zero and open circuit voltage is 81.61V. Since current is zero, active power, apparent power and reactive power are zero. Power factor and phase angle are observed as errors, since phase angle will not exist if current is zero.

R phase, Y phase and B phase voltages are set at 220.24V, 225.10V and 223.19V respectively. Current flowing in 3 phases are observed as 0.72A, 0.67A, 0.76A respectively. From waveform analysis in Fig.4.28, it is observed that angle in between (U2,I2), (U3,I3), (U4,I4) are out of phase which signifies that active power is generated in all the three phases on stator side and the active powers generated are negative as shown in numerical data of Fig.4.27.

GSC and RSC are voltages are set at 220.86V and 116.27V. Since coupling transformer of 2:1 ratio is used on rotor side, rotor side voltage is approximately half of the stator and grid side voltages. From waveform analysis of Fig.4.28, it is observed that angle in between (U5,I5)is out of phase which signifies that active power is generated on rotor side and the active power generated is indicted as negative value(-0.0744kW) as shown in numerical data of Fig.4.27. In subsynchronous mode, power factor on GSC is negative and phase angle is greater than 90 degrees, which implies that GSC will act as inverter and RSC will act as rectifier for feeding the power from rotor side to grid side. Rotor is generating and supplying the power(-0.0744kW) to the grid side(-0.0544kW) through power electronic converters. From Fig.4.27, it is observed that total voltage and current harmonic distortions are less than 5% according to the standard grid codes.

	Open Circuit	R phase	Y phase	B phase	GSC	RSC
Vrms	81.61	220.24	225.10	223.19	220.86	116.27
Irms	0.0000	0.7299	0.6724	0.7642	0.2474	3.2891
Active Power (P)	-0.0000k	-151.38	-143.65	-155.94	-54.42	-0.0744k
Apparent Power (S)	0.0000k	160.76	151.35	170.56	54.65	0.3824k
Reactive Power (Q)	0.0000k	54.11	47.68	69.09	-4.97	-0.3751k
Power Factor	Error	-0.9416	-0.9491	-0.9143	-0.9959	-0.1946
Phase angle	Error	G160.33	G161.64	G156.11	D174.79	D101.22
Voltage Harmonic Distortion	-------	0.906	0.610	0.806	1.331	-------
Current Harmonic Distortion	-------	2.036	3.448	3.251	2.127	-------

Figure 4.27: Super synchronous numeric data for N=1700rpm and P=450w of DFIG WECS

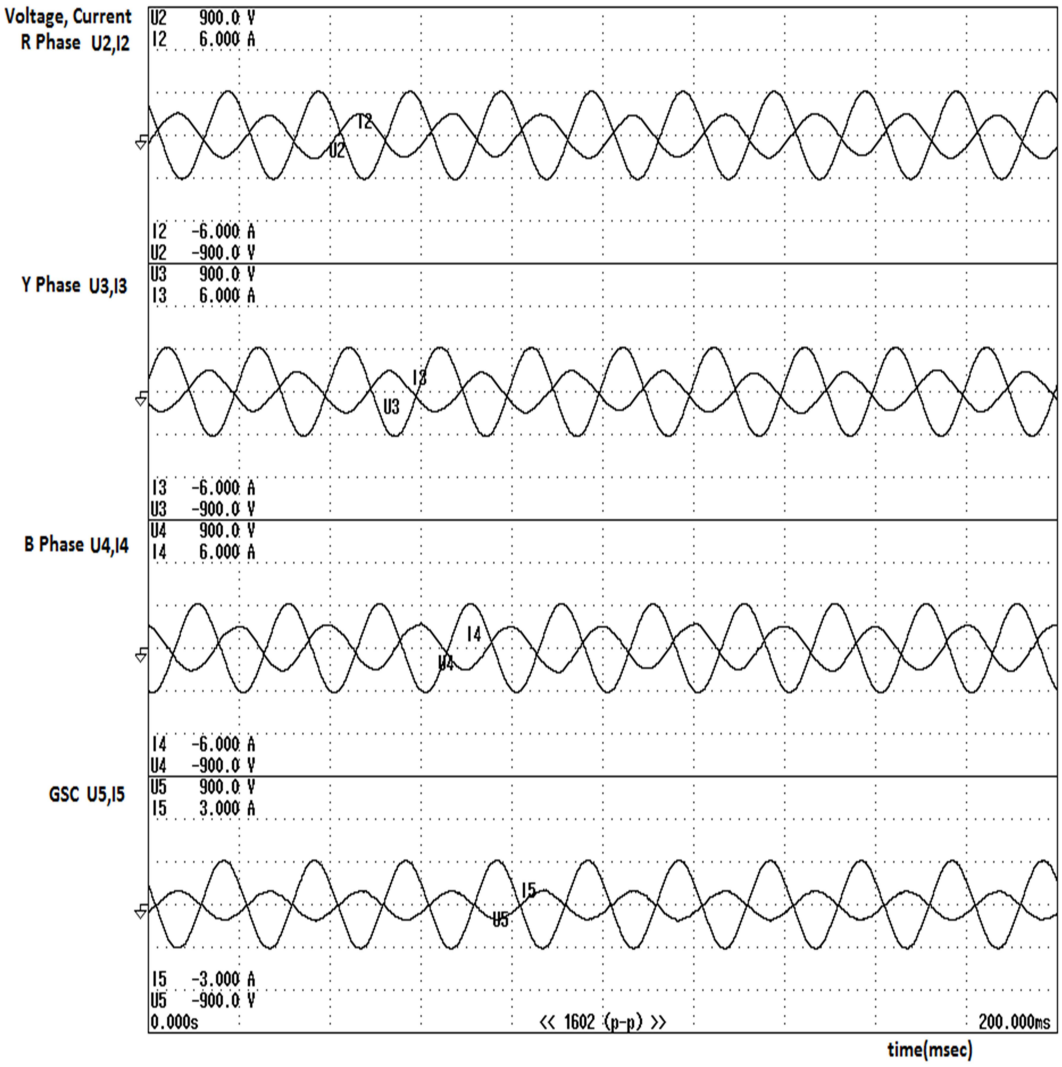

Figure 4.28: Supersynchronous waveform analysis for N=1700rpm and P=450w of DFIG WECS

4.11 Chapter Summary

In this chapter, a new control scheme namely LQR-OPC scheme has been presented for DFIG WECS, in which the performance index has been selected and by adjusting the weighing factors for control input, the actual rotor currents approached the desired reference currents with zero steady state error. It has been observed that SVOC does not require any estimator like FOC, since measured stator voltage is the only variable considered for rotor current control loop dynamics. From results, it has been observed that, stator active and reactive power are controlled by rotor q-axis current and d-axis current respectively for a given stator voltage using stator voltage oriented control. Faster current control dynamics for DFIG are achieved by adjusting the weighing factors in performance index. Feedforward compensation has also been done for eliminating the cross coupling induced emf and emf induced due to stator flux of DFIG. A controller has also been designed for switching of VSC based on rotor current control outputs of LQROPC DFIG model. From the results obtained, it is observed that through application of the proposed controller, steady state stability and zero steady state error are achieved in face of transient disturbances. Simulation Results obtained show the effectiveness of the proposed LQROPC has been verified with experimental results and it is observed that harmonic content is very low according to grid codes.

Chapter 5

Active and Reactive Power Control of DFIG Wind Energy Conversion System with Sliding Mode Control

5.1 Introduction

In chapter 4, LQR OPC controller applied for active and reactive power control achieved the steady state stability and zero steady state error in face of transient disturbances, but robustness requirement is not achieved in DFIG WECS. In this chapter, stator active and reactive power has been controlled by using Sliding Mode Control. Robustness of SMC is verified with Lyapunov function. Chattering due to switching function is eliminated using low pass filter. Simulations have been pursued for controlling active and reactive power by SMC using MATLAB/ SIMULINK. Controlling active and reactive power plays a vital role for power transmission and distribution. A number of controllers such as DPC[86, 87, 88, 41, 89, 90, 91, 92], FOC, DTC, MPC,SMC[93, 94, 95, 96, 97, 98, 99, 100], H_∞ controllers have been proposed in literature. In [101], sliding surface is taken for first order or linear equation. Torque equation is nonlinear, so it is necessary to linearise the torque equation by reduced order dynamics. Partial load region is taken since optimization can be done in partial region only. Sliding surface $\sigma\left(\Omega_a, \Gamma_G\right)$ is in terms of high speed shaft Ω_a of generator and torque Γ_G of

the generator. Optimal operating point $\sigma\left(\Omega_{aopt}, \Gamma_{Gopt}\right)$ is obtained depending on the wind speed.

In [35], two DPCs has been considered for DFIG and GSC separately. DPC for DFIG for eliminating torque & reactive power pulsations and DPC for GSC to compensate for the pulsations of stator active power. Under unbalanced grid supply, stator voltage of DFIG are splitted into positive and negative components and unbalanced control methods are considered based on symmetrical component theory.

In [30],Integral sliding Mode direct torque of DFIG under unbalanced grid voltage has been proposed. Grid voltage unbalance may be caused by unbalanced transmission line impedance, unbalanced loads and large single phase load. Because of parameter dependence of vector control, DPC and DTC has been proposed as alternatives to vector control. In this paper, two objectives hav been achieved, one is to regulate torque and stator reactive power independently and the other is to minimize ripples in torque and stator reactive power. For achieving these objectives, three controllers have been developed (i) positive and negative sequence torque and reactive power $T_e^+, T_e^-, Q_s^+, Q_s^-$. (ii)positive sequence controller for T_e^+, Q_s^-. (iii)sliding mode controller for T_e^+, Q_s^-, i.e., S_{Te}^+ & S_{Qs}^-. Sliding mode controller controls the system state on the predefined sliding surface on the system state space by adaptively changing the structure of the controller. Hence the system response depends only on the sliding surface and is insensitive to variations of system parameters and external disturbances.

In [102],sliding mode DPC is used for regulating active and reactive powers in the stationary reference frame. Under network unbalance, stator voltages and currents are divided into positive and negative sequence components. The stator output active power oscillations are cancelled because of negative sequence component. Therefore errors of stator output active power and reactive power are selected as sliding surfaces.

When the trajectory of the active and reactive power coincides with the sliding surface, then the steady state error will be cancelled.

In [37], DPC,VSC and SVM are combined for controlling the stator side active and reactive power by selecting voltage vectors from look up table. DPC method directly controls the stator side active and reactive power by selecting voltage vector from look up table using the

information about the active and reactive powers of the stator. The proposed VSC controller are two different sliding surfaces for active and reactive power control. The main problem in DPC is that it does not consider system uncertainties in DFIG. So VSC is proposed for avoiding this problem. In VSC, error dynamics for active and reactive power are bounded for reaching the sliding surfaces.

5.1.1 Chapter Objectives

- To design a robust nonlinear controller for controlling active and reactive power on stator side connected to grid.
- To verify the robustness of the controller in face of parametric uncertainities such as DFIG system parameters, power converter losses.
- To device a mechanism for reducing the chattering.

5.2 Modelling of stator active and reactive power of DFIG

From (4.2), stator current I_s can be written as

$$I_s = I_{dqs} = \left[\left(\frac{1}{L_\sigma L_{ss}}\right)\left(\psi_{dqs} - \frac{L_{mi}}{L_{rr}}\psi_{dqr}\right)\right] \tag{5.1}$$

From (4.1), u_s can be obtained as

$$u_s = u_{dqs} = u_{ds} + ju_{qs} = R_s I_{dqs} + \frac{d}{dt}\psi_{dqs} + j\omega_s\psi_{dqs} \tag{5.2}$$

Neglecting the stator resistance(negligible) and assuming the stator flux as constant, (5.2) can be rewritten as

$$u_s = u_{dqs} = \underbrace{R_s I_{dqs}}_{0} + \underbrace{\frac{d}{dt}\psi_{dqs}}_{0} + j\omega_s\psi_{dqs} \tag{5.3}$$

$\frac{d}{dt}\psi_{dqs} = 0$, since ψ_{dqs} is constant.

$$\begin{aligned} u_s &= j\omega_s\psi_{dqs} \\ u_{ds} + ju_{qs} &= j\omega_s\left(\psi_{ds} + j\psi_{qs}\right) \\ &= j\omega_s\psi_{ds} - \omega_s\psi_{qs} \end{aligned} \tag{5.4}$$

From Fig.4.2, in SVOC, orienting the d axis along the synchronous reference frame, $u_{ds} = u_s,\ u_{qs} = 0$

$$u_{ds} + j0 = j\omega_s\psi_{ds} - \omega_s\psi_{qs} \tag{5.5}$$

Comparing real and imaginary parts of (5.5) gives

$$\begin{aligned} u_{ds} &= -\omega_s\psi_{qs} \\ \psi_{qs} &= -\tfrac{u_{ds}}{\omega_s},\ \ \psi_{ds} = 0 \end{aligned} \tag{5.6}$$

Stator apparent power is given by

$$S_s = P_s + jQ_s = -\frac{3}{2}u_{ds}\left[\underbrace{\left(\frac{1}{L_\sigma L_{ss}}\right)\left(\psi_{dqs} - \frac{L_{mi}}{L_{rr}}\psi_{dqr}\right)}_{I_s}\right] \tag{5.7}$$

$$S_s = P_s + jQ_s = -\frac{3}{2}u_{ds}\left[\left(\frac{1}{L_\sigma L_{ss}}\right)\left(\left(\psi_{ds} + j\psi_{qs}\right) - \frac{L_{mi}}{L_{rr}}\left(\psi_{dr} + j\psi_{qr}\right)\right)\right] \tag{5.8}$$

$$S_s = P_s + jQ_s = -\frac{3}{2}u_{ds}\left[\left(\frac{1}{L_\sigma L_{ss}}\right)\left(\left(\underbrace{\psi_{ds}}_{0} + j\ \underbrace{\psi_{qs}}_{\psi_{qs}=-\frac{u_{ds}}{\omega_s}}\right) - \frac{L_{mi}}{L_{rr}}\left(\psi_{dr} + j\psi_{qr}\right)\right)\right] \tag{5.9}$$

$$S_s = P_s + jQ_s = \left(\frac{3}{2L_\sigma L_{ss}}\frac{L_{mi}}{L_{rr}}u_{ds}\psi_{dr}\right) - j\left(\frac{3}{2L_\sigma L_{ss}}\frac{L_{mi}}{L_{rr}}u_{ds}\right)\left(\psi_{qr} + \frac{L_{rr}}{L_{mi}}\frac{u_{ds}}{\omega_s}\right) \tag{5.10}$$

Comparing real and imaginary parts of (5.10) gives

$$\begin{aligned} P_s &= \left(\frac{3}{2L_\sigma L_{ss}}\frac{L_{mi}}{L_{rr}}u_{ds}\psi_{dr}\right) = \sigma u_{ds}\psi_{dr} \\ Q_s &= -\frac{3}{2L_\sigma L_{ss}}\frac{L_{mi}}{L_{rr}}u_{ds}\left(\psi_{qr} + \frac{L_{rr}}{L_{mi}}\frac{u_{ds}}{\omega_s}\right) = -\sigma u_{ds}\left(\psi_{qr} + \frac{L_{rr}}{L_{mi}}\frac{u_{ds}}{\omega_s}\right) \end{aligned} \tag{5.11}$$

where $\sigma = \frac{3}{2L_\sigma L_{ss}}\frac{L_{mi}}{L_{rr}}$

From (5.11), one obtains

$$\psi_{dr} = \frac{P_s}{\sigma u_{ds}}, \;\; \psi_{qr} = -\frac{Q_s}{\sigma u_{ds}} - \frac{L_{rr}}{L_{mi}} \frac{u_{ds}}{\omega_s} \tag{5.12}$$

5.3 Design of SMC for active and reactive power control

The switching variables are chosen as

$$\begin{aligned} S_{P_s} &= e_{P_s} + c_{p_s} \int e_{P_s} dt \\ S_{Q_s} &= e_{Q_s} + c_{q_s} \int e_{Q_s} dt \end{aligned} \tag{5.13}$$

$$\begin{aligned} e_{P_s} &= P_s^* - P_s \\ e_{Q_s} &= Q_s^* - Q_s \end{aligned} \tag{5.14}$$

where S_{P_s} and S_{Q_s} are the sliding surfaces for stator active and reactive power, e_{P_s} and e_{Q_s} are the errors of stator active and reactive power, P_s^* and Q_s^* are the reference values of stator active and reactive power.

From (5.13), time derivative of the sliding surfaces can be expressed as

$$\begin{aligned} \dot{S}_{P_s} &= \left(\dot{P}_s^* - \dot{P}_s\right) + c_{p_s}\left(P_s^* - P_s\right) = \left(\dot{P}_s^* - P_s\right) + c_{p_s} e_{P_s} \\ \dot{S}_{Q_s} &= \left(\dot{Q}_s^* - \dot{Q}_s\right) + c_{q_s} \int \left(Q_s^* - Q_s\right) dt = \left(\dot{Q}_s^* - \dot{Q}_s\right) + c_{q_s} e_{Q_s} \end{aligned} \tag{5.15}$$

$$\begin{aligned} \dot{P}_s = \frac{dP_s}{dt} &= \sigma u_{ds} \frac{d\psi_{dr}}{dt} \\ &= \sigma u_{ds}\left(u_{dr} - R_r I_{dr} + \omega_{sl}\psi_{qr}\right) \\ &= \sigma u_{ds}\left(u_{dr} - 0 + \omega_{sl}\psi_{qr}\right) \\ &= \sigma u_{ds} u_{dr} + \sigma u_{ds}\omega_{sl}\psi_{qr} \\ &= \sigma u_{ds} u_{dr} + \sigma u_{ds}\omega_{sl}\left(-\frac{Q_s}{\sigma u_{ds}} - \frac{L_{rr}}{L_{mi}}\frac{u_{ds}}{\omega_s}\right) \end{aligned} \tag{5.16}$$

$$\begin{aligned} \dot{S}_{P_s} &= \left(\dot{P}_s^* - \sigma u_{ds} u_{dr} + \sigma u_{ds}\omega_{sl}\left(-\frac{Q_s}{\sigma u_{ds}} - \frac{L_{rr}}{L_{mi}}\frac{u_{ds}}{\omega_s}\right)\right) + c_{p_s} e_{P_s} \\ f_{P_s} &= f_1\left(u_{ds}, \omega_{sl}, \omega_s, Q_s, c_{p_s}, e_{P_s}, \dot{P}_s^*\right) \\ \dot{S}_{P_s} &= f_{P_s} - \sigma u_{ds}\left[u_{dr}\right] \end{aligned} \tag{5.17}$$

$$\begin{aligned}\dot{Q}_s = \frac{dQ_s}{dt} &= \frac{d}{dt}\left[-\sigma u_{ds}\left(\psi_{qr} + \frac{L_{rr}}{L_{mi}}\frac{u_{ds}}{\omega_s}\right)\right] = -\sigma u_{ds}\frac{d\psi_{qr}}{dt} + 0 \\ &= -\sigma u_{ds}u_{qr} + \sigma u_{ds}\omega_{sl}\left(\frac{P_s}{\sigma u_{ds}}\right) \\ &= -\sigma u_{ds}u_{qr} + \omega_{sl}P_s\end{aligned} \tag{5.18}$$

$$\begin{aligned}\dot{S}_{Q_s} &= \left(\dot{Q}_s^* - \dot{Q}_s\right) + c_{q_s}e_{Q_s} \\ &= \dot{Q}_s^* - (-\sigma u_{ds}u_{qr} + \omega_{sl}P_s) + c_{q_s}e_{Q_s} \\ &= \dot{Q}_s^* + \sigma u_{ds}u_{qr} - \omega_{sl}P_s + c_{q_s}e_{Q_s} \\ f_{Q_s} &= f_2\left(u_{ds}, \omega_{sl}, P_s, c_{q_s}, e_{Q_s}, \dot{Q}_s^*\right) \\ \dot{S}_{Q_s} &= f_{Q_s} + \sigma u_{ds}\left[u_{qr}\right]\end{aligned} \tag{5.19}$$

From (5.17) and (5.19), one can write

$$\begin{bmatrix} \dot{S}_{P_s} \\ \dot{S}_{Q_s} \end{bmatrix} = \underbrace{\begin{bmatrix} f_{P_s} \\ f_{Q_s} \end{bmatrix}}_{F_{P_sQ_s}} - \sigma \underbrace{\begin{bmatrix} u_{ds} & 0 \\ 0 & -u_{ds} \end{bmatrix}}_{H} \begin{bmatrix} u_{dr} \\ u_{qr} \end{bmatrix} \tag{5.20}$$

Let the equivalent control signals are assumed as

$$\begin{bmatrix} u_{dr_{eq}} \\ u_{qr_{eq}} \end{bmatrix} = \frac{H^{-1}}{\sigma} F_{P_sQ_s} \tag{5.21}$$

Substituting (5.21) in (5.20) yields

$$\begin{aligned}\dot{S}_{P_s} = 0 &= \dot{e}_{P_s} + c_{p_s}e_{P_s} \\ \dot{S}_{Q_s} = 0 &= \dot{e}_{Q_s} + c_{q_s}e_{Q_s}\end{aligned} \tag{5.22}$$

Equation (5.22) denotes that the errors in the control variables tend to zero. However, the control signals defined in (5.21) depends highly on DFIG parameters. To compensate deviations due to DFIG system parameters, a second term is introduced in the control signals of (5.22) as

$$\begin{aligned} u_{dr} &= u_{dr_{eq}} + u_{dr_c} \\ u_{qr} &= u_{qr_{eq}} + u_{qr_c} \end{aligned} \tag{5.23}$$

Fig.5.1 shows the active and reactive power control using sliding mode controller. In SMC,

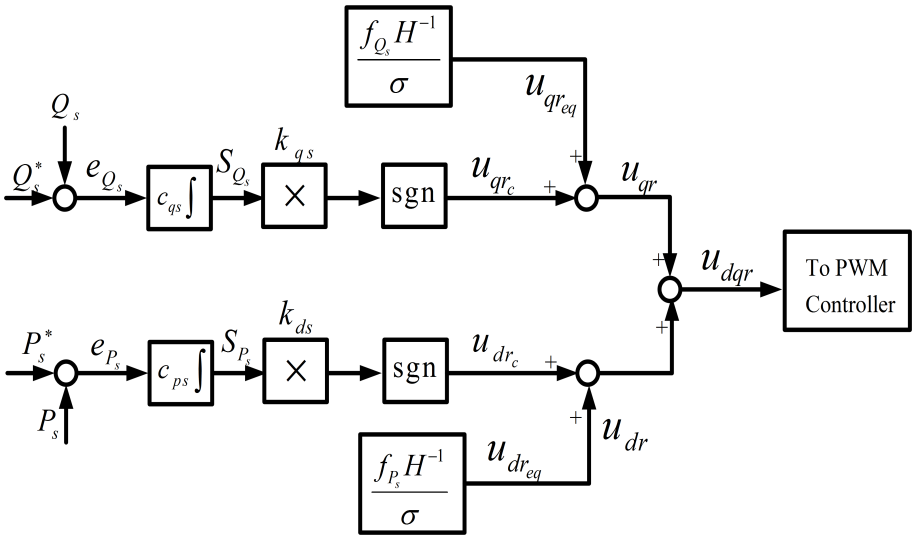

Figure 5.1: Sliding mode controller design for DFIG WECS

stator active and reactive power are compared with the reference values and the error obtained is given to integrator along with constant c_p and c_q. The outputs are the sliding surfaces S_{P_s} and S_{Q_s} respectively. These sliding surfaces are multiplied with k_{ps} and k_{qs} along with discontinuity functions to obtain u_{dr_c} and u_{qr_c} respectively. From equations (5.17) and (5.19), $u_{dr_{eq}}$ and $u_{qr_{eq}}$ are obtained. Finally eq.(5.23) is obtained as shown in Fig.5.1. These control variables obtained from SMC controller are used for PWM switching of converters.

$$\begin{bmatrix} u_{dr_c} \\ u_{qr_c} \end{bmatrix} = H^{-1} \underbrace{\begin{bmatrix} k_{p_s} & 0 \\ 0 & k_{q_s} \end{bmatrix} \begin{bmatrix} \text{sgn}(S_{P_s}) \\ \text{sgn}(S_{Q_s}) \end{bmatrix}}_{u_{PQ_1}} \tag{5.24}$$

where $u_{PQ1} = \begin{bmatrix} u_{P_1} \\ u_{Q_1} \end{bmatrix}$

Equation (5.20) can be rewritten so that d_{r1} and d_{r2} are added as uncertainties. compensation variables u_{dr_c} and u_{qr_c} are considered, which yields

$$\begin{bmatrix} \dot{S}_{P_s} \\ \dot{S}_{Q_s} \end{bmatrix} = \begin{bmatrix} f_{P_s} \\ f_{Q_s} \end{bmatrix} - \sigma \begin{bmatrix} u_{ds} & 0 \\ 0 & -u_{ds} \end{bmatrix} \begin{bmatrix} u_{dr} \\ u_{qr} \end{bmatrix} + \begin{bmatrix} d_{r1} \\ d_{r2} \end{bmatrix} \tag{5.25}$$

Replacing (5.21),(5.23) and (5.24) in (5.25) yields

$$\begin{bmatrix} \dot{S}_{P_s} \\ \dot{S}_{Q_s} \end{bmatrix} = -\sigma \begin{bmatrix} k_{p_s} & 0 \\ 0 & k_{q_s} \end{bmatrix} \begin{bmatrix} \text{sgn}(S_{P_s}) \\ \text{sgn}(S_{Q_s}) \end{bmatrix} + \begin{bmatrix} d_{r1} \\ d_{r2} \end{bmatrix} \tag{5.26}$$

5.4 Robustness verification using Lyapunov theory

In order to verify that (5.21),(5.23) and (5.24) lead the switching variables to converge to zero, the following Lyapunov function is chosen as

$$V = \frac{1}{2} S_{P_s Q_s}^T S_{P_s Q_s} \geq 0 \tag{5.27}$$

For converge, its derivative must be negative, that is

$$\dot{V} = S_{P_s Q_s}^T \dot{S}_{P_s Q_s} \leq 0 \tag{5.28}$$

Substituting (5.26) in (5.28) yields

$$\dot{V} = S_{P_s} \sigma k_{p_s} \text{sgn}(S_{P_s}) + S_{P_s} d_{r1} - S_{Q_s} \sigma k_{q_s} \text{sgn}(S_{Q_s}) + S_{Q_s} d_{r2} \leq 0 \tag{5.29}$$

In equation (5.29) , control variables converge to zero, if

$$k_{p_s} \gg \frac{|d_{r1}|}{\sigma}, \quad k_{q_s} \gg \frac{|d_{r2}|}{\sigma} \tag{5.30}$$

The second term of control signal in (5.24) is discontinuous due to sgn function. To obtain a continuous signal, u_{PQ1} in (5.24) is passed through low pass filter(LPF). Now, equation (5.24) can be modified as follows

$$\begin{bmatrix} u_{dr_c} \\ u_{qr_c} \end{bmatrix} = H^{-1} u_{PQ_{av}} \tag{5.31}$$

$$u_{PQ_{av}} = \begin{bmatrix} u_{P_{av}} \\ u_{Q_{av}} \end{bmatrix}$$
$$u_{P_{av}}(s) = \frac{1}{1+sT} u_{P1}(s),\ u_{Q_{av}}(s) = \frac{1}{1+sT} u_{Q1}(s) \tag{5.32}$$

where T denotes the time constant of the LPF. Thus, the discontinuous signals u_{P1} and u_{Q1} become only part of the internal process and the control variables are finally continuous. From equations (5.21),(5.23) and (5.31), the expression of the active and reactive power control signal is given by

$$\begin{bmatrix} u_{dr_c} \\ u_{qr_c} \end{bmatrix} = \frac{H^{-1}}{\sigma} F_{P_s Q_s} + H^{-1} u_{PQ_{av}} \tag{5.33}$$

The second term in (5.33) makes the active and reactive power control system robust, which is independent of DFIG parameters.

5.5 Results and Discussion

A 2 kW DFIG coupled to wind turbine is simulated using MATLAB/SIMULINK. Simulation parameters are given in Table 4.3. For simulation, wind speed is set constant at 12m/sec. Due to voltage dip on the stator side, transients are observed from 3 to 6.2 sec as shown in Fig. 5.2. Therefore current is rising abnormally at 3 sec. By adjusting the sliding mode parameter values, the current is settling to steady value after 6.2 sec as shown in Fig. 5.3. The value of sliding surface coefficients c_{ps} and c_{qs} are chosen as 2 and 1.8 respectively. To determine the switching control, the bounds of parametric uncertainties are taken as

$$0.5\ L_{mi} \leq L_{mi} \leq 1.5 L_{mi}$$
$$0.5\ L_s \leq L_s \leq 1.5 L_s$$
$$0.5\ L_r \leq L_r \leq 1.5 L_r$$

Under these assumptions and according to eq.(5.30), the constants k_{ps}=52 and k_{qs}=75.8 in (5.24) are taken large so that the ripples in active and reactive power are reduced effectively and reaches to steady state. In Fig. 5.4,active power obtained is 223W at 3 sec, and ripples

are observed in active power from 3 sec to 6.2 sec due to unbalanced voltage. Similarly, ripples in reactive power has been reduced as shown in Fig. 5.5. The ripples are reduced by considering the large values for constants k_{ps} and k_{ps}. The DC link voltage is maintained constant at 200V at steady state after 6.2 sec. The rotor speed is fluctuating from 3 sec due to fall in voltage and after 70% rated speed is reached, rotor speed is coming to steady value as shown in Fig. 5.6. The main advantage of using SMC is chatering phenomenon is reduced both in active and reactive power. The robustness of DFIG WECS is verified by using Lyapunov theory.

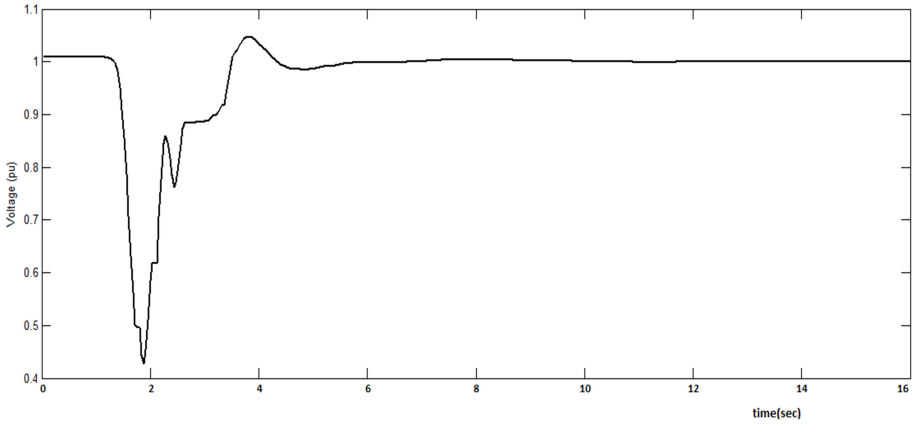

Figure 5.2: Stator voltage versus time

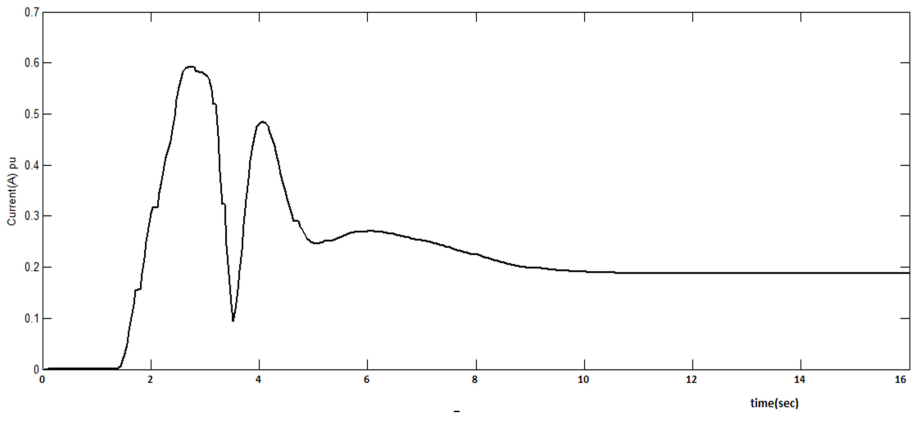

Figure 5.3: Stator current versus time

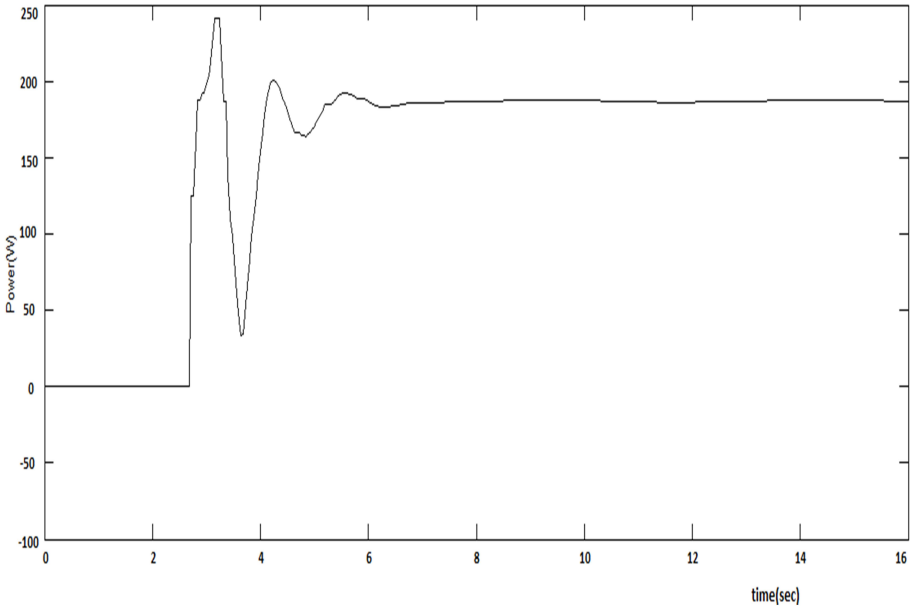

Figure 5.4: Active Power versus time

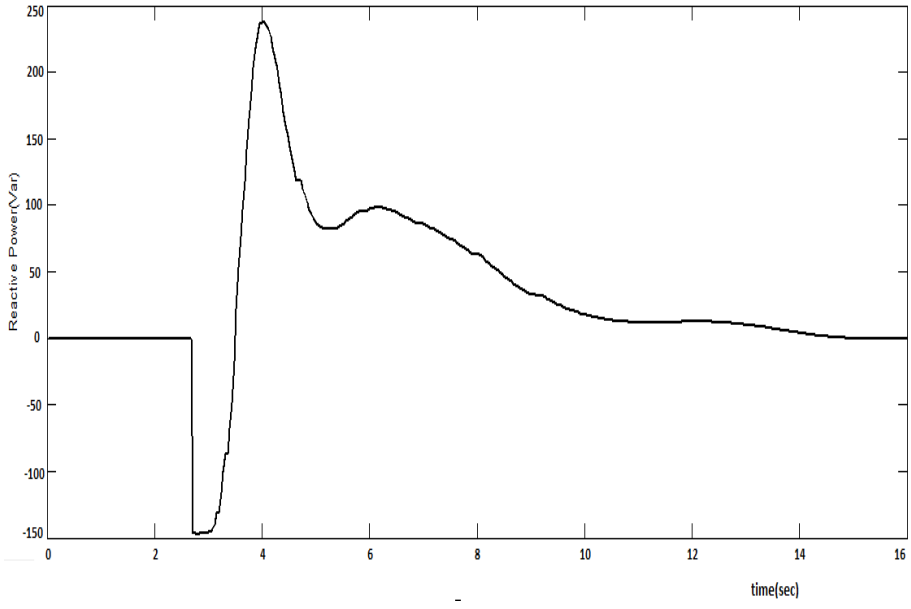

Figure 5.5: Reactive Power versus time

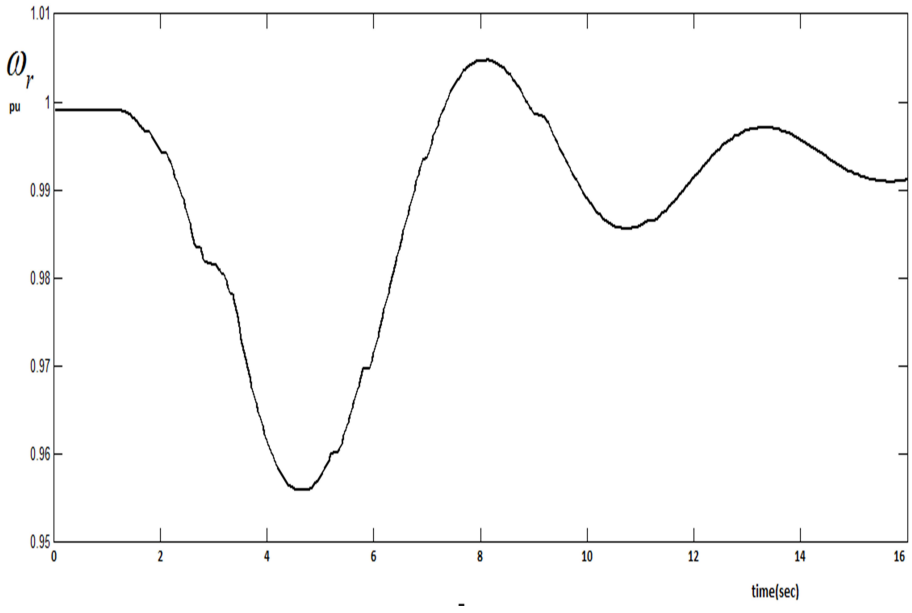

Figure 5.6: ω_r versus time

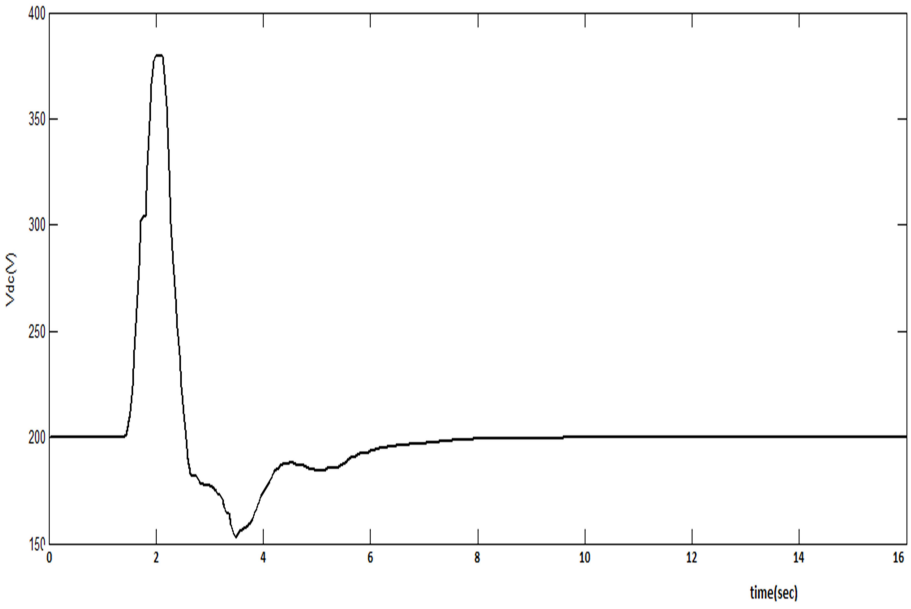

Figure 5.7: DC voltage versus time

5.5.1 Experiment Results

In super synchronous mode, stator and rotor feed power to grid and RSC will act as rectifier and GSC will act as inverter. Since rotor speed is above rated speed, rotor generates power which causes DC link voltage to increase. For operating in closed loop control, DC link voltage should be equal to set value. Because of change in DC link voltage, there is phase difference coming in between voltage and current. Due to phase difference, power is generated and fed to grid both from stator and rotor side. On GSC, PF and DC link voltage are regulated. Stator side voltage, grid side voltage and rotor side voltage are represented as shown in Table 5.1. Active power generated on stator side is -223.92W and on rotor side is -14.096W as shown in Fig.5.8 are negative which implies voltage and currents are out of phase as shown in waveform of Fig.5.9. Stator and rotor are generating power and feeding to grid, but grid side active power is 16.28W indicating the positive value, which signifies that voltage and current are in phase and is absorbing power.

Table 5.1: Descriptions of the parameters for figures Fig.5.8

Vrms[V]	Stator side voltage	Grid side voltage	Rotor side voltage
Irms[A]	Stator side current	Grid side current	Rotor side current
Active power P(W)	Stator side Active power	Grid side Active power	Rotor side Active power
Apparent power S(VA)	Stator side Apparent power	Grid side Apparent power	Rotor side Apparent power
Reactive power Q(Var)	Stator side Reactive power	Grid side Reactive power	Rotor side Reactive power
Power Factor(pf)	Stator side pf	Grid side pf	Rotor side pf
Phase angle(ϕ)	Stator side ϕ	Grid side ϕ	Rotor side ϕ

	Stator side	Grid side	Rotor side
Vrms	243.48	36.18	114.07
Irms	0.9716	1.5071	132.49
Active Power (P)	-223.92	16.28	-14.096
Apparent Power (S)	236.56	54.53	15.114
Reactive Power (Q)	76.29	-52.04	5.454
Power Factor	-0.9466	0.2986	-0.9326
Phase angle	G161.19	D72.63	G158.85

Figure 5.8: Numeric data for N=1700 rpm and P=300 w of DFIG WECS

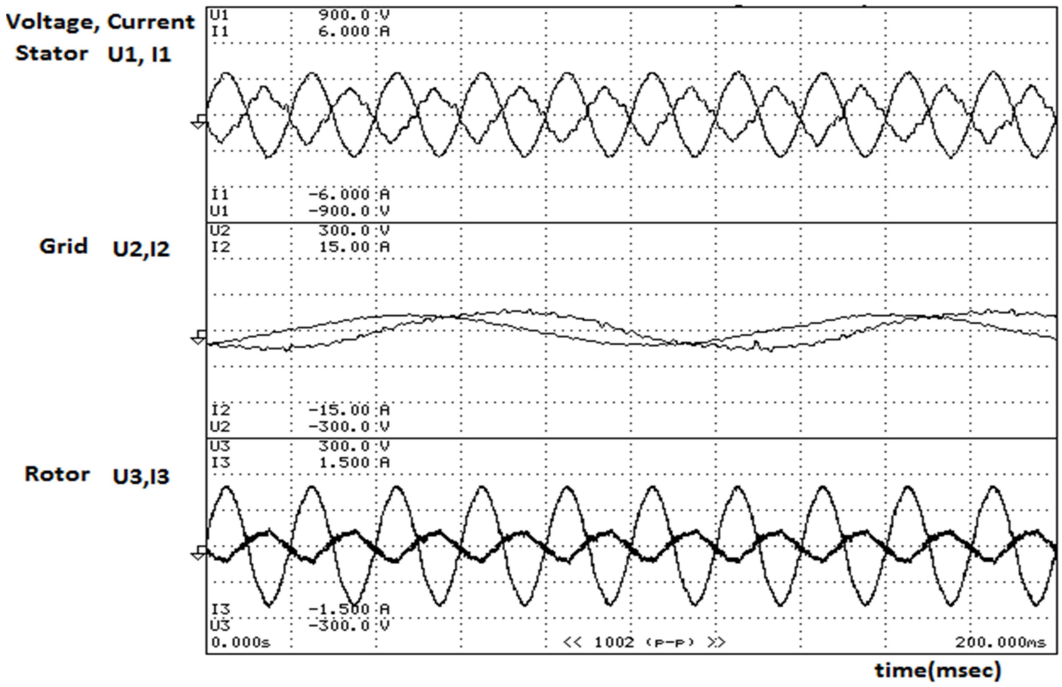

Figure 5.9: Waveform data for N=1700 rpm and P=300 w of DFIG WECS

5.6 Comparative analysis of SMCFOC, SMCDPC and LQROPC

5.6.1 Sub synchronous mode

Table 5.2: Descriptions of the parameters for figures Fig.5.10,5.11,5.12,5.13,5.14,5.15

Parameter	Rotor R-Phase (RRP)	Rotor Y-Phase (RYP)	Rotor B-Phase (RBP)	Stator R-Phase (SRP)	Stator Y-Phase (SYP)	Stator B-Phase (SBP)
Vrms[V]	RRP voltage	RYP voltage	RBP voltage	SRP voltage	SYP voltage	SBP voltage
Irms[A]	RRP current	RYP current	RBP current	SRP current	SYP current	SBP current
Active power P(W)	RRP power	RYP power	RBP power	SRP power	SYP power	SBP power
Apparent power S(VA)	RRP power	RYP power	RBP power	SRP power	SYP power	SBP power
Reactive power Q(Var)	RRP power	RYP power	RBP power	SRP power	SYP power	SBP power
Power Factor(pf) λ	RRP pf	RYP pf	RBP pf	SRP pf	SYP pf	SBP pf
Phase angle(ϕ)	RRP ϕ	RYP ϕ	RBP ϕ	SRP ϕ	SYP ϕ	SBP ϕ

In Fig.5.10,5.11,5.12, FOC, DPC and LQROPC algorithms are compared for various stator and rotor parameters listed in Table 5.2 for sub synchronous mode for N=1300 rpm and by setting P=300 w. Numeric data is considered for comparision as shown in Table 5.2. Results in sub synchronous mode shows that, LQROPC control is better compared to SMCFOC and SMCDPC. Element1,2,3 represents rotor R,Y,B phase parameters and Element 4,5,6 represents stator R,Y,B phase parameters. In sub synchronous mode stator and grid are in phase and grid supplies power to rotor. Rotor is absorbing power and the values of P are positive. In FOC,DTC and LQROPC, the active power fed from grid to rotor are 134.2

w, 133.3 w and 150.7 w respectively. Hence, it is observed from Fig.5.10,5.11,5.12 that grid is supplying more active power to rotor in LQROPC compared to FOC and DTC.

	Rotor R phase (RRP)	Rotor Y phase (RYP)	Rotor B phase (RBP)	Stator R phase (SRP)	Stator Y phase (SYP)	Stator B phase (SBP)
Vrms	89.38	163.56	162.86	152.82	154.12	156.55
Irms	2.8677	2.6049	2.5446	1.0753	1.0303	0.9042
Active Power (P)	0.1463k	0.1342k	0.1279k	-0.1637k	-0.1578k	-0.1403k
Apparent Power (S)	0.2302k	0.3436k	0.3316k	0.1630k	0.1576k	0.1398k
Reactive Power(Q)	0.1777k	0.3163k	0.3060k	0.0000k	0.0000k	0.0000k
Power Factor	0.6355	0.3907	0.3858	-1.0000	-1.0000	-1.0000
Phase angle	G50.54	G67.00	G67.31	D180.00	D180.00	D180.00

Figure 5.10: FOC control of Stator and rotor parameters for Subsynchronous mode N=1300rpm and P=300w of DFIG WECS

	Rotor R phase (RRP)	Rotor Y phase (RYP)	Rotor B phase (RBP)	Stator R phase (SRP)	Stator Y phase (SYP)	Stator B phase (SBP)
Vrms	95.98	161.26	161.36	209.99	212.20	215.52
Irms	2.8242	2.5185	2.4700	1.2670	1.3130	1.1095
Active Power (P)	0.1498k	0.1333k	0.1308k	-0.2015k	-0.1859k	-0.1327k
Apparent Power (S)	0.2456k	0.3366k	0.3262k	0.2578k	0.2729k	0.2351k
Reactive Power(Q)	0.1946k	0.3091k	0.2989k	0.1609k	0.1998k	0.1941k
Power Factor	0.6099	0.3961	0.4008	-0.7815	-0.6812	-0.5645
Phase angle	G52.41	G66.67	G66.37	G141.40	G132.94	G124.37

Figure 5.11: DTC control of Stator and rotor parameters for Subsynchronous mode N=1300rpm and P=300w of DFIG WECS

	Rotor R phase (RRP)	Rotor Y phase (RYP)	Rotor B phase (RBP)	Stator R phase (SRP)	Stator Y phase (SYP)	Stator B phase (SBP)
Vrms	99.69	163.52	163.19	210.06	213.54	216.42
Irms	3.2467	2.9019	2.8699	1.2490	1.2166	1.0070
Active Power (P)	0.1689k	0.1507k	0.1495k	-0.2164k	-0.1898k	-0.1461k
Apparent Power (S)	0.2944k	0.3989k	0.3891k	0.2526k	0.2525k	0.2107k
Reactive Power(Q)	0.2412k	0.3694k	0.3592k	0.1303k	0.1666k	0.1519k
Power Factor	0.5737	0.3777	0.3842	-0.8566	-0.7516	-0.6931
Phase angle	G54.99	G67.81	G67.40	G148.94	G138.73	G133.88

Figure 5.12: LQROPC control of Stator and rotor parameters for Subsynchronous mode N=1300rpm and P=300w of DFIG WECS

5.6.2 Super synchronous mode

Fig.5.13,5.14,5.15 are compared for various stator and rotor parameters for super synchronous mode for N=1700 rpm and by setting P=300 w. Numeric data is considered for comparision as shown in Table 5.2. In super synchronous mode both rotor and stator supplies power to grid. Phase difference(out of phase) is observed between volage and current of both the stator and rotor. Therefore, rotor and stator generate power which is fed to the grid. Rotor is delivering power and the values of active power P are negative. In FOC,DTC and LQROPC, the active power fed from grid to rotor are -105.54 w, -100.9 w and -108.41 w respectively. Negative sign indicates power is generated.It is observed from Fig.5.13,5.14,5.15 that rotor active power is more generated and delivered to grid in LQROPC compared to SMCFOC and SMCDPC.

	Rotor R phase (RRP)	Rotor Y phase (RYP)	Rotor B phase (RBP)	Stator R phase (SRP)	Stator Y phase (SYP)	Stator B phase (SBP)
Vrms	206.03	206.60	208.85	99.86	98.96	99.09
Irms	0.5178	0.5175	0.4973	3.150	3.203	3.188
Active Power (P)	-105.44	-105.54	-103.40	-0.0813k	-0.0833k	-0.0763k
Apparent Power (S)	107.34	106.66	104.24	0.3135k	0.3153k	0.3144k
Reactive Power (Q)	20.09	15.45	-13.20	-0.3027k	-0.3041k	-0.3050k
Power Factor	-0.9823	-0.9894	-0.9919	-0.2594	-0.2641	-0.2427
Phase angle	G169.21	G171.67	D172.72	D105.04	D105.31	D104.05

Figure 5.13: FOC control of Stator and rotor parameters for Super synchronous mode N=1700 rpm and P=300 w of DFIG WECS

	Rotor R phase (RRP)	Rotor Y phase (RYP)	Rotor B phase (RBP)	Stator R phase (SRP)	Stator Y phase (SYP)	Stator B phase (SBP)
Vrms	205.00	205.80	208.34	99.06	98.34	98.52
Irms	0.4945	0.4853	0.4668	3.184	3.231	3.225
Active Power (P)	-100.90	-99.37	-96.88	-0.0781k	-0.0800k	-0.0733k
Apparent Power (S)	101.99	99.34	97.65	0.3143k	0.3161k	0.3163k
Reactive Power (Q)	-14.83	0.00	-12.26	-0.3044k	-0.3059k	-0.3076k
Power Factor	-0.9894	-1.0000	-0.9921	-0.2486	-0.2530	-0.2317
Phase angle	D171.64	D180.00	D172.79	D104.39	D104.66	D103.40

Figure 5.14: DTC control of Stator and rotor parameters for Super synchronous mode N=1700 rpm and P=300 w of DFIG WECS

	Rotor R phase (RRP)	Rotor Y phase (RYP)	Rotor B phase (RBP)	Stator R phase (SRP)	Stator Y phase (SYP)	Stator B phase (SBP)
Vrms	205.80	205.41	208.39	96.55	95.73	95.81
Irms	0.5076	0.5347	0.5302	3.152	3.214	3.202
Active Power (P)	-103.92	-108.41	-110.35	-0.0938k	-0.0945k	-0.0871k
Apparent Power (S)	105.31	109.72	110.89	0.3028k	0.3063k	0.3052k
Reactive Power (Q)	-17.08	16.88	-10.96	-0.2879k	-0.2914k	-0.2925k
Power Factor	-0.9868	-0.9881	-0.9951	-0.3098	-0.3084	-0.2854
Phase angle	D170.66	G171.15	D174.33	D108.05	D107.96	D106.58

Figure 5.15: LQROPC control of Stator and rotor parameters for Super synchronous mode N=1700 rpm and P=300 w of DFIG WECS

5.7 Chapter Summary

In this chapter, in order to control both active and reactive powers of DFIG-WECS, a new SMC has been proposed with SVOC. The stator active and reactive power are controlled by considering the control variables as rotor voltages(quadrature and direct axis) respectively. Sliding surfaces has been selected for active and reactive power and the robustness of the dynamic switching variables has been verified using Lyapunov stability criterion. Simulations studies are pursued using MATLAB/SIMULINK and the results shown that active and reactive power have been controlled effectively around the reference value.

The proposed sliding mode controller has been implemented in real time on a 2 kW lab set up. Active,reactive power and various parameters like power factor and DC link voltage of DFIG WECS have been controlled through linear quadratic regulator optimal preview control and compared with sliding mode field oriented control and sliding mode direct power control. Both numeric and waveform analysis have been presented for performance analysis of the DFIG based WECS both for sub synchronous and super synchronous modes.

Chapter 6

Conclusions and Future Directions

6.1 Conclusions of the thesis

- An extensive literature review on active and reactive power control is presented in chapter 1. Controllers such as field oriented control, direct torque control, direct power control, rotor current control, model predictive control, linear parameter varying control has been studied. Different MPPT techniques for wind turbine has also been studied.

- In chapter 2, a sliding mode control has been developed for torque and pitch control of the DFIG based wind energy conversion system. After simulation and experimentations, it is observed that the proposed SMC provides efficient control performance for DFIG speed and power regulation compared to both linear parameter varying and proportional integral controllers in terms of steady state and transient responses with simpler controller structure.

- In chapter 3, in order to capture the nonlinear and time varying dynamics of variable speed variable pitch DFIG based WECS, a NARMAX model is identified on-line which is used subsequently to develop an adaptive controller for speed and power regulation of DFIG connected to wind turbine. Nonlinear model predictive controller (NAMPC) has been proposed for NARMAX identification model. The efficacy of the proposed NAMPC is verified by comparing its performance with that of PI and model predictive

controllers.

- Subsequently in chapter 4, an optimal controller is designed that is based on linear quadratic regulator optimal preview control (LQROPC) theory. A new performance index is formulated with weighting factors for control input. From the obtained results, it is seen that the the actual rotor currents approach the desired reference currents with zero steady state error. Faster current control dynamics for DFIG are achieved by adjusting the weighing factors in the aforesaid performance index. Simulation results show the effectiveness of the proposed LQR OPC controller by comparing its performance with that of sliding mode field oriented control and sliding mode direct power controllers.

- In chapter 5, stator active and reactive power are controlled by designing a sliding mode controller with new choices of the sliding surface. Simulations studies show that active and reactive power are controlled effectively close to the set reference values of active and reactive powers.

  The proposed SMC controller has been implemented on the experimental DFIG based WECS set up. Active, reactive power and various parameters like power factor and DC line voltage of DFIG based WECS has been controlled through LQROPC controller and compared with sliding mode field oriented control and sliding mode direct power controllers both in sub synchronous and super synchronous modes.

6.2 Contributions of the thesis

The following are the thesis contributions.

- A new sliding mode controller (SMC) has been developed for both the toque and pitch control of an wind turbine of the wind energy conversion system (WECS) in order to achieve robustness in face of external disturbances and chattering free response.

- A Nonlinear Auto-Regressive Moving Average Exogenous (NARMAX) model structure

is developed for identification of the nonlinear dynamics of the WECS which was found to be appropriate for real-time control of WECS.

- For the above NARMAX modeling of the WECS, an adaptive on-line Recursive Least Square (RLS) estimation algorithm has been employed for parameter estimation of a variable pitch variable speed wind turbine system.
- An Optimal Preview Control (OPC) scheme has been developed for active and reactive power control on stator side of the DFIG with feed-forward compensation.
- Stability analysis of the proposed control schemes were pursued and it was proved that the proposed controllers exhibit stable performances.
- For achieving effective active and reactive power control of the WECS, a robust sliding mode controller has been proposed.
- A composite co-ordination control scheme has been developed for wind-turbine plus DFIG based wind energy conversion system by employing the aforesaid OPC and SMC.

6.3 Suggestions for Future Work

- In the thesis, stator side unbalanced voltage conditions are considered for controlling active and reactive power. But the performance of the DFIG based WECS under unbalanced voltage conditions on grid side should be considered. For investigating this problem, impedance matching on grid side should also be taken into consideration.
- Low voltage ride through problem has to be investigated, since current increases drastically for low voltage dips on grid side. There are two main problems that must be overcome in achieving the ride through requirements of DFIG during the voltage dip. The first one is the peak rotor fault current that may exceed the rotor-side converter limit, and the second one is the dc-link overvoltage. The ride through control is triggered if the rotor current limit is 2 pu (per unit) and the dc-link voltage limit is 1.2 times its nominal value.

6.4 Thesis Dissemination

Journals

1. B.Subudhi and P.S.Ogeti, Sliding mode approach to torque and pitch control for an wind energy system using FPGA, Archives of Control Sciences, vol.22(LVIII),no.3, pp 285-302,2012.

2. B.Subudhi and P.S.Ogeti,"NARMAX model based Adaptive Control of a Wind Energy Conversion System", IET Journal of Engineering, doi no.10.1049/joe.2016.0081, pp 1-9, 2016.

3. B.Subudhi and P.S.Ogeti,"Optimal Preview Stator Oriented Control of DFIG Wind Energy Conversion System", IET Generation, Transmission and Distribution (Revised copy submitted Under Review)

Conferences

1. B.Subudhi and P.S.Ogeti, Sliding mode approach to torque and pitch control for an wind energy system, Proc. IEEE Conference Indicon 2012, Kochi, Kerala, Dec 12, 2012.

2. B.Subudhi and P.S.Ogeti, Field oriented control in grid connected variable speed SCIG WECS, Proc. in National Conference in Burla, Dec 30, 2012.

3. B.Subudhi, P.S.Ogeti and A.K.Panda, Design of Error Amplifier in PWM controller for improving Dynamic Performance of Boost Converter, Proc. in Recent Advances in Power energy and Control, RAPEC 2013, Rourkela, Nov 23-24, 2013.

4. B.Subudhi and P.S.Ogeti, Sliding Mode Approach to Regulate Output Power of a DFIG Wind Energy Conversion System with Pitch Angle Control", Proc. 2nd international conference on Power System Analysis Control and Optimization(ICPSACO-2015), 10-12, December 2015.

References

[1] S. Sawyer, *Global Wind Energy Outlook 2014*.

[2] N. Z. Bin Wu, Yongquiang Lang and S. Kouro, *Power Conversion and Control of Wind Energy Systems*. USA: John Wiley and Sons,Inc., publication, IEEE Press, 2011.

[3] H.-J. G. O. I. Syed Muhammad Raza Kazmi, Hiroki Goto, "A novel algorithm for fast and efficient speed-sensorless maximum power point tracking in wind energy conversion system," *IEEE Trans. on Industrial Electronics*, vol. 58, no. 1, pp. 29–36, 2011.

[4] Y. Mitsutoshi and O. Motoyoshi, "Active and reactive power control for double fed wound rotor induction generator," *IEEE Trans. on Power Electronics*, vol. 6, no. 4, pp. 624–629, 1991.

[5] D. W. Xingyi xu, "Implementation of direct stator flux orientation control on a versatile DSP based system," *IEEE Trans. on Industry Applications*, vol. 27, no. 4, pp. 694–700, 1991.

[6] A. G. O.Barambones and F. Maseda, "Integral sliding controller for induction motor based on field-oriented control theory," *IET Control Theory Appl.*, vol. 1, no. 3, pp. 786–794, 2007.

[7] Y. R. V. Amir Ostadi, Amirnaser, "Modelling and stability analysis of a DFIG based wind-power generator interfaced with a series compensated line," *IEEE Trans. on Power Deliver*, vol. 24, no. 3, pp. 1504–1514, 2009.

[8] S. A. Roberto Cardenas, Ruben Pena and G. Asher, "Overview of Control Systems for the operation of DFIGs in wind-energy applications," *IEEE Trans. on Industrial Electronics*, vol. 60, no. 7, pp. 2776–2798, 2013.

[9] T. Kyohei Kurohane, "A hybrid smart AC/DC power system," *IEEE Trans. on Smart grid*, vol. 1, no. 2, pp. 199–204, 2010.

[10] H. G. G. Yang, "Robust pitch controller for output power levelling of variable-speed variable-pitch wind turbine generator systems," *IET Renewable Power Generation*, vol. 3, no. 2, p. 168179, 2009.

[11] M. Kayikc and J. V. Milanovi, "Reactive power control strategies for DFIG-based plants," *IEEE Trans. on Energy Conversion*, vol. 22, no. 2, pp. 389–396, 2007.

[12] P. M. O.S.Ebrahim, M.F.Salem, "Application of linear quadratic regulator theory to the stator field oriented control of induction motors," *IET Electric Power applications*, vol. 4, no. 8, pp. 637–646, 2010.

[13] A. U. Endusa Billy Muhando, Tomonobu Senjyu and T. Funabashi, "Gain-scheduled H_∞ control for WECS via LMI techniques and parametrically dependent feedback part ii: Controller design and implementation," *IEEE Trans. on Industrial Electronics*, vol. 58, no. 1, pp. 57–65, 2011.

[14] A. Pena, Clare, "Doubly fed induction generator using back-to-back PWM converters and its application to variable-speed wind-energy generation," *IEE Proc. Electr. Power Appl.*, vol. 143, no. 3, pp. 231–241, 1996.

[15] M. Kayikci, "Reactive power control strategies for DFIG-based plants," *IEEE Trans. on Energy Conversion*, vol. 22, no. 2, pp. 389–396, 2007.

[16] H. C. L. Chen, Lu, "An analytical approach to maximum power tracking and loss minimization of a doubly fed induction generator considering core loss," *IEEE Trans. on Energy Conversion*, vol. 24, no. 1, pp. 137–145, 2012.

[17] X. Tang, "A flexible active and reactive power control strategy for a variable speed constant frequency generating system," *IEEE Trans. on Power Electron.*, vol. 10, no. 4, pp. 472–478, 1995.

[18] W. C. L. Xu, "Torque and reactive power control of a doubly fed induction machine by position sensorless scheme," *IEEE Trans. on Industrial Application*, vol. 31, no. 3, pp. 636–642, 1995.

[19] M. Depenbrock, "Direct self-control (DSC) of inverter-fed induction machine," *IEEE Trans. on Power Electron.*, vol. 3, no. 4, pp. 420–429, 1988.

[20] G. L. R. Y. Yazhou Lei, Alan Mullane, "Modelling of a wind turbine with a Doubly fed induction generator for grid integration studies," *IEEE Trans. on Energy Conversion*, vol. 21, no. 1, pp. 257–264, 2006.

[21] N. M. Ted K.A.Brekken, "Control of a doubly fed induction generator under unbalanced grid voltage conditions," *IEEE Trans. on Energy Conversion*, vol. 22, no. 1, pp. 1–10, 2007.

[22] M. S.Chondrogiannis, "Stability of double fed induction generator under stator voltage oriented vector control," *IET Renewable Power Generation*, vol. 2, no. 3, pp. 170–180, 2008.

[23] R. D. D. S. Muller, M. Deicke, "Doubly fed induction generator systems for wind turbines," *IEEE Trans. on Industrial Application*, vol. 8, no. 3, pp. 26–33, 2002.

[24] S. R. S. Heath Hofmann and C. R. Sullivan, "Stator flux- based vector control of induction machines in magnetic saturation," *IEEE Trans. on Industry Applications*, vol. 33, no. 4, pp. 935–942, 1997.

[25] R. Datta and V.T.Ranganathan, "Variable speed wind power generation using doubly fed rotor induction machine-A comparison with alternative schemes," *IEEE Trans on Energy Conversion*, vol. 17, no. 3, pp. 414–421, 2002.

[26] P.-E. V. Francois Bonnet and M. Pietrzak-David, "Direct torque control of doubly fed induction machine," *IEEE Trans. on Industrial Electronics*, vol. 54, no. 5, pp. 2482–2490, 2007.

[27] m. j.-b. Jihen arbi, "Direct virtual torque control for doubly fed induction generator grid connection," *IEEE Trans. on Industrial Electronics*, vol. 56, no. 10, pp. 4163–4173, 2010.

[28] r. k. Lingling fan, "Harmonic analysis of a DFIG for a wind energy conversion system," *IEEE Trans. on Energy Conversion*, vol. 25, no. 1, pp. 181–190, 2010.

[29] J. P. J. M. C. G. Abad, M. A. Rodriguez, "Direct torque control for doubly fed induction machine-based wind turbines under voltage dips and without crowbar protection," *IEEE Trans. on Energy Conversion*, vol. 25, no. 2, pp. 586–588, 2010.

[30] K. C. W. Si Zhe Chen, Norbert C Cheung and J. Wu, "Integral sliding-mode direct torque control of doubly-fed induction generators under unbalanced grid voltage," *IEEE Trans. on Energy Conversion*, vol. 25, no. 2, pp. 356–368, 2010.

[31] P. C. Abad, Rodrguez, "Direct torque control for doubly fed induction machine-based wind turbines under voltage dips and without crowbar protection," *IEEE Trans. on Energy Conversion*, vol. 25, no. 2, pp. 586–588, 2010.

[32] T. I.Takahashi, "A new quick-response and high efficiency control strategy of an induction motor," *IEEE Trans. on Industrial Application*, vol. 22, no. 5, pp. 820–827, 1986.

[33] V. R. R. Datta, "Direct power control of gridconnected wound rotor induction machine without rotor position sensors," *IEEE Trans. on Power Electron.*, vol. 16, no. 3, pp. 390–396, 2001.

[34] L. Xu and P. Cartwright, "Direct active and reactive power control of DFIG for wind energy generation," *IEEE Trans. on Energy Conversion*, vol. 21, no. 3, pp. 750–758, 2006.

[35] Y. H. Peng Zhou and D. Sun, "Improved direct power control of DFIG-based wind turbine during network unbalance," *IEEE Trans. on Power Electronics*, vol. 24, no. 11, pp. 2465–2474, 2009.

[36] B. H. Y. H. Jiabing Hu, Heng Nian and Z. Q. Zhu, "Direct active and reactive power regulation of DFIG using sliding-mode control approach," *IEEE Trans. on Energy Conversion*, vol. 25, no. 4, pp. 1028–1039, 2010.

[37] D. Chwa and K.-B. Lee, "Variable structure control of the active and reactive powers for a DFIG in wind turbines," *IEEE Trans. on Industry Applications*, vol. 46, no. 6, pp. 2545–2555, 2010.

[38] M. K. Bourdoulis and A. T. Alexandridis, "Direct power control of DFIG wind systems based on nonlinear modeling and analysis," *IEEE Journal of Emerging and selected topics in Power Electronics*, vol. 2, no. 4, pp. 764–775, 2014.

[39] H. Shang, "Sliding-mode-based direct power control of grid-connected wind-turbine-driven doubly fed induction generators under unbalanced grid voltage conditions," *IEEE Trans. on Energy Conversion*, vol. 27, no. 2, pp. 362–373, 2012.

[40] S. Zhou, He, "Improved direct power control of a DFIG-based wind turbine during network unbalance," *IEEE Trans. on Power Electron.*, vol. 24, no. 11, pp. 2465–2474, 2009.

[41] I. P. Abad, Rodrguez, "Direct power control of doubly-fed-induction-generator-based wind turbines under unbalanced grid voltage," *IEEE Trans. on Power Electron.*, vol. 25, no. 2, pp. 442–452, 2010.

[42] A. Santos-Martin, Rodriguez-Amenedo, "Direct power control applied to doubly fed induction generator under unbalanced grid voltage conditions," *IEEE Trans. on Power Electron.*, vol. 23, no. 5, pp. 2328–2336, 2008.

[43] L. H. T. P. A. Petersson, T. Thiringer, "Modeling and experimental verification of grid interaction of a DFIG wind turbine," *IEEE Trans. on Energy Conversion*, vol. 20, no. 4, pp. 878–886, 2005.

[44] P. C. L. Xu, "Direct active and reactive power control of DFIG for wind energy generation," *IEEE Trans. on Energy Conversion*, vol. 21, no. 3, pp. 750–758, 2006.

[45] L. X. D. Zhi, "Direct power control of DFIG with constant switching frequency and improved transient performance,," *IEEE Trans. on Energy Conversion*, vol. 22, no. 1, pp. 110–118, 2007.

[46] R. K. Lingling Fan, "Modelling of DFIG based wind farms for SSR analysis," *IEEE Trans. on Power delivery*, vol. 25, no. 4, pp. 2073–2082, 2010.

[47] J. P. W. Roberto Cardenas, RubenPena, "Control of the reactive power supplied by a matrix converter," *IEEE Trans. on Energy Conversion*, vol. 24, no. 1, pp. 301–303, 2009.

[48] M. M. Roohollah Fadaeinedjad and G. Moschopoulos, "Simulation of a wind turbine with doubly fed induction generator by FAST and Simulink," *IEEE Trans. on Energy Conversion*, vol. 23, no. 2, pp. 690–700, 2008.

[49] J. M. A. B. Miguel Castilla, Jaume Miret and L. G. de Vicuna, "Direct rotor current-mode control improves the transient response of doubly fed induction generator-based wind turbines," *IEEE Trans. on Energy Conversion*, vol. 25, no. 3, pp. 722–731, 2010.

[50] C. X. Liu, Blaabjerg, "Stator current harmonic control with resonant controller for doubly fed induction generator," *IEEE Trans. on Power Electron.*

[51] W. S. Li, Haskew, "Control of DFIG wind turbine with direct-current vector control configuration," *IEEE Trans. on Sustain. Energy*, vol. 3, no. 1, pp. 1–11, 2012.

[52] T. Karaipoom and I. Ngamroo, "Optimal superconducting coil integrated into DFIG wind turbine for fault ride through capability enhancement and output power fluctuation suppression," *IEEE Trans. on Sustainable Energy*, vol. 6, no. 1, pp. 28–42, 2015.

[53] H. K. Endusa Billy Muhando, Tomonobu Senjyu and T. Funabashi, "Extending the modelling framework for wind generation systems: RLS-based paradigm for performance under high turbulence inflow," *IEEE Trans. on Energy Conversion*, vol. 24, no. 1, pp. 211–221, 2009.

[54] N. U. T. F. H. F. Tomonobu Senjyu, Ryosei Sakamoto and H. Sekine, "Output power leveling of wind turbine generator for all operating regions by pitch angle control," *IEEE Trans. on Energy Conversion*, vol. 21, no. 2, pp. 467–475, 2006.

[55] D. W. M. Soliman, O.P. Malik, "Multiple model multiple-input multiple-output predictive control for variable speed variable pitch wind energy conversion systems," *IET Renew. Power Gener.*, vol. 5, no. 2, p. 124136, 2011.

[56] O. P. M. Mostafa Soliman, Member and D. T. Westwick, "Multiple model predictive control for wind turbines with doubly fed induction generators," *IEEE Trans on Sustainable Energy*, vol. 2, no. 3, pp. 215–225, 2011.

[57] T. D. Z. J. Can Huang, Fangxing Li and X. Ma, "Second-order cone programming-based optimal control strategy for wind energy conversion systems over complete operating regions," *IEEE Trans. on Sustainable Energy*, vol. 6, no. 1, pp. 263–271, 2015.

[58] F. Filho, De Oliverira Filho, "A predictive power control for wind energy," *IEEE Trans. on Sustain. Energy*, vol. 2, no. 1, pp. 99–105, 2011.

[59] F. Filho, "Model-based predictive control applied to the doubly-fed induction generator direct power control," *IEEE Trans. Sustain. Energy*, vol. 3, no. 3, pp. 398–406, 2012.

[60] G.-E. S. Mauricio, Leon, "An adaptive nonlinear controller for DFIM-based wind energy conversion system," *IEEE Trans. on Energy Conversion*, vol. 23, no. 4, pp. 1025–1035, 2008.

[61] H. Liu, "Design of a self-tuning PI controller for a STATCOM using particle swarm optimization," *IEEE Trans. on Industrial Electronics*, vol. 57, no. 2, pp. 702–715, 2010.

[62] H. D. B. Fernando A. Inthamoussou, Fernando D. Bianchi and R. J. Mantz, "LPV wind turbine control with anti-windup features covering the complete wind speed range," *IEEE Trans. on Energy Conversion*, vol. 29, no. 1, pp. 259–266, 2014.

[63] A. U. Endusa Billy Muhando, Tomonobu Senjyu and T. Funabashi, "Gain-scheduled H_∞ control for WECS via LMI techniques and parametrically dependent feedback part i: Model development fundamentals," *IEEE Trans. on Industrial Electronics*, vol. 58, no. 1, pp. 48–56, 2011.

[64] J. Y. Z. F. Lescher and P. Borne, "Robust gain scheduling controller for pitch regulated variable speed wind turbine," *Stud. Inform. Control*, vol. 14, no. 12, pp. 299–315, 2005.

[65] R. M. F. Bianchi and C. Christiansen, "Gain scheduling control of variable speed wind energy conversion systems using quasi-PV models," *Control Engg. Practice*, vol. 13, no. 2, pp. 247–255, 2005.

[66] D. Leith and W. Leithead, "Appropriate realisation of gain-scheduled controllers with application to wind turbine regulation," *Int. J. Control*, vol. 65, no. 2, pp. 223–248, 2005.

[67] a. B. K. Stol, B. Rigney, "Accommodating control of a variable-speed turbine using a symbolic dynamics structural model," *Proc. 2000 ASME Wind Energy Symp.*

[68] J. W. X.Y. Zhang and J.-M. Yang, "H-infinity robust control of constant power output for the wind energy conversion system above rated wind," *Control Theory and Application*, vol. 25, no. 2, pp. 321–324, 2008.

[69] S. Heier, *Grid Integration of Wind Energy Conversion Systems.* ISBN 0-97143-X: John Wiley and Sons Ltd, 1998.

[70] T. A.-A. Brice Beltran and M. E. H. Benbouzid, "Sliding mode power control of variable-speed wind energy conversion systems," *IEEE Trans. on Energy Conversion*, vol. 23, no. 2, pp. 551–558, 2008.

[71] ——, "High-order sliding control of variable speed wind turbines," *IEEE Trans. on Industrial Electronics*, vol. 56, no. 9, pp. 3314–3321, 2009.

[72] G. T. L. X. Miren Itsaso Martinez, Ana Susperregui, "Sliding-mode control of a wind turbine-driven double-fed induction generator under non-ideal grid voltages," *IET Renewable Power Generation*, vol. 7, no. 4, pp. 370–379, 2013.

[73] B. Beltran and M. E. H. Benbouzid, "Second-order sliding mode control of a doubly fed induction generator driven wind turbine," *IEEE Trans. on Energy Conversion*, vol. 27, no. 2, pp. 261–269, 2012.

[74] S. S.A.Billings and M.J.Korenberg, "Identification of MIMO non linear systems using a forward-regression orthogonal estimator," *International Journal of Control*, vol. 49, no. 6, pp. 2157–2189, 1989.

[75] S. S.Chen and W.Luo, "Orthogonal least squares methods and their applications to non linear system identification," *International Journal of Control*, vol. 50, no. 5, pp. 1873–1896, 1989.

[76] S.A.Billings and S.Chen, "Extended model set, global data and threshold model identification of severely non linear systems," *International Journal of Control*, vol. 50, no. 5, pp. 1897–1923, 1989.

[77] S. K. Pradhan and B. Subudhi, "Non-linear adaptive model predictive controller for a flexible manipulator: An experimental study," *IEEE Transactions on control systems Technology*, vol. 22, no. 5, pp. 1754–1768, 2014.

[78] G.C.Goodwin and K.S.Sin, *Adaptive Filtering Prediction and Control*. New Jersey: Prentice-Hall, 1984.

[79] R. B. M.U.D. Mufti and S. C. Tripathy, "Self tuning control of winddiesel power systems," *IEEE Int. Conf. Power Electron.Drives Energy Syst. Ind. Growth*, vol. 1, pp. 258–264, 1996.

[80] B. P. Francoise Mei, "Modal analysis of grid connected doubly fed induction generators," *IEEE Tran. on Energy conversion*, vol. 22, no. 3, pp. 728–736, 2007.

[81] D. G. Jiefeng Hu, Jianguo Zhu, "Model predictive direct power control of doubly-fed induction generators under unbalanced grid voltage conditions in wind energy applications," *IET Renewable Power Generation*, vol. 8, no. 6, pp. 687 – 695, 2014.

[82] Y.-Y. H. Yung-Tsai Weng, "Sliding mode regulator for maximum power tracking and copper loss minimisation of a doubly fed induction generator," *IET Renewable Power Generation*, vol. 9, no. 4, pp. 297–305, 2015.

[83] B. H. Y. H. Jiabing Hu, Heng Nian and Z. Q. Zhu, "Direct active and reactive power regulation of DFIG using sliding-mode control approach," *IEEE Trans. on Energy Conversion*, vol. 25, no. 4, pp. 1028–1039, 2010.

[84] J. E. L. Holdsworth, X.G. Wu and N. Jenkins, "Comparison of fixed speed and doubly-fed induction wind turbines during power system disturbances," *IEE Proc-Gener. Transm. Distrib.*, vol. 150, no. 3, pp. 343–352, 2003.

[85] T. T. Akihiko Matsushita, "Decoupled preview control system and its application to induction motor drive," *IEEE Trans. on Industrial Electronics*, vol. 42, no. 1, pp. 50–57, 1995.

[86] Y. P. K. L. S. Jou, S. Lee, "Direct power control of a DFIG in wind turbines to improve dynamic responses," *Journal on Power Electron.*, vol. 9, no. 5, pp. 781–790, 2009.

[87] P. Z. Y. H. H. Nian, Y. Song, "Improved direct power control of a wind turbine driven doubly fed induction generator during transient grid voltage unbalance," *IEEE Trans. on Energy Conversion*, vol. 26, no. 3, pp. 976–985, 2011.

[88] E. Shehata, "Direct power control of wind-turbine-driven DFIG during transient grid voltage unbalance," *http://dx.doi.org/10.1002/we.1619*, vol. 55, no. 2, pp. 152–162, 2013.

[89] H. K. M.V. Kazemi, A.S. Yazdankhah, "Direct power control of DFIG based on discrete space vector modulation, renewable energy," *Elsevier, Renewable Energy*, vol. 35, no. 5, pp. 1033–1042, 2010.

[90] G. M. S. E.G. Shehata, "Direct power control of DFIG based wind energy generation systems under distorted grid voltage conditions," *International Journal of Electrical Power and Energy Systems*, vol. 53, pp. 956–966, 2013.

[91] L. Y. L. Xu, D. Zhi, "Direct power control of grid connected voltage source converters," *IEE power engineering annual meeting*, pp. 1–6, 2007.

[92] B. W. D. Zhi, L. Xu, "Improved direct power control of grid-connected dc/ac converters," *IEEE Trans. on Power Electron.*, vol. 25, no. 5, pp. 1280–1292, 2009.

[93] V. Utkin, "Sliding mode control design principles and applications to electric drives," *IEEE Trans. on Industrial Electronics*, vol. 40, no. 1, pp. 23–36, 1993.

[94] K. W. J. W. S.Z. Chen, N.C. Cheung, "Integral variable structure direct torque control of doubly fed induction generator," *IET Renew. Power Generation*, vol. 5, no. 1, pp. 18–25, 2011.

[95] R. W. D. Kairous, "DFIG-based fuzzy sliding-mode control of WECS with a flywheel energy storage," *Electric Power Systems Research*, vol. 93, no. 21, pp. 16–23, 2012.

[96] S. K. V.N. Pande, U.M. Mate, "Discrete sliding mode control strategy for direct real and reactive power regulation of wind driven DFIG," *Electric Power Systems Research,Elsevier*, vol. 100, no. 34, pp. 73–81, 2013.

[97] X. Y. J. Hu, "VSC-based direct torque and reactive power control of doubly fed induction generator," *Renewable Energy,Elsevier*, vol. 40, no. 1, pp. 13–23, 2012.

[98] S. C. Martinez, Tapia, "Sliding-mode control for DFIG rotor and grid side converters under unbalanced grid," *IEEE Trans. on Energy Conversion*, vol. 27, no. 2, pp. 328–339, 2012.

[99] J. H. L. Shang, "Sliding mode based direct power control of grid connected wind turbine driven doubly fed induction generator under unbalanced grid voltage conditions,," *IEEE Trans. on Energy Conversion*, vol. 27, no. 2, pp. 362–373, 2012.

[100] E. Sheahta, "Speed sensorless torque control of an IPMSM drive with online stator resistance estimation using reduced order EKF," *International Journal of Electrical Power and Energy Systems*, vol. 47, pp. 378–386, 2013.

[101] A. I. Iulian Munteanu, Seddik Bacha, "Energy-reliability optimization of wind energy conversion system by sliding mode control," *IEEE Trans. on Energy Conversion*, vol. 23, no. 3, pp. 975–985, 2008.

[102] L. Shang and J. Hu, "Sliding-mode-based direct power control of grid-connected wind-turbine-driven doubly fed induction generator under unbalanced grid voltage conditions," *IEEE Trans. on Energy Conversion*, vol. 27, no. 2, pp. 362–373, 2012.